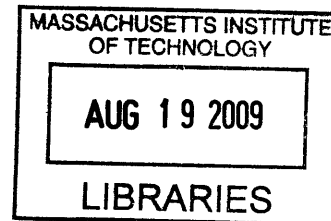


Design of a 2400MW Liquid-Salt Cooled Flexible Conversion Ratio Reactor

by
Robert C. Petroski

B.S. Nuclear Engineering/Engineering Physics
University of California, Berkeley, 2006



Submitted to the Department of Nuclear Science and Engineering
in Partial Fulfillment of the Requirements for the Degree of

Master of Science in Nuclear Science and Engineering
at the
Massachusetts Institute of Technology

September 2008

ARCHIVES

© 2008 Massachusetts Institute of Technology. All rights reserved.

Signature of Author _____
Department of Nuclear Science and Engineering

Handwritten signature of Robert C. Petroski in black ink.

Certified by _____

Professor Neil Todreas
Thesis Advisor

Certified by _____

Doctor Pavél Hejzlar
Thesis Advisor

Handwritten signature of Doctor Pavél Hejzlar in black ink.

Accepted by _____

Professor Jacquelyn C. Yanch
Chairman, Department Committee on Graduate Students

Handwritten signature of Professor Jacquelyn C. Yanch in black ink.

Design of a 2400MW Liquid-Salt Cooled Flexible Conversion Ratio Reactor

by
Robert C. Petroski

Submitted to the Department of Nuclear Science and Engineering
in Partial Fulfillment of the Requirements for the Degree of
Master of Science in Nuclear Science and Engineering

September 2008

ABSTRACT

A 2400MWth liquid-salt cooled flexible conversion ratio reactor was designed, utilizing the ternary chloride salt NaCl-KCl-MgCl_2 (30%-20%-50%) as coolant. The reference design uses a wire-wrapped, hex lattice core, and is able to achieve a core power density of 130 kW/l with a core pressure drop of 700kPa and a maximum cladding temperature under 650°C. Four kidney-shaped conventional tube-in-shell heat exchangers are used to connect the primary system to a 545°C supercritical CO_2 power conversion system. The core, intermediate heat exchangers, and reactor coolant pumps fit in a vessel approximately 10 meters in diameter and less than 20 meters high. Lithium expansion modules (LEMs) were used to reconcile conflicting thermal hydraulic and reactor physics requirements in the liquid salt core. Use of LEMs allowed the design of a very favorable reactivity response which greatly benefits transient mitigation. A reactor vessel auxiliary cooling system (RVACS) and four redundant passive secondary auxiliary cooling systems (PSACS) are used to provide passive heat removal, and are able to successfully mitigate both an unprotected station blackout transient as well as protected transients in which a scram occurs. Additionally, it was determined that the power conversion system can be used to mitigate both a loss of flow accident and an unprotected transient overpower.

Professor Neil Todreas, Thesis Co-supervisor
Dr. Pavel Hejzlar, Thesis Co-supervisor

Acknowledgments

I would first like to thank my thesis advisors Professor Neil Todreas and Dr. Pavel Hejzlar for the opportunity to work with them during my graduate studies. I am indebted to Professor Todreas for his excellent mentorship and Dr. Hejzlar for his technical insight. Thanks to Professor Driscoll for being a perpetual font of good ideas. Thanks very much to my coworkers on this project, Anna, C.J., Eugene, and Josh, as well as my officemates Anna, Paolo, and Edo for all being a pleasure to work with. I would also like to acknowledge the Department of Energy for their support and funding via the Advanced Fuel Cycle Initiative fellowship program. Thanks to my friends on both coasts and my family for their love and support.

Table of Contents

Abstract.....	3
Acknowledgments.....	5
Table of Contents.....	7
List of Figures.....	9
List of Tables.....	11
1. Introduction.....	13
1.1 Background.....	13
1.2 Objective and scope.....	14
1.3 Design process overview.....	17
1.4 Design constraints.....	18
2. Methodology.....	21
2.1 Description of the subchannel model.....	21
2.2 Orificing calculations.....	27
2.3 Description of RELAP model.....	31
2.4 Salt reactor reactivity feedback implementation.....	50
3. Salt Selection.....	57
3.1 Preliminary fluoride selection.....	57
3.2 Final chloride selection.....	63
3.3 Properties of the most promising salt candidate.....	65
4. Steady State Reactor Design.....	72
4.1 CR=1 reference core design.....	73
4.2 Heat exchanger design.....	78
4.3 LEM design.....	84
4.4 CR=0 design.....	89
5. Transient Performance.....	93
5.1 CR=1 unprotected station blackout.....	93
5.2 CR=1 unprotected loss of flow.....	116
5.3 CR=1 unprotected transient overpower.....	124
5.4 CR=0 transients.....	128
5.5 Protected Transients.....	136
6. Conclusions and Future Work.....	140
References.....	143

List of Figures

Figure 1.2-1 Schematic of a pool type reactor with a dual free level design.....	15
Figure 2.1-1 Examples of subchannels in a square array.....	21
Figure 2.1-2 Fenech and Gnielinski correlation comparison.....	24
Figure 2.2-1 CR=1 reference salt core BOL power peaking map	28
Figure 2.2-2 CR=1 orificing flow rate map	29
Figure 2.2-3 CR=1 Three-zone orificing flow rate map	29
Figure 2.2-4 CR=0 reference salt core BOL ower peaking map	30
Figure 2.2-5 CR=0 orificing flow rate map	31
Figure 2.2-6 CR=0 Three-zone orificing flow rate map	31
Figure 2.3-1 Nodalization diagram for the primary and secondary (PCS and PSACS) reactor coolant systems and RVACS.	36
Figure 2.3-2 RELAP and subchannel model pressure drop comparison	40
Figure 2.3-3 RELAP and subchannel temperature comparison.....	40
Figure 2.3-4 Vessel layout showing virtual free levels and time dependent volume	44
Figure 2.3-5 RVACS heat flux as a function of position.....	47
Figure 2.3-6 RVACS heat flux for explicit- and virtual-free-level models	48
Figure 2.4-1 Reactivity insertion due to coolant thermal expansion, CR=1 BOL.....	51
Figure 2.4-2 Reactivity insertion due to coolant thermal expansion, CR=0 BOL.....	52
Figure 2.4-3 Reactivity insertion due to fuel temperature increase, CR=1 BOL	53
Figure 2.4-4 Reactivity insertion due to fuel temperature increase, CR=0 BOL	54
Figure 2.4-5 Reactivity insertion due to lithium expansion modules	55
Figure 3.3-1 Power density vs. NaCl-KCl-MgCl ₂ property values.....	68
Figure 4.2-1 To-scale illustration of vessel layout.....	82
Figure 4.2-2 To-scale illustration of IHX layout	83
Figure 4.3-1 Schematic view of a lithium expansion module	85
Figure 4.3-2. Example of LEM reactivity insertion curve (25 LEMs/assembly)	87
Figure 4.3-3 CR=1 LEM and CTC reactivity responses	89
Figure 5.1-1 Short-term CR=1 salt reactor response to an SBO	96
Figure 5.1-2 Core midplane heat transfer coefficient and film temperature rise.....	96
Figure 5.1-3 Heat removal through the RVACS after SBO	98
Figure 5.1-4 Effect of changing SBO decay heat removal	100
Figure 5.1-5 Peak cladding temperatures for a high flow rate core.....	102
Figure 5.1-6 Effect of pump flywheels and a reactor scram on SBO response	103
Figure 5.1-7 CR=1 reactivity following an SBO.....	106
Figure 5.1-8 CR=1 Fission power following an SBO	106
Figure 5.1-9 CR=1 long term peak cladding temperature response to an SBO.....	108
Figure 5.1-10 CR=1 long term reactivity response to an SBO	108
Figure 5.1-11 CR=1 long term power response to an SBO; 200% power PSACS, 1.0x tank size case.....	109
Figure 5.1-12 CR=1 long term peak cladding temperature response to an SBO.....	111
Figure 5.1-13 CR=1 long term peak cladding temperature response to an SBO.....	113
Figure 5.1-14 CR=1 long term peak cladding temperature response to an SBO.....	114

Figure 5.1-15 CR=1 long term reactivity response to an SBO	115
Figure 5.1-16 CR=1 long term power response to an SBO; 60% power PSACS, 0.75x tank size case.....	115
Figure 5.2-1 Normalized valve area as a function of valve stem position.....	118
Figure 5.2-2 CR=1 salt reactor temperature response to a LOFA	119
Figure 5.2-3 CR=1 salt reactor reactivity response to a LOFA	119
Figure 5.2-4 CR=1 salt reactor power response to a LOFA	120
Figure 5.2-5 CR=1 salt reactor temperature response to a LOFA (shutdown case).....	122
Figure 5.2-6 CR=1 salt reactor reactivity response to a LOFA	123
Figure 5.2-7 CR=1 salt reactor power response to a LOFA (shutdown case).....	123
Figure 5.3-1 CR=1 salt reactor peak cladding temperature response to a UTOP.....	126
Figure 5.3-2 CR=1 salt reactor reactivity response to a UTOP	127
Figure 5.3-3 CR=1 salt reactor power response to a UTOP	127
Figure 5.4-1 Short-term CR=0 temperature response to an SBO	129
Figure 5.4-2 Short-term CR=0 reactivity response to an SBO	129
Figure 5.4-3 Long-term CR=0 temperature response to an SBO	130
Figure 5.4-4 Long-term CR=0 reactivity response to an SBO	130
Figure 5.4-5 Long-term CR=0 power response to an SBO	131
Figure 5.4-6 CR=0 temperature response to a LOFA.....	132
Figure 5.4-7 CR=0 reactivity response to a LOFA.....	132
Figure 5.4-8 CR=0 power response to a LOFA.....	133
Figure 5.4-9 CR=0 temperature response to a UTOP.....	134
Figure 5.4-10 CR=0 reactivity response to a UTOP.....	135
Figure 5.4-11 CR=0 power response to a UTOP.....	135
Figure 5.5-1 CR=1 response to a protected transient.....	139
Figure 5.5-2 CR=0 response to a protected transient.....	139

List of Tables

Table 1.4-1 Summary of design constraints for the salt-cooled reactor	20
Tables 2.3-1 NaCl-KCl-MgCl ₂ (30%-20%-50%) properties for RELAP	33
Table 2.3-1 Orificing and flow split in the core.....	38
Table 2.3-2 Internal power multipliers.	38
Table 2.3-3 Fuel conductivities (W/mK)	39
Table 2.3-4 Comparison of spreadsheet and RELAP model results for the salt reactor intermediate heat exchangers	42
Table 2.4-1 Salt reactor coolant density reactivity model for RELAP5-3D.....	52
Table 2.42 Salt reactor fuel temperature reactivity model for RELAP5-3D	54
Table 2.4-3 Salt reactor LEM reactivity model for RELAP5-3D.....	56
Table 3.1-1 Physical properties of candidate coolant salts ⁵	58
Table 3.2-2 Assumed NaF-KF-ZrF ₄ physical properties	61
Table 3.2-2 Reference fluoride core geometry	62
Table 3.2-3 CR=1 NaF-KF-ZrF ₄ salt core characteristics.....	62
Table 3.2-1 T-H analysis results of selected coolant salts	64
Table 3.3-1 Assumed NaCl-KCl-MgCl ₂ (30-20-50) physical properties.	65
Table 3.3-2 Neutron activation data.....	71
Table 4.1-1 Reference CR=1 salt core geometry.....	74
Table 4.1-2 CR=1 NaCl-KCl-MgCl ₂ salt reference core operating characteristics.	75
Table 4.2-1 Salt reactor IHX geometry and performance (for 1 out of 4 IHXs)	83
Table 4.4-1 CR=0 NaCl-KCl-MgCl ₂ salt reference core operating characteristics.	90
Table 5.3-1 CR=1 maximum control rod worth	126
Table 5.4-1 CR=0 maximum control rod worth	134

1. Introduction

This project is part of a larger Nuclear Energy Research Initiative (NERI) project at MIT investigating the use of different coolants in flexible conversion ratio (FCR) fast reactors. An FCR reactor can have different cores installed to operate at conversion ratios near zero to transmute minor actinides and near unity to improve uranium utilization. FCR reactors may become important for dynamically addressing changing fuel cycle requirements. Reducing inventories of long-lived minor actinides using low conversion ratio cores can reduce the number of repositories needed in the near term, while operating at a conversion ratio near unity would allow uranium resources to be extended for centuries in the long term. Having both capabilities present in a single reactor system would allow tremendous flexibility in managing minor actinide inventories; a reactor fleet using FCR reactors could be tailored to satisfy both disposal and fuel availability requirements as needed.

FCR work so far has focused on sodium cooled reactors. The objective of the MIT NERI project is to investigate the use of several other coolants for use in FCR reactor systems: lead, liquid salt, and CO₂. The role of this thesis is the design of a liquid-salt cooled FCR reactor, with a focus on salt selection and system thermal hydraulics.

1.1 Background

Prior to this project, there has been very little work on liquid salt fast reactors, only preliminary scoping studies. The term “liquid salt” as used here refers to coolant salt not containing fuel, as opposed to prior “molten salt” reactors that had fuel dissolved in the salt. Liquid salts are an

interesting coolant option because they are chemically compatible with air and water, are less corrosive to structural materials than lead, have extremely high boiling points, and are optically transparent. Also, they have high specific heats, comparable to that of water, which allows a lower coolant flow rate while reducing the temperature rise across the core.

While there has been little work on salt-cooled fast reactors, there is a significant body of experience with salt thermal reactors, most notably with the Molten Salt Reactor Experiment at ORNL, which used salt as fuel rather than coolant [Haubenreich, 1970; Robertson, 1965]. Also, there have been a number of past studies into the properties of different salt compositions which play an important role in the selection of a coolant salt [summarized in Williams 2006]. Also applicable to this thesis is concurrent work on the lead-cooled FCR reactor, since many of the design choices and specifications can be adapted from the lead design [Todreas & Hejzlar FCR reports].

1.2 Objective and scope

The overall goal of this thesis is to develop a commercial sized (2400 MWt) salt-cooled FCR reactor that is comparable to the lead, sodium, and gas cooled FCR reactor designs. In doing so, this thesis will identify the advantages and disadvantages of liquid salt as a coolant, as well as the challenges present in developing a liquid-salt cooled fast reactor. Although this thesis aims to design a FCR reactor these conclusions will be applicable to fast reactors in general as well.

The overall plant design selected is similar to that of existing lead and sodium cooled fast reactor designs, with a pool-type reactor using a dual free level primary coolant loop. A schematic

diagram of this reactor layout is shown in Figure 1.2-1. A dual free level design is used so that CO₂ from a failed heat exchanger tube cannot be entrained into the core, which would increase core reactivity and potentially lead to a criticality accident.

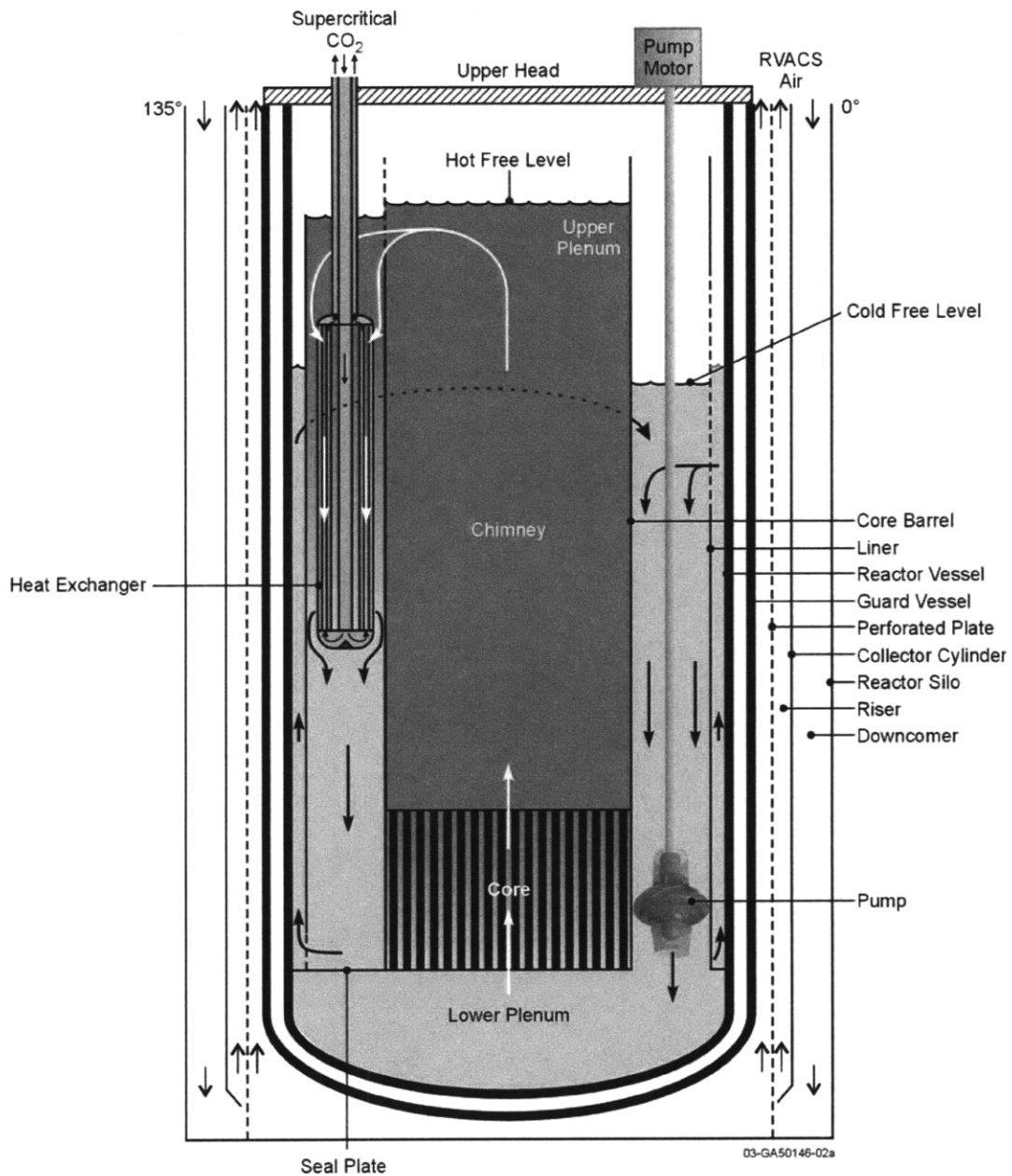


Figure 1.2-1 Schematic of a pool type reactor with a dual free level design [from Hejzlar et al., 2004]

Decay heat removal during shutdown occurs through a Reactor Vessel Auxiliary Cooling System (RVACS) and a Passive Secondary Auxiliary Cooling System (PSACS), a system designed for the lead-cooled FCR reactor. The PSACS consists of a heat exchanger connected to each power conversion system train via valves, which can discharge heat into large water tanks during transients. As with the lead design, a supercritical CO₂ cycle is used for power conversion. In the core, a tight-pitch hexagonal lattice using wire wrap spacers is used to achieve a low coolant volume fraction. A low coolant volume fraction is required because of the moderating ability and large positive coolant temperature coefficient of salt coolant. The materials used in the fuel, core, and vessel are the same as those in current sodium and lead reactor designs so the designs can be directly compared.

Within these general design choices, the goal of this thesis is to develop a liquid-salt cooled reactor that can match the lead FCR reactor in terms of power output (2400 MWth), power conversion system performance, and total vessel size, while still satisfying materials constraints. Additionally, the salt system must be able to demonstrate passive safety for three bounding unprotected transients: a station blackout, a loss of flow accident, and a transient overpower.

Because some of the design choices for the salt reactor have been adapted from previous liquid metal cooled reactor designs, this thesis builds on past work for these designs and focuses on areas in which the salt design differs from previous designs. This thesis focuses on salt selection as well as salt steady state and thermal hydraulics. While reactor physics data certainly is incorporated into the design, the majority of physics design work was done by Eugene Shwageraus, a post doctorate also working on this NERI project.

1.3 Design process overview

Design for the liquid salt reactor began with the development of a core design that could satisfy reactor physics and thermal hydraulics constraints while outputting the desired amount of power and maximize power density. A large number of design parameters were available including geometric parameters, coolant velocities, and choice of coolant salt. To rapidly evaluate a large number of different core designs, a subchannel spreadsheet model of the core was developed mirroring the code SUBCHAN, developed to analyze the lead-cooled FCR reactor [Todreas & Hejzlar, 2006a]. It was found early on that fluoride coolant salts were unable to meet a 100 kW/l power density target while simultaneously satisfying reactor physics requirements. Chloride salts were found to perform better both neutronicallly and thermal hydraulically for fast reactor applications and were adopted for subsequent designs. However, even using chloride salts and an extremely small P/D (1.086), additional measures were required to reduce the coolant temperature coefficient to an acceptable level, such as hydride control rods, streaming assemblies, and axial blankets, each of which reduced the power density of the core. In order to reconcile reactor physics and thermal hydraulic constraints, Lithium thermal Expansion Modules (LEMs) were introduced to passively reduce the coolant temperature coefficient. LEMs allowed the core P/D to be increased to 1.19, greatly improving core thermal hydraulics and allowing core power density to increase to 130 kW/l.

The subchannel spreadsheet model was used to evaluate both hot channel and core average performance for the final core design. Intermediate heat exchangers for the salt reactor were designed using another spreadsheet model developed by Anna Nikiforova for designing the lead-cooled FCR reactor [Todreas & Hejzlar, 2008 Appendix 3C]. The final core and IHX designs

were implemented in a RELAP5-3D model in order to perform transient analyses. Portions of the model corresponding to the power conversion system and the RVACS could be taken directly from the lead-cooled FCR design. Three transient sequences were analyzed: an unprotected station blackout (SBO), an unprotected loss of flow accident (LOFA), and an unprotected transient overpower (UTOP). Based on these analyses, the salt reactor's lithium expansion modules and passive safety systems were modified so that each of the three transient scenarios could be successfully and passively mitigated.

During the course of this design work, emphasis was given to first developing a successful unity conversion ratio design, because it was judged as likely to be more desirable for future fuel cycle needs. Because much of the design of liquid-salt cooled reactor is adapted from the lead-cooled reactor design, this report makes frequent mentions to the lead-cooled reactor as a base case for salt studies. The description of the lead-cooled FCR reactor is given in the Flexible Conversion Ratio Fast Reactor Systems Evaluation reports by Todreas and Hejzlar [2006-2008], and the corresponding thesis by Nikiforova [2008].

1.4 Design constraints

The salt-cooled FCR reactor uses the same structural materials as similar fast reactors: T-91 for the core cladding and intermediate heat exchanger tubes, and SS316 for the reactor and guard vessels. These materials were selected based on their suitability for high temperature operation, corrosion resistance, and near-term availability. For each material, there are temperature constraints for steady state operation and transients, as well as a neutron fluence constraint. Steady state temperature constraints for reactor structural materials are taken from the ASME

code for the materials employed. The salt reactor also uses the same metallic fuel as similar fast reactors, with the same temperature and burnup limits. In addition to materials constraints, there are reactor physics constraints relating to proliferation resistance and passive safety performance. These were found to be adequately met by reactor physics analyses and are not addressed in this report. Finally, there are a couple soft constraints which have a bearing on cost: the pressure drop across the core and the maximum vessel size. For pressure drop, a value of 1MPa is used because it is comparable to that of existing fast reactors [IAEA, 2006], while for vessel size the dimensions of the lead-cooled FCR reactor & S-PRISM vessels are used for guidance. These constraints can be exceeded through the use of larger pumps or a larger vessel, although doing so would increase the capital cost of the salt system. A summary of the constraints adopted for this thesis is given in Table 1.4-1. More details regarding the development of constraints for FCR reactor systems are available in the NERI project quarterly reports.

Table 1.4-1 Summary of design constraints for the salt-cooled reactor

Cladding limits	Steady state membrane temperature:	650°C ^{††}	
	Transient inner temperature:	725°C	
	Fluence (E > 0.1 MeV):	3.3-4.0 x 10 ²³ n/cm ²	
	Irradiation damage:	150-200 dpa	
Fuel limits	Maximum temperature (CR=0/CR=1)	1200/1000°C	
	Peak burnup [†] (CR=0/CR=1)	Heavy metal loading dependent/150 MWd/kg	
Vessel limits	Steady state maximum membrane temperature:	430°C (for guard vessel)	
	Transient maximum membrane temperature:	750°C	
	Fluence (above 1 MeV):	5E+19n/cm ²	
Neutronic constraints	Proliferation	Pu isotopic composition	Same or dirtier than LWR spent fuel
	Reactivity coefficients	A/B [‡]	≤ 1.62
		C ΔT _c /B [*]	≥ 1; ≤ 2.7
		Δρ _{TOP} /B [*]	≤ 1.62
Thermal hydraulics	Core pressure drop	1.0 MPa	
Vessel size ^{**}	Outer vessel diameter:	9.2 m-10m	
	Vessel height:	19.5 m	

*Reactivity coefficient ratios. These limits are preliminary and will have to be revisited depending on core temperatures

**S-PRISM (a non-pressurized vessel) dimensions taken as guidance

†Alloy-type fuel, taking into account cladding stress for given cladding dimensions and temperature limits, based on analyses in Hejzlar et al. [2004]

††For the CR=0 core, which has a content of Pu larger than 20wt%, a smaller limit than 650°C may be required, driven by fuel cladding chemical interaction (FCCI) issues since Pu may form an eutectic with iron resulting in cladding thinning. A large amount of Zr in the fertile free fuel will mitigate FCCI and the exact limit is currently uncertain. Also, a zirconium liner can be developed to prevent this eutectic formation. The 650°C limit is consistent with the achievable category of materials, which were selected for the analyses in the project and assume successful completion of ongoing R&D on materials development.

2. Methodology

2.1 Description of the subchannel model

A spreadsheet model mirroring the function of the SUBCHAN code [Todreas & Hejzlar, 2006b] was developed to quickly analyze different core geometries, operating conditions, and coolant salts. The SUBCHAN code was developed to design the lead-cooled FCR reactor; it analyses a core by dividing it into a number of non-communicating subchannels. Examples of the different types of subchannels in a square-lattice assembly are shown in Figure 2.1-1. Based on user-inputted core geometry, coolant inlet flow rate and temperature, and core power distribution, SUBCHAN calculates the core pressure drop, coolant outlet temperature, as well as maximum cladding and fuel temperatures.

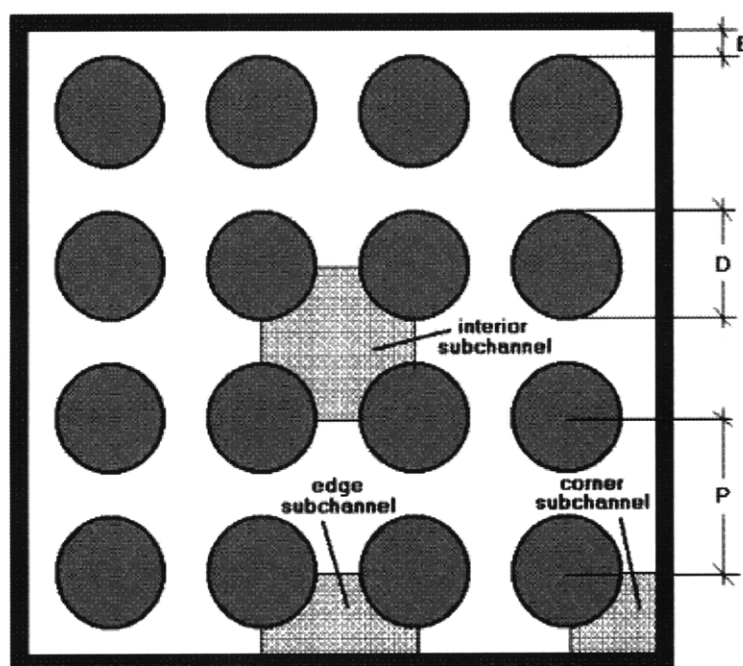


Figure 2.1-1 Examples of subchannels in a square array

The spread sheet model developed similarly divides the triangular-array, wire-wrapped salt assemblies into non-communicating subchannels. “Non-communicating” means the assumption is made that there is no heat or mass transfer between the different subchannels. This assumption is inaccurate for the salt core, because the presence of wire-wrap spacers leads to a great deal of mixing throughout each assembly. However, this assumption is conservative because mixing flattens the coolant temperature profile in each assembly, reducing the maximum fuel and cladding temperatures, so a subchannel analysis is useful for providing quick and meaningful results. Each subchannel is divided into a number of axial meshes (one each for the reflector and shield regions below the core, 11 for the active core, and one for the gas plenums above the core). The channel geometries are specified, allowing the subchannel flow area (A) to be calculated. The peaking factor and axial flux shape of the subchannel are also specified, so the heat input to each subchannel mesh (Q_i) can be computed. Given coolant inlet velocity (v_0) and enthalpy (h_0), conservation of energy (Equation 2.1-1) and mass (Equation 2.1-2) can be used to determine coolant velocity and enthalpy in subsequent axial nodes.

$$h_i = h_{i-1} + Q_i / \dot{m} \quad (2.1-1)$$

$$v_i \rho_i = v_0 \rho_0 = \dot{m} / A \quad (2.1-2)$$

The subscript i designates the axial node number, and ρ_i is the coolant density at node i , which along with coolant temperature, heat capacity, and thermal conductivity can be calculated from the coolant enthalpy h_i .

With the coolant properties and flow velocity, correlations can be used to determine the friction factor and heat transfer coefficient for each subchannel mesh. For friction factor the Cheng-Todreas [1986] correlation is used, which was developed to deal specifically with wire-wrap

flow bundles. Very little work has been done on heat transfer in wire wrap bundles, especially for high Prandtl number fluids such as liquid salts. This is because the coolant commonly used in wire-wrapped bundles is liquid sodium, which has a low Prandtl number and yields very low film temperature rises, making the convective heat transfer coefficient less important. One study was performed by Fenech [1985] on wire-wrap heat transfer in water-cooled bundles, but his results were for a fixed geometry ($P/D=1.05$) and could not be directly applied. Therefore, an alternate approach was needed to model heat transfer in the liquid-salt cooled core.

The approach taken was to use the well known Gnielinski heat transfer correlation [1976], which applies to $Re > 1000$ for tube flow, and apply it to wire wrap flow. The Gnielinski correlation has the following form:

$$Nu = \frac{\frac{\xi}{8} (Re-1000) Pr}{1 + 12.7 \sqrt{\frac{\xi}{8}} (Pr^{2/3} - 1)} \quad \xi = \frac{1}{(1.82 \log(Re) - 1.64)^2} \quad Re > 1000 \quad (2.1-3)$$

The Gnielinski correlation can be compared to the correlation developed by Fenech for a water cooled wire-wrap assembly (Eq. 2.1-4). This done by applying the Gnielinski correlation to the geometry tested by Fenech and setting the Prandtl number to 5.4, that of warm water. Results of the comparison are shown in Figure 2.1.-2.

$$Nu = \frac{h * D_H}{k} = \frac{1}{F_{hotspot}} * 0.0301 * Re^{0.79} * Pr^{0.43} \quad Re > 2300 \quad (2.1-4)$$

h : heat transfer coefficient (W/m^2K)

D_H : subchannel hydraulic diameter, including the wire (m)

k : coolant thermal conductivity (W/mK)

$F_{hotspot}$: hot spot factor (~ 1.2 for interior subchannels)

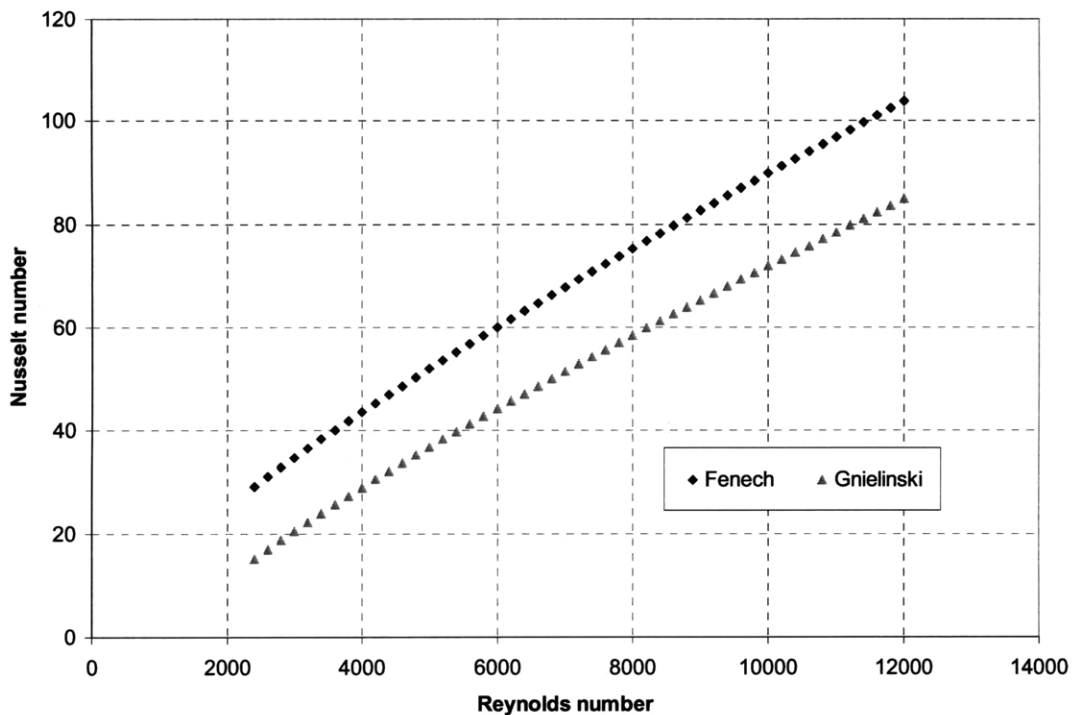


Figure 2.1-2 Fenech and Gnielinski correlation comparison

Figure 2.1.-2 shows that the Gnielinski correlation yields smaller values for Nusselt number, with values about half those of the Fenech correlation near transition flow Reynolds numbers. This is likely evidence that there are heat transfer enhancement mechanisms caused by the wire-wrap geometry, such as enhanced flow turbulence. Such mechanisms would not be simple to model and would require additional experimental data to verify. Since the Gnielinski correlation doesn't take these mechanisms into account, it should be considered a conservative estimate. Also, it should be noted that the difference between the modified Gnielinski and Fenech correlations becomes more pronounced for Prandtl numbers in the liquid salt range (~ 30), with the Gnielinski correlation becoming even more conservative. Therefore, the heat transfer analysis in this report as a whole is very conservative, due to the use of both the non-communicating subchannel approximation and the Gnielinski correlation.

Given the friction factor at each node in a subchannel, the pressure loss across the entire subchannel is given by:

$$\Delta P = \sum_i \left[\frac{1}{2} f_i \frac{L_i}{D_H} \rho_i v_i^2 + (\rho_i v_i^2 - \rho_{i-1} v_{i-1}^2) + \frac{1}{2} K_{L,i} \rho_i v_i^2 \right] \quad (2.1-5)$$

L_i : length of the i th mesh

D_H : the subchannel's wetted hydraulic diameter (includes the wire perimeter)

$K_{L,i}$: is any form loss (such as an orifice) associated with the i th mesh

The first term in the summation is the pressure loss due to friction, the second term is the pressure loss due to coolant acceleration (usually small), and the third term is the form loss. Here the pressure change due to gravity has been neglected since it has relatively little effect on pumping power (there is a small natural circulation head present when the reactor is operating because of different density coolant in the chimney and downcomer). A form loss coefficient of 0.4 is introduced to the entrance and exit of the core bundle to represent flow contraction and expansion at these points. These form losses were introduced to mirror the original SUBCHAN input decks. While the value of 0.4 at the exit is smaller than the correct value of 1.0, the contribution of these form losses to the total core pressure drop is minimal so the actual values can be safely neglected.

Cladding temperatures are calculated by dividing the linear heat rate (Q'_i) at a mesh by the thermal resistance (R_i) between the cladding and the coolant, and adding this temperature difference to the local coolant temperature:

$$T_{clad,i} = T_{coolant,i} + Q_i' / R_i \quad ; \quad R_i = \frac{1}{2\pi r_{co} h_i} + \frac{\ln(r_{co}/r_{ci})}{2\pi k_c} \quad (2.1-6)$$

r_{co} : cladding outer radius

r_{ci} : cladding inner radius

h_i : local heat transfer coefficient ($h_i = k_i \text{Nu}/D_H$, where k_i is the coolant thermal conductivity at node i)

k_c : cladding thermal conductivity

Here the temperature of the cladding's inner surface is used for comparison against the limit in Table 1.4-1 since it is higher. Fuel temperatures are calculated in a similar way by adding terms for the cladding inner oxide layer (roughly assumed to be 10 microns thick with a thermal conductivity of 2W/mK), the lead-alloy fuel-cladding bond, and the fuel pin to the thermal resistance. Note that SUBCHAN code uses node-averaged values for the linear heat rate, i.e. $(Q_i + Q_{i+1})/2$ instead of Q_i in Equation 2.1-6; this was changed for the spreadsheet model to better match the calculations performed by RELAP. The method employed here yields maximum cladding temperatures a few degrees higher than the SUBCHAN code.

Spreadsheet models were developed for interior, side, and corner subchannels of a hexagonal assembly. The models can be used to calculate the coolant flow rates in each subchannel that would produce a specified pressure loss. Coolant and cladding temperatures can also be computed, which showed that interior channels generally have the highest cladding temperature. Flow rate results for the subchannels can be summed to determine the total flow rate in an assembly for a given pressure drop, which in turn allows the total flow rate in the core to be computed. Flow through unheated channels (i.e. interassembly-space and shield/reflector

assemblies) is neglected because it is assumed that these flow rates can be made arbitrarily small through orificing.

Benchmarking

The spreadsheet subchannel model is a recreation of the SUBCHAN code in a different format, and tests using lead reactor parameters showed that the two models' results agreed exactly. This is expected because the spreadsheet performs the same set of calculations that SUBCHAN does using the same fundamental equations. The only changes made to allow for salt reactor modeling were the geometric parameters (square lattice to triangular), the correlations used, and the removal of node-averaged linear heat rates (see comments for Eq. 2.1-6). These changes were benchmarked by comparing the results to hand calculations (for the geometry changes) and the expected outputs for the correlations (from charts in the correlations' respective papers).

2.2 Orificing calculations

Without orificing, approximately the same coolant flow rate goes through each assembly.

Orificing can be used to reduce coolant flow through the core, which is desirable because this raises the average outlet temperature, increasing plant efficiency. A reduced flow rate also reduces the pumping power required to move coolant through the core.

With the spreadsheet subchannel model, it is possible to quickly determine the minimum flow rate in an assembly, given its radial peaking factor and axial flux shape, which does not cause the cladding temperature limit (650°C) to be exceeded. What results is an orificing map similar to that shown in Figure 2.2-2, corresponding to the assembly peaking factor map in Figure 2.2-1.

The numbers in the orificing map correspond to the relative flow rate in that assembly compared to the flow rate in the assembly with the maximum peaking factor (the hot assembly). Using the optimal orificing scheme shown in Figure 2.2-1, the flow rate in the core can be reduced about 23% from an unorificed core, a large improvement. However, the orificing scheme in Figure 2.2-2 uses a different orifice setting for nearly every assembly, and may be challenging to implement in practice. Another approach is to use the three-zone orificing scheme shown in Figure 2.2-3. This scheme minimizes the flow rate through the core using only three orifice settings, producing a flow reduction of about 15%, yielding the majority of the benefit of the optimal scheme. Use of a three-zone orificing scheme raises the core outlet temperature from 558°C to 569°C. The corresponding flow rate, 85% of the unorificed value, was subsequently assumed for calculating core performance parameters.

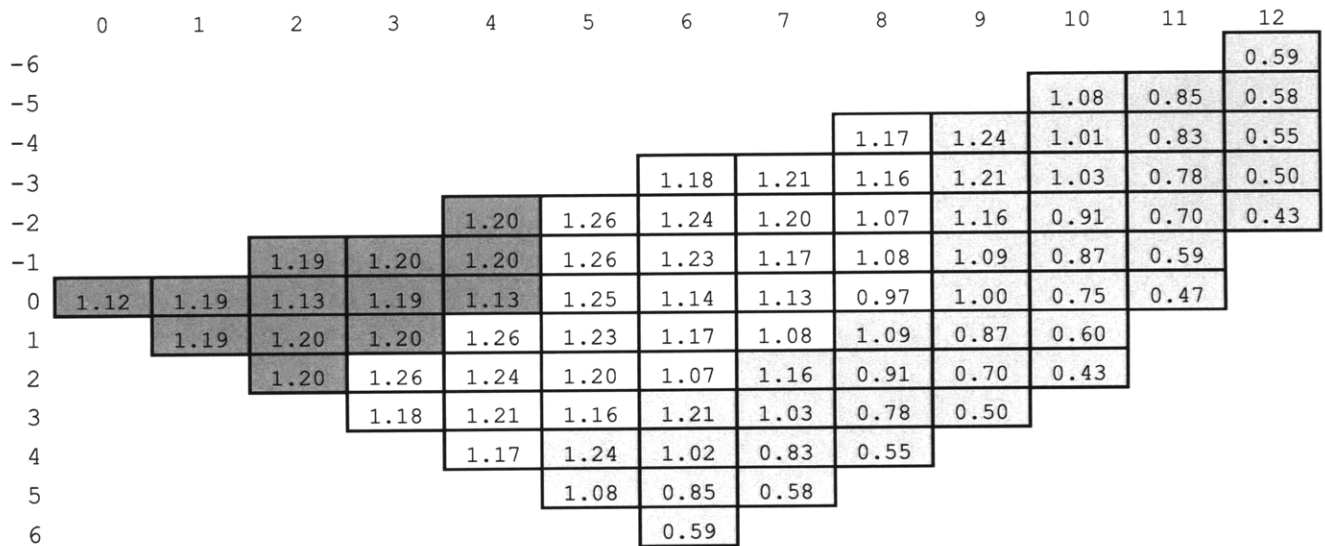


Figure 2.2-1 CR=1 reference salt core BOL power peaking map [Todreas & Hejzlar 2008a]

	0	1	2	3	4	5	6	7	8	9	10	11	12
-6													0.419
-5											0.828	0.628	0.411
-4									0.912	0.981	0.765	0.611	0.388
-3							0.922	0.951	0.903	0.951	0.783	0.570	0.351
-2					0.938	1.000	0.980	0.941	0.818	0.903	0.678	0.505	0.300
-1			0.929	0.938	0.938	1.000	0.970	0.912	0.827	0.837	0.645	0.419	
0	0.862	0.929	0.871	0.929	0.871	0.990	0.883	0.873	0.729	0.756	0.545	0.329	
1		0.929	0.938	0.938	1.000	0.970	0.912	0.827	0.837	0.645	0.427		
2			0.938	1.000	0.980	0.941	0.818	0.903	0.678	0.505	0.300		
3				0.922	0.951	0.903	0.951	0.783	0.570	0.351			
4					0.912	0.981	0.774	0.611	0.388				
5						0.828	0.628	0.411					
6							0.419						

Figure 2.2-2 CR=1 orificing flow rate map

	0	1	2	3	4	5	6	7	8	9	10	11	12
-6													0.427
-5											0.837	0.837	0.427
-4									1.000	1.000	0.837	0.837	0.427
-3							1.000	1.000	1.000	1.000	0.837	0.837	0.427
-2					1.000	1.000	1.000	1.000	0.837	1.000	0.837	0.837	0.427
-1			1.000	1.000	1.000	1.000	1.000	1.000	0.837	0.837	0.837	0.427	
0	1.000	1.000	1.000	1.000	1.000	1.000	1.000	1.000	0.837	0.837	0.837	0.427	
1		1.000	1.000	1.000	1.000	1.000	1.000	0.837	0.837	0.837	0.427		
2			1.000	1.000	1.000	1.000	0.837	1.000	0.837	0.837	0.427		
3				1.000	1.000	1.000	1.000	0.837	0.837	0.427			
4					1.000	1.000	0.837	0.837	0.427				
5						0.837	0.837	0.427					
6							0.427						

Figure 2.2-3 CR=1 Three-zone orificing flow rate map

The values in Figures 2.2-1 through 2.2-3 are just for the core beginning-of-life power map; the power map changes somewhat over the life of the core. Similar orificing calculations can be performed for middle-of-life and end-of-life power maps, yielding two more flow rate maps similar to Figure 2.2-2. Another flow rate map can be constructed using the maximum values for each assembly position from the BOL, MOL, and EOL maps, which would represent the ideal

fixed orifices for the life of the core. At the time orificing calculations were performed for the salt reference cores, MOL and EOL data were not available, so their contribution to the overall orificing picture was not included. However, when performing the same study for the lead FCR reactor, it was found that because the radial flux shape changes little over the life of the core, this effect amounts to less than a 3% increase in coolant flow rate. Given the already large uncertainties in heat transfer calculations for the salt reactor this small factor was neglected.

Subchannel and orificing calculations were also performed for the CR=0 salt core, which found that despite needing a higher coolant flow rate through the hot assembly (due to higher peaking), the CR=0 core is more amenable to orificing, allowing the total core flow rate to be lower than that of the CR=1 core. Since the FCR reactor is designed to operate with both cores interchangeably, the higher CR=1 core flow rate was assumed for the CR=0 core as well. Power peaking and flow maps for the CR=0 case are given in Figures 2.2-4 through 2.2-6.

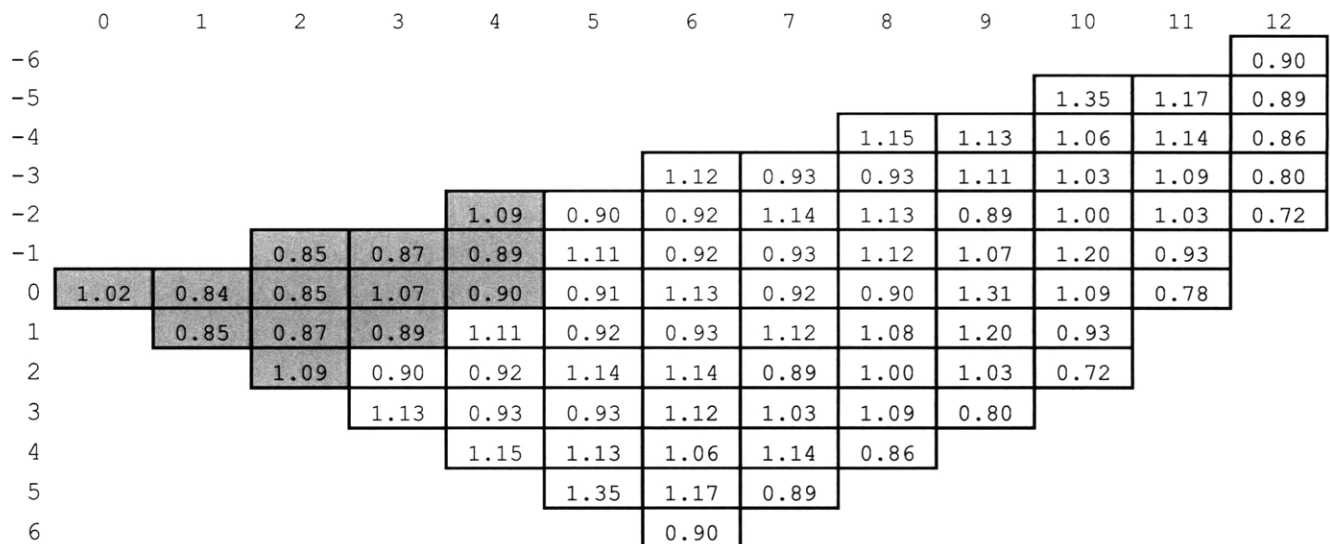


Figure 2.2-4 CR=0 reference salt core BOL power peaking map [Todreas & Hejzlar 2008a]

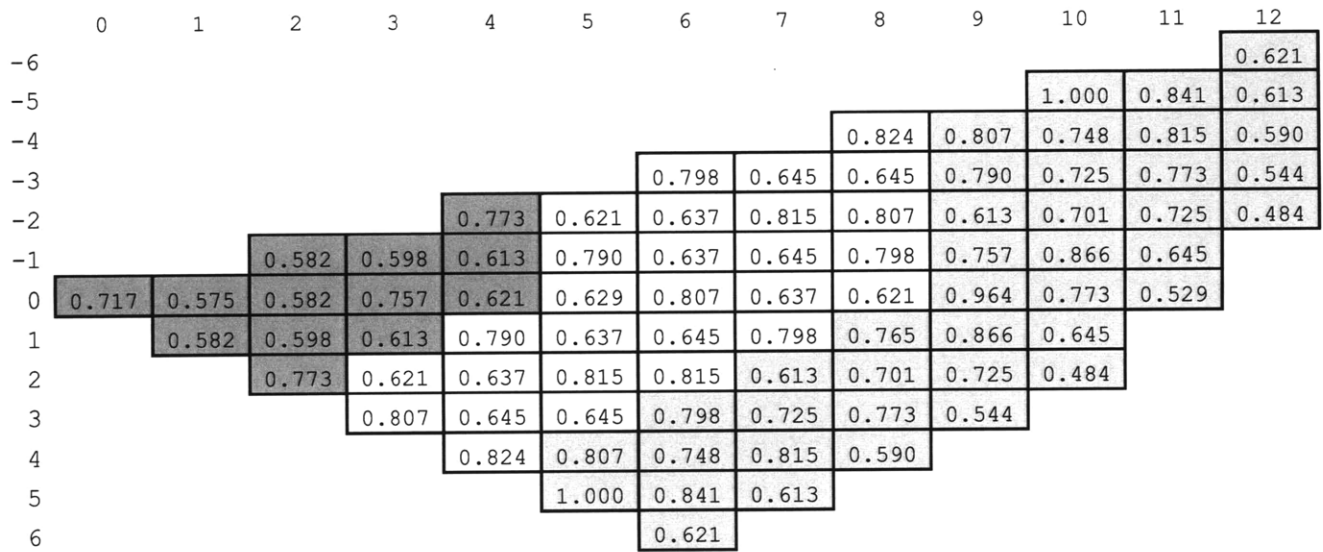


Figure 2.2-5 CR=0 orificing flow rate map

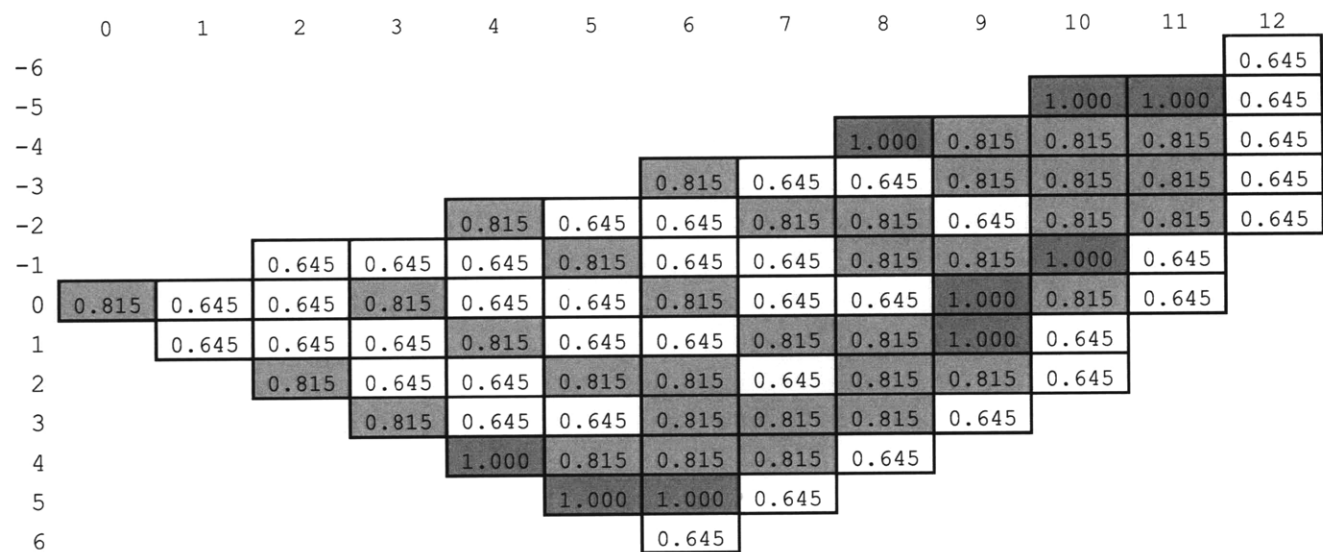


Figure 2.2-6 CR=0 Three-zone orificing flow rate map

2.3 Description of RELAP model

RELAP5-3D/ATHENA is a code developed at Idaho National Laboratory for the simulation of thermal hydraulic systems [RELAP, 2005], and is referred to interchangeably as “RELAP” in this thesis. A RELAP model was constructed of the salt reactor system, including the primary

coolant loop, power conversion system, ultimate heat sink, and auxiliary heat removal systems. This model is able to simulate the salt reactor's behavior for different steady state configurations and transient scenarios. The RELAP model for the salt reactor was constructed based on the RELAP model for the similarly configured lead-cooled FCR reactor, which itself was based on an earlier lead-bismuth reactor model developed at INL. RELAP model development for the salt reactor was performed in several stages:

1. Properties of the selected coolant salt were implemented in RELAP
2. A separate core model was created based on results from the spreadsheet subchannel analysis to yield the correct core average and limiting behavior.
3. A model of the intermediate heat exchangers was created based on results from a previously developed heat exchanger spreadsheet model.
4. Core and IHX component models were benchmarked and incorporated into a complete system model including the power conversion system and auxiliary heat removal systems.
5. The power conversion system's precooler sizes were adjusted slightly to yield the correct steady state system temperatures.
6. Lithium expansion module (LEM) and passive secondary auxiliary cooling system (PSACS) designs were finalized based on transient simulation results.

Salt implementation

The ternary chloride salt NaCl-KCl-MgCl₂ (30%-20%-50%) was selected based on neutronic and subchannel analyses as described in the salt selection section of this thesis. It was necessary

to first implement the properties of the selected coolant salt into the RELAP5-3D executable before any of the salt systems could be modeled. This was done by Cliff Davis at Idaho National Laboratory and Matthew Memmott at MIT, based on the set of salt properties submitted to them for this thesis. In addition to the basic thermal hydraulic properties described in the salt properties section (density, viscosity, thermal conductivity, and heat capacity), RELAP also requires values for salt isothermal compressibility, vapor pressure, vapor properties, surface tension, as well as triple point and critical point properties. Data for many of these properties do not exist, so values similar to properties of other liquid salts were used. Since the coolant in the liquid-salt cooled reactor never approaches the saturation line or sonic velocities, the values of these properties have no effect on the results obtained. The salt property values implemented into RELAP are given in Tables 2.3-1 numbers 1 through 9 below. The symbols for the properties are the same as those used in the report “Implementation of Molten Salt Properties into RELAP5-3D/ATHENA” (INEEL/EXT-05-02658).

Tables 2.3-1 NaCl-KCl-MgCl₂ (30%-20%-50%) properties for RELAP

Table 1. Constants for liquid salt

T_{melt} (K)	669.15
A_D (kg/m ³ -K)	-0.778
B_D (kg/m ³)	2260
A_κ (1/Pa)	1.62E-10
B_κ (1/K)	0.0018
c_p (J/kg-K)	1005.

Table 2. Parameters for vapor components

Component	M_i (g/mol)	\tilde{c}_{p_i} (J/mol-K)
NaCl	58.443	37.921
KCl	74.551	38.061
MgCl ₂	95.211	61.748

Table 3. Constants for salt vapor

M (g/mole)	80.049
R (J/kg-K)	103.862
c _p (J/kg-K)	662.9

Table 4. Saturation line constants

A _{sat}	8.806
B _{sat} (K)	10375

Table 5. Values for triple and critical points

T ₀ (K)	669.15
P ₀ (Pa)	2.668E-5
T _{crit} (K)	2615.1
P _{crit} (Pa)	9.196E6

Table 6. Reference values for specific internal energy and specific entropy.

u _{f0} (J/kg)	0.0
s _{f0} (J/kg-K)	0.0
u _{g0} (J/kg)	8.164E5
s _{g0} (J/kg-K)	3201
u _{crit} (J/kg)	1.9042E6
s _{crit} (J/kg-K)	1356

Table 7. Constants for transport properties of liquid.

A _μ (Pa-s)	5.18E-5
B _μ (K)	3040
K (W/m-K)	0.39

Table 8. Constants for surface tension.

A _σ (N/m-K)	-4.31E-5
B _σ (N/m)	0.1131

Table 9. Parameters used for calculating the dynamic viscosity of the vapor components.

Component	M _i (g/mol)	\tilde{c}_{p_i} (J/mole-K)	T _{melt} (K)	\tilde{V} (cm ³ /mole)	$\frac{\varepsilon}{K_i}$ (K)	σ _i (Å)
NaCl	58.443	37.921	1073.8	35.68	2062	4.02
KCl	74.551	38.061	1044.0	46.38	2004	4.39
MgCl ₂	95.211	61.748	987.0	53.84	1895	4.61

Overview of RELAP nodalization

The nodalization diagram created for the lead-cooled FCR reactor [Todreas & Hejzlar, 2008b] is shown in Figure 2.3-1. The salt reactor model nodalization is identical in nearly every respect, aside from some differences explained in the subsection about virtual free levels. The volumes

numbered in the 500s correspond to the liquid salt primary system, the 100s, 200s, 300s, and 400s make up the four CO₂ secondary trains, 600s to the ultimate heat sink water, 800s to the RVACS air, and 900s to the PSACS water tanks. Time-dependent volumes (effectively infinite mass sources/sinks) are set up to represent the boundary conditions for the open RVACS and ultimate cooling systems, as well as to represent a virtual “atmosphere” for the primary circuit.

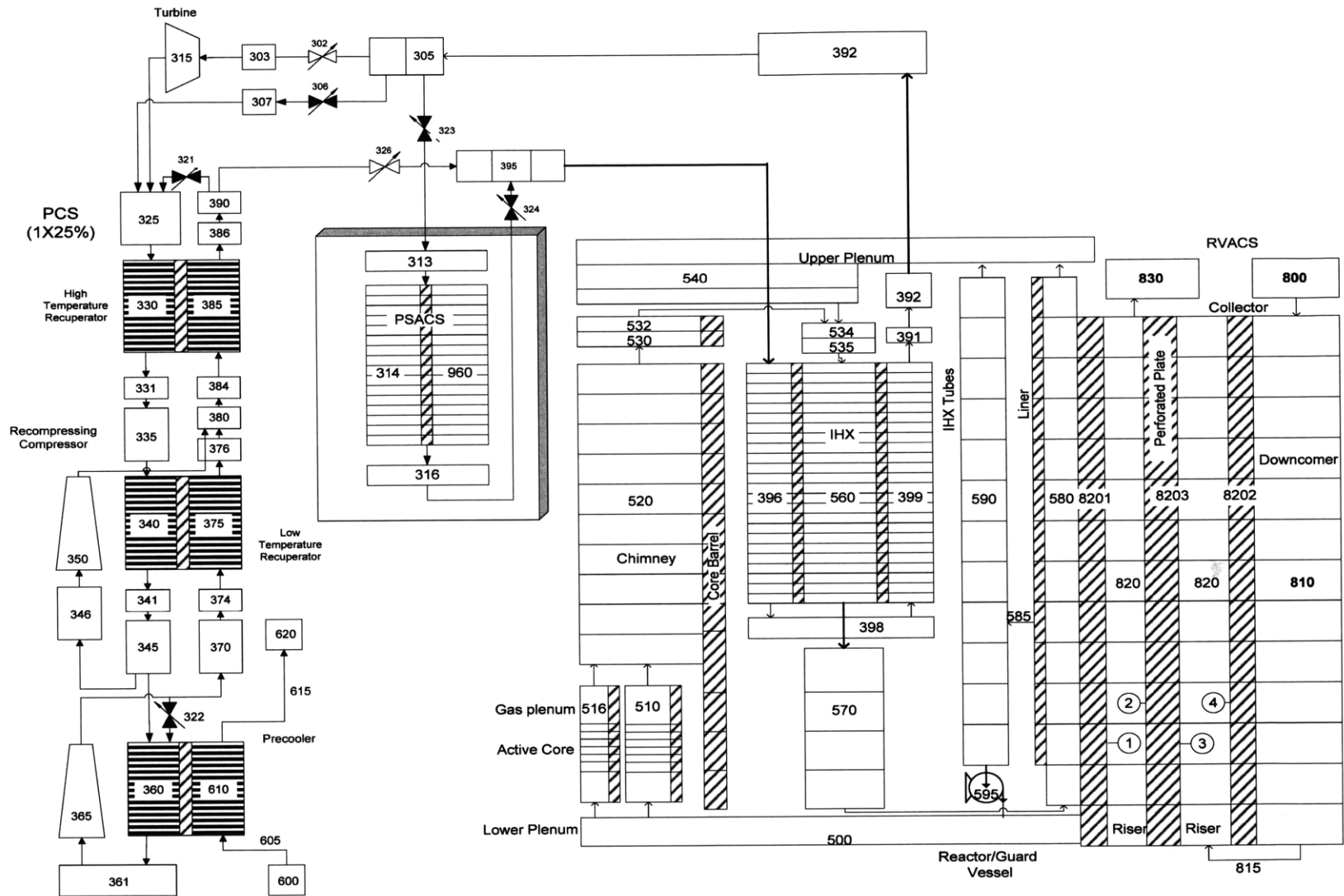


Figure 2.3-1 Nodalization diagram for the primary and secondary (PCS and PSACS) reactor coolant systems and RVACS.

Beginning at the lower plenum below the core, volume 500, coolant moves through volumes 510 and 516 which represent the core. Volume 516 is the hot channel and volume 510 is the average channel; together they model both the overall performance of the core as well as its performance in the most limiting assemblies. Each core volume is divided into 23 axial nodes, one each for the reflector and shield below the core, 11 for the active core, and 10 for the gas plenums above the core. Above the core is volume 520, the chimney, which in the salt reactor is bottlenecked to allow more room for the intermediate heat exchangers. Volumes 530 through 540 are at the top of the reactor vessel and distribute coolant from the chimney to the annulus above the four intermediate heat exchangers, volume 560 through 563. The set of downcomers below the heat exchangers is volume 570, which connects to volume 580, the peripheral riser. The riser is connected to volume 590, the second set of downcomers, then the reactor coolant pump, volume 595, pumps coolant back into the lower plenum.

The remaining systems (RVACS air and power conversion system) are taken from the lead-cooled FCR reactor model and were not appreciably modified during this project, other than to connect them appropriately to the liquid salt primary system. One exception is the design of the PSACS, which was changed in the course of transient analysis; these changes are described below in the PSACS modeling subsection and later in the transient analysis section.

RELAP core model

As described above, the salt core is divided into a hot channel and an average channel. Each channel is axially divided into 23 regions, one each for the blanket and reflector, 11 for the heated region of the core, and 10 for the gas plenum/LEM region above the core. Since the

interior subchannels of the hot assemblies have the highest cladding temperatures, the hot channel in the RELAP model is composed exclusively of interior subchannels, rather than of entire assemblies. This hot channel is equivalent to the heated interior subchannels of 12 assemblies, all using a hot subchannel peaking factor 2% greater than the highest assembly peaking factor, the same peaking factor used in the subchannel model.

A summary of the core RELAP implementation is given in Tables 2.3-1 and 2.3-2. The hot channel area is different for the two conversion ratios because the CR=1 core has more fuel rods and thus more heated channels per assembly. Because of higher peaking in the CR=0 core, the average channel is more strongly orificed, directing more flow through the hot channel. For the power multipliers, values are listed starting from the bottom of the core. Fuel conductivities for the salt reactor cores are given in Table 2.3-3.

Table 2.3-1 Orificing and flow split in the core

	CR=1	CR=0
Highest assembly peaking factor	1.26	1.35
Number of assemblies	12	12
Channel area (m ²) (hot/average)	0.09391/4.48985	0.09224/4.49152
Orificing coefficients (hot/average)	0.0/13.610	0.0/23.116
Mass flow rate (kg/s) (hot/average)	771./ 32034.	833./ 31972.

Table 2.3-2 Internal power multipliers.

CR=1			CR=0		
Relative	Average	Hot	Relative	Average	Hot
0.706	0.06218	0.00199	0.601	0.05282	0.00182
0.886	0.07804	0.00250	0.823	0.07233	0.00249
1.057	0.09310	0.00299	1.014	0.08912	0.00306
1.187	0.10455	0.00335	1.158	0.10177	0.00350
1.261	0.11106	0.00356	1.247	0.10960	0.00377
1.276	0.11239	0.00360	1.277	0.11223	0.00386
1.229	0.10825	0.00347	1.246	0.10951	0.00376
1.124	0.09900	0.00317	1.157	0.10169	0.00350
0.966	0.08508	0.00273	1.016	0.08929	0.00307
0.766	0.06747	0.00216	0.832	0.07312	0.00251
0.543	0.04783	0.00153	0.629	0.05528	0.00190

Table 2.3-3 Fuel conductivities (W/mK)

Temperature (K)	CR = 0	CR = 1
293	3.75	8.22
373	4.60	9.00
873	10.95	15.26
1173	13.70	20.14
1873	22.80	34.81

A simplification is made for modeling wire-wrap pressure drop in the salt core by adapting RELAP's Colebrook & White correlation to match the results given by the Cheng-Todreas correlation. This was done by varying the value of the surface roughness parameter in the Colebrook & White correlation so that the total pressure drop across the hot channel matched that in the subchannel model. Compared to the Cheng-Todreas correlation, this adapted Colebrook & White correlation has a weaker dependence on Reynolds's number; it tends to underpredict the friction factor for lower Reynolds numbers and overpredict it for higher Reynolds numbers. Over the range of Reynolds numbers for the reference core at steady state, the relative error is less than 5%, which is less than the uncertainty of each correlation. This simplification may affect the accuracy of modeling transient behavior, which involves low Reynolds numbers, but is needed because RELAP does not include an implementation of the Cheng-Todreas correlation.

To benchmark the RELAP core model, it was run at 2400 MWt and a total coolant flow rate of 3.28E4 kg/s, corresponding to the nominal steady state operating conditions. The pressure drop across the core and coolant and cladding temperatures were compared to the values obtained by the subchannel model. Results are given in Figures 2.3-2 and 2.3-3. As these figures show, there is extremely good agreement between the RELAP model developed and the subchannel model used to develop the core. The total pressure drop across the core matches within 2 kPa,

the matching coolant temperatures show the correct flow split has been achieved, and the peak cladding temperature matches within 1 °C.

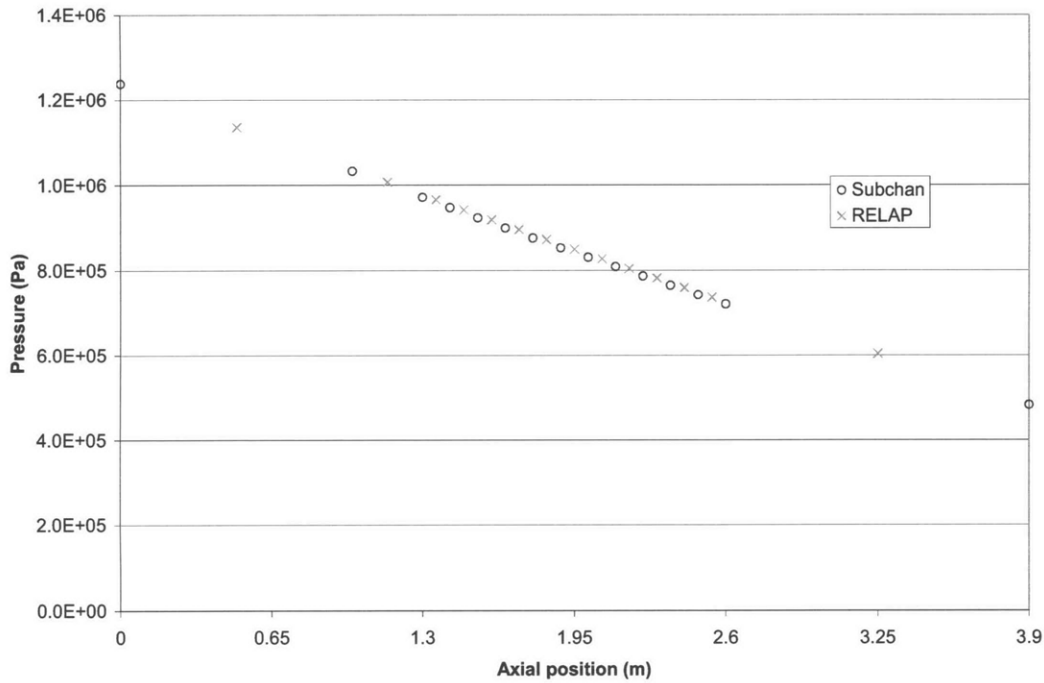


Figure 2.3-2 RELAP and subchannel model pressure drop comparison

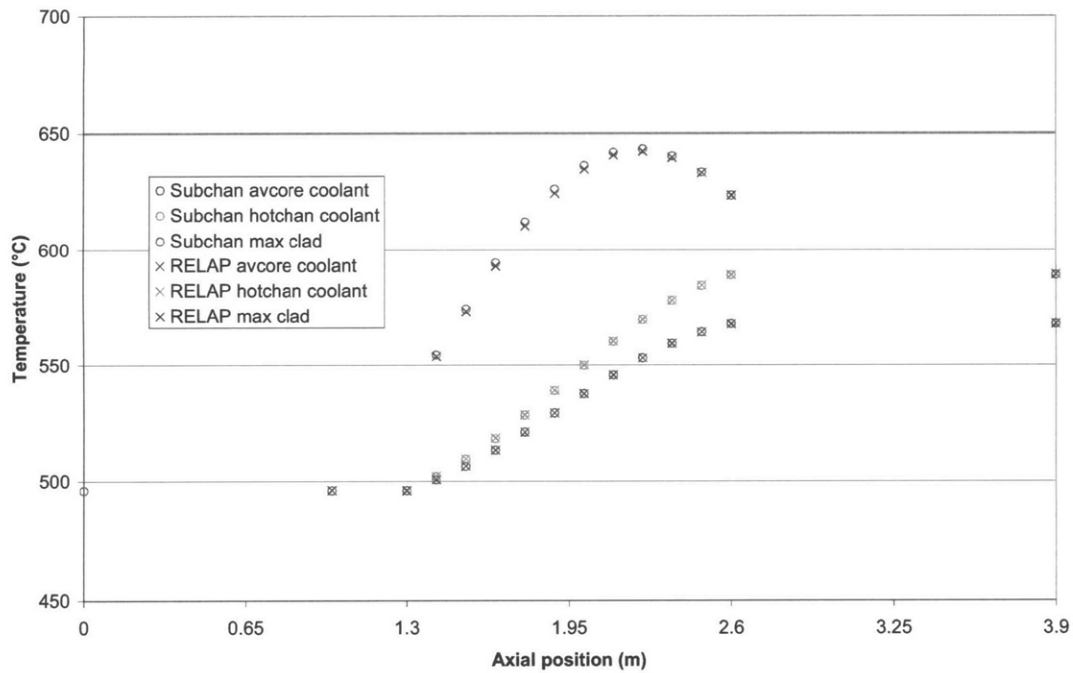


Figure 2.3-3 RELAP and subchannel temperature comparison

Lithium expansion module model

The hydrodynamic volumes and heat structures above the core corresponding to the gas plenums are structured to incorporate the presence of LEMs. They are divided into 10 axial nodes, each 0.13 meters long, to obtain a better estimate of time dependent heat transfer to the LEMs. A heat structure representing the LEM lithium reservoirs are present above the core average channel, alongside the heat structure for the gas plenums. These LEM heat structures consist of three radial nodes bounding two meshes: the first mesh extends from a radius of 0.0mm to 3.26mm and is composed of liquid lithium, and the second mesh extends from 3.26mm to 3.76mm and is composed of T-91 cladding material. Heat transfer in the liquid lithium is assumed to be due to conduction only, which is reasonable for liquid metals. Molten lithium properties are taken from Ohse, 1985. Heat transfer from the primary coolant to the LEMs is calculated using the same Gnielinski correlation used for the active core.

The average temperature of the liquid lithium at the centerline node of the LEM heat structure is calculated using RELAP control variables. This LEM reservoir temperature is converted to a reactivity insertion using a RELAP general table function, according to the temperature-reactivity curves specified in the section on lithium expansion module design, and is added to the contributions from the other reactivity feedbacks. The reactivity contribution of LEMs is also given in the reactivity parameter implementation subsection of this section.

Intermediate heat exchanger model

The salt reactor intermediate heat exchangers were designed using the spreadsheet model developed by Anna Nikiforova to design the lead reactor IHXs, with the primary side heat transfer correlation changed to the Gnielinski correlation, which is appropriate for high Prandtl

number liquid salts. A comparison of RELAP model results with the spreadsheet results is given in Table 2.3-4. The two sets of results do not match exactly because RELAP uses a slightly different correlation (Colebrook-White with fitted roughness term instead of McAdams) for pressure losses than the spreadsheet model. Also, the RELAP model incorporates the power lost through the RVACS and power gained from the reactor coolant pumps, meaning the RELAP heat exchangers do not reject exactly 600MW each. Nevertheless, results agree very well and validate the performance of the RELAP model.

Table 2.3-4 Comparison of spreadsheet and RELAP model results for the salt reactor intermediate heat exchangers

INPUT	Spreadsheet model	RELAP
Core power (MW_{th})	2400	
Salt mass flow rate (kg/s)	32800	
S-CO ₂ mass flow rate (kg/s)	12848	
Number of heat exchangers	4	
Target power transmitted in the IHX (per IHX) (MW_{th})	600	
Salt inlet temperature (°C)	569.	
Salt outlet temperature (°C)	496.	
S-CO ₂ inlet temperature (°C)	397.	
S-CO ₂ target outlet temperature (°C)	548.	
S-CO ₂ pressure (MPa)	19.7	
GEOMETRY		
Lattice	Triangular	
Number of tubes (per IHX)	21989	
Outer tube diameter (mm)	13	
Tube wall thickness (mm)	2.02	
Pitch to diameter ratio	1.23	
Inner IHX radius (r_i) (m)	2.551	
Outer IHX radius (r_o) (m)	4.465	
OUTPUT		
Calculated power (MW_{th})	600.0	601.4
Tube length (m)	6.78	6.90
Logarithmic temperature difference (°C)	49.9	N/A
S-CO ₂ velocity (average) (m/s)	16.8	17.2
Salt velocity (average) (m/s)	2.29	2.30
S-CO ₂ -side pressure loss (across IHX tubes) (kPa)	291	293
Salt-side pressure loss (kPa)	116	116

Virtual free level model

A limitation in the current RELAP5-3D version prevents the modeling of free levels for some coolants, including sodium and liquid salt. This limitation relates to partial pressure of coolant vapor in the gas-filled free space. Thus, the primary system model cannot include any air and must be completely filled with coolant. However, free levels are an integral part of the dual-free-level design, and free level positions must be known to determine if there is any overflow or if any components become exposed to air. Furthermore, the free level position in the outer annulus determines the amount of heat removed by the RVACS, since heat transfer to the guard vessel is much higher below the free level than above it. To account for free level positions without being able to explicitly model them, “virtual free levels” were built into the salt reactor RELAP model.

To construct the virtual free level model, first, volumes where air would have been present in the reactor vessel are removed from the model (parts of volumes 540 and 580, as well as all of volume 599). This way, the virtual free level model can contain the same amount of coolant and have the same thermal inertia as the actual reactor system. What results are two “ceilings” close to where the free levels should be, one above the chimney and one along the periphery of vessel, where the second riser and downcomer are. This is depicted in Figure 2.3-4, with the dot-dash lines indicating the positions of the ceilings.

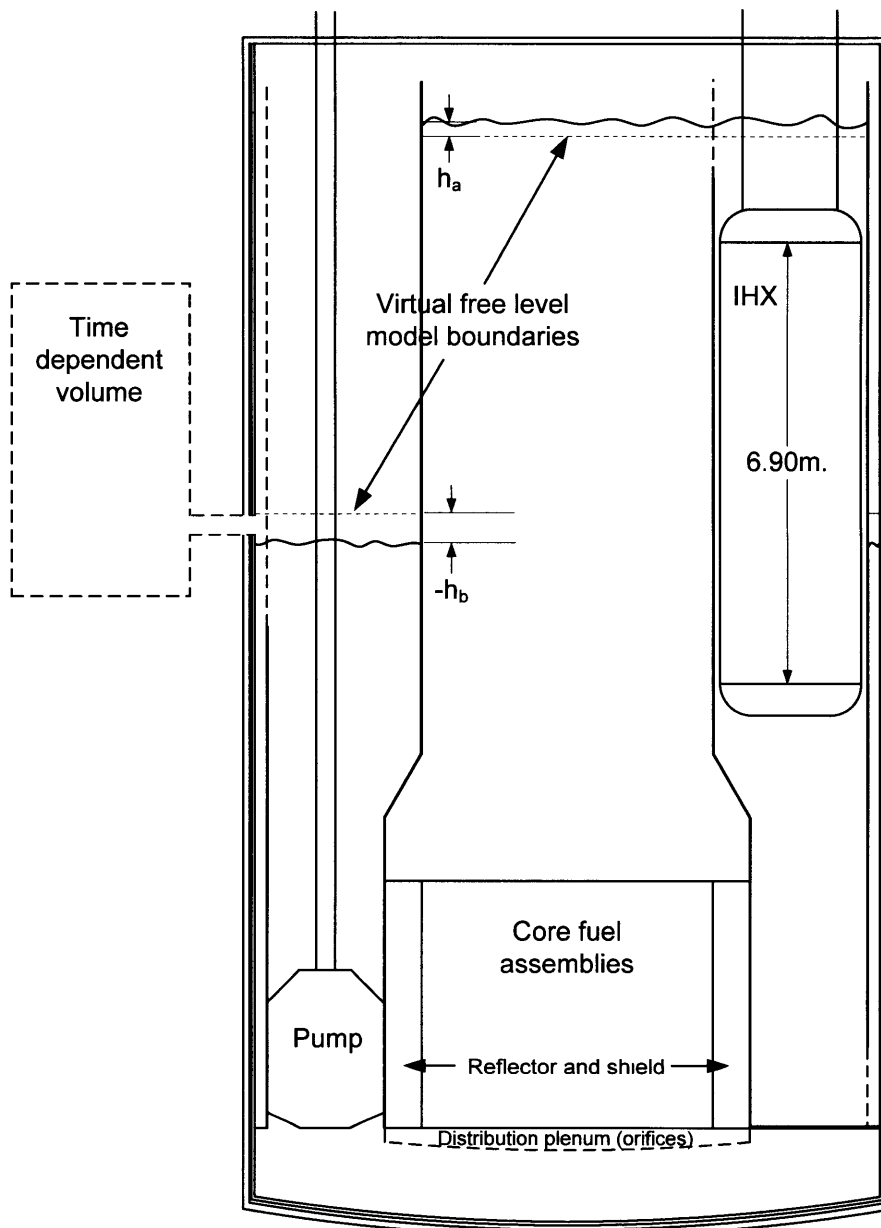


Figure 2.3-4 Vessel layout showing virtual free levels and time dependent volume

In order to allow for thermal expansion, a time-dependent volume (number 588) was connected to the top of peripheral riser; this functions similarly to a pressurizer by holding the pressure constant while allowing coolant to enter and exit. With this model, it is possible to calculate where the free level positions should be based on the pressures at the ceilings and total mass of coolant in the system. First, imagine that the “correct” free level positions exist at height h_a and

h_b above the ceilings, where the subscript a denotes the hot free level (chimney) and b denotes the cold free level (periphery); these heights can also be negative. Then, the total mass of coolant in the system is given by:

$$M_{total} = M_{model,i} + \rho_{a,i} A_a h_{a,i} + \rho_{b,i} A_b h_{b,i} = M_{model} + \rho_a A_a h_a + \rho_b A_b h_b \quad (2.3-1)$$

Here A is the area of the free level, ρ is the coolant density at the free level, and the subscript i represents initial or nominal conditions. M_{model} is the total mass of coolant modeled by RELAP, the actual total coolant mass M_{total} is equal to this mass plus the mass of the “virtual” coolant not modeled (Recall that vessel volume is initially chosen so that $M_{total} \approx M_{model,i}$). This equation takes into account the effect of thermal expansion; if the coolant heats up and expands, some of it will be pushed into the time-dependent volume, reducing the mass of coolant in the model. For the total coolant mass to remain constant, there must be more virtual coolant, i.e. the free levels must rise. To determine the relative position of the free levels, one can use the fact that both free levels are at the same atmospheric pressure:

$$P_a - \rho_a g h_a = P_b - \rho_b g h_b = P_{atm} \quad (2.3-2)$$

Here P_a and P_b are the coolant pressures measured by RELAP at the “ceilings” of the model; subtracting the hydrostatic pressure due to virtual coolant yields the pressure at the virtual free levels. Together these two equations allow one to solve for the free level positions h_a and h_b , since all other quantities can be derived from RELAP output.

The final component of the virtual free level model is connecting the position of the peripheral free level h_b to RVACS performance. This is necessary because heat transfer to the guard vessel

from the atmosphere above the coolant free level is much lower than from the coolant below the free level. This is done using a first-order approximation, depicted graphically in Figure 2.3-5. The diamonds show RVACS heat flux as a function of height along the periphery in the lead-cooled FCR reactor model, which uses an explicitly modeled free level. One can see that the heat flux decreases linearly below the free level, then falls dramatically to an approximately constant value above the free level, where heat transfer from the air inside the vessel to the guard vessel constitutes the primary thermal resistance. One can assume similar behavior exists for the salt reactor – a linear decrease below the free level then a small and constant value above it. In the virtual free level salt reactor model, only heat fluxes below the ceiling are computed by RELAP, however these heat flux values for the salt reactor can be extrapolated to the virtual free level position as shown by the dashed line in Figure 2.3-5. Above the free level the heat flux is assumed to have the same constant value as for the lead reactor, which is reasonable since the air in the salt and lead reactor vessels will be similar. The total heat removed by the RVACS is then the sum over the modeled heat fluxes and the extrapolated amount, which is the L-shaped area under the dashed curve in Figure 2.3-5. Control variables are used to perform the extrapolation described and calculate the total amount of additional heat that should be removed by the RVACS. To actually remove the heat from the coolant in the virtual free level model, an artificial heat structure is set up at the top of the peripheral riser that rejects the amount of heat calculated by these control variables.

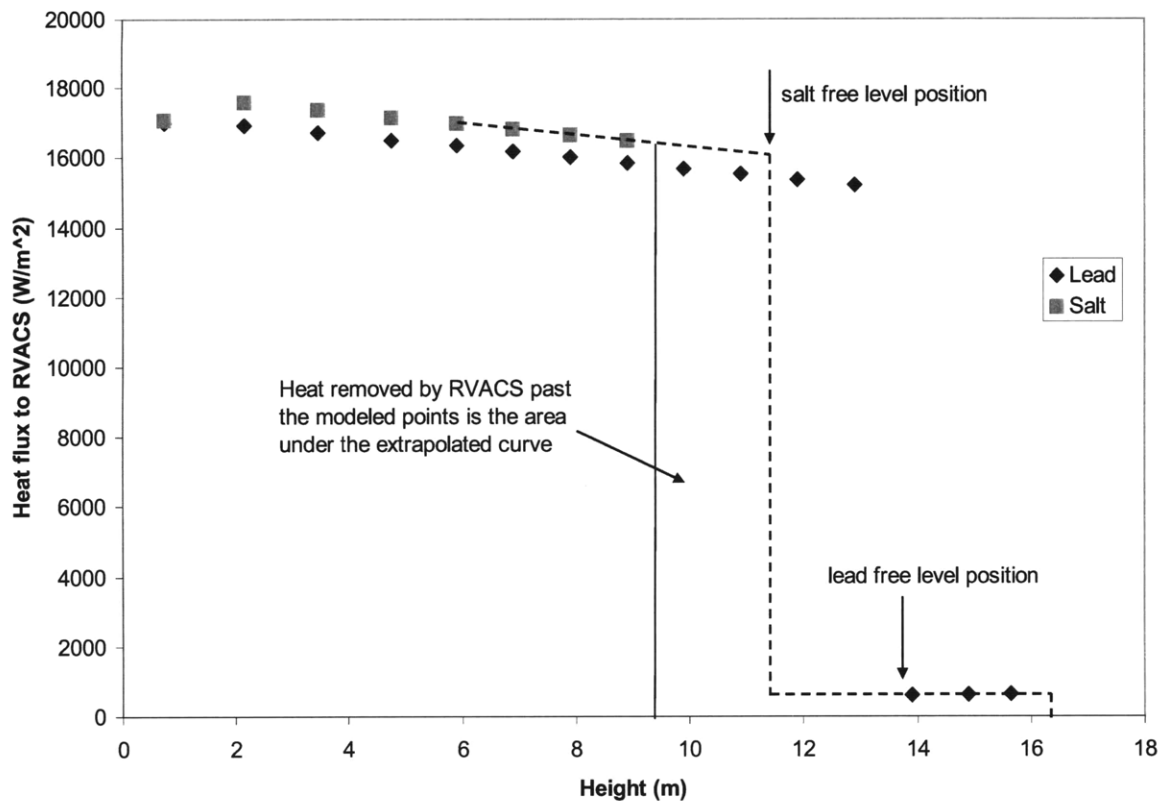


Figure 2.3-5 RVACS heat flux as a function of position

To benchmark the virtual free level model, it was implemented in the lead-cooled reactor RELAP model and results from this model were compared to those of the original model. The testing demonstrated that heat fluxes from the coolant to the RVACS were nearly identical for the virtual free level model and the original (explicit free level) model, (Figure 2.3-6) showing that the linear extrapolation method employed is accurate. While the virtual free level model possesses the same thermal inertia as the system being modeled, it does not account for the movement of coolant masses. For example, during a loss of flow accident the coolant level will fall in the chimney and rise in the periphery; in the virtual free level model this movement is tracked but no actual coolant migration occurs. Finally, there is a small error introduced by the movement of coolant into and out of the time dependent volume due to thermal expansion; this

amount is less than 5% for a bounding accident and therefore does not significantly impact results.

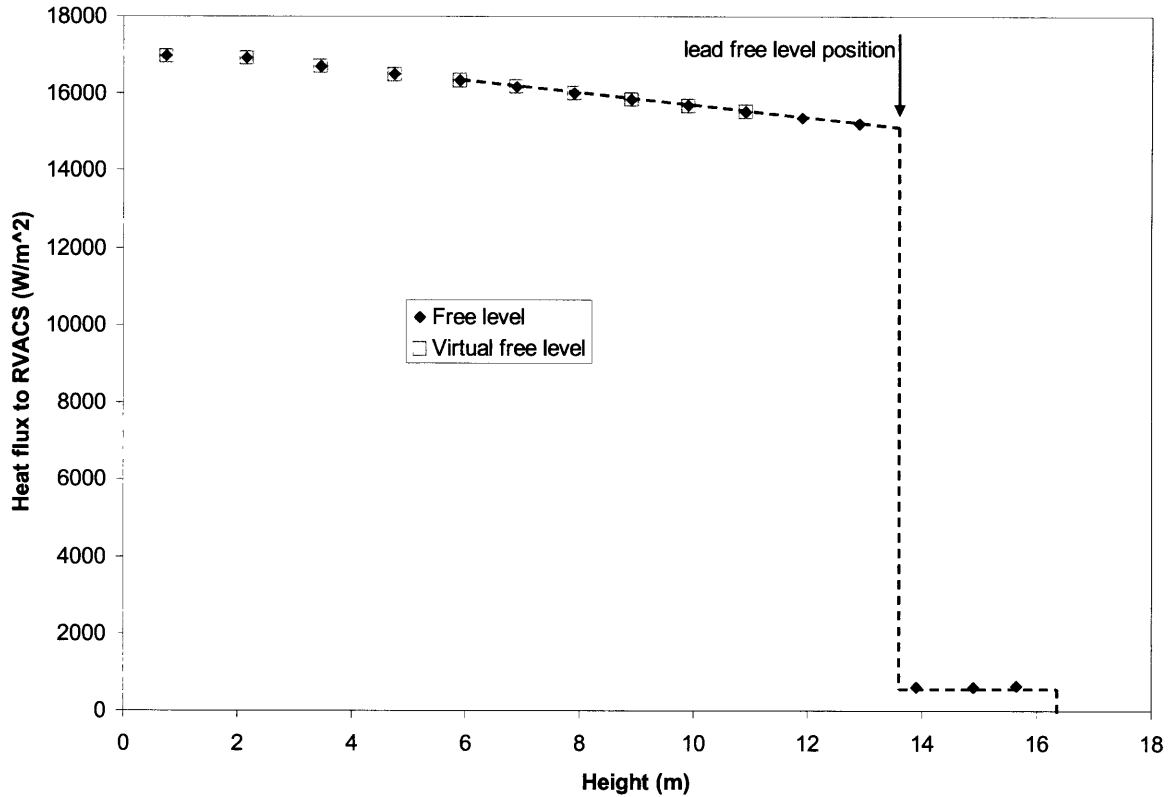


Figure 2.3-6 RVACS heat flux for explicit- and virtual-free-level models

PSACS modeling

The Passive Secondary Auxiliary Cooling System (PSACS) is a novel decay heat removal system designed for the lead-cooled flexible conversion ratio reactor [Todreas & Hejzlar, 2008b]. The PSACS consists of an passive auxiliary heat exchanger (PAHX) connected to each power conversion system train via valves, which can discharge heat into large water tanks during transients. Adjusting the design of the PAHX and size of the PSACS water tanks has a large effect on transient performance of the liquid-salt cooled FCR reactor.

The original dimensions for the lead FCR reactor PSACS are given in Table 2.3-5. Because the salt PSACS designs were derived from this original lead design, the different iterations are named based on the relative power removed by the PSACS system and the capacity of the PSACS water tanks. The different motivations for resizing the PSACS for the salt system are explained in the transient analysis section.

Table 2.3-5 Salt reactor PSACS design iterations*

Design iteration		Original lead design	Previous salt design	Reference salt design
Design designation		200% power, 1.0x tank size	100% power, 1.1x tank size	60% power, 0.75x tank size
Water Tank	Height (m)	12.0	~13.2	~9.0
	Diameter (m)	6.0	~6.0	~6.0
Passive Auxiliary Heat Exchanger (PAHX)	Number of tubes	700	~500	~350
	Tube length (m)	4.0	~3.0	~2.4
	Inner diameter – CO ₂ side (m)	8.00E-03	8.00E-03	8.00E-03
	Tube thickness (m)	2.80E-03	2.80E-03	2.80E-03
	Outer diameter – water side (m)	1.36E-02	1.36E-02	1.36E-02
P/D ratio		3	3	3

*Parameters for the salt designs are estimates; see simplifications below

The original lead PSACS design was modeled explicitly in RELAP as hydrodynamic volumes and heat structures with the geometry given in Table 2.3-5. Two simplifications were used to model the subsequent PSACS designs. First, RELAP code runs stall when the PSACS tanks are nearing depletion; so it was necessary to introduce a PSACS trip (closure of the PSACS valves) shortly before this occurs in order for RELAP runs to proceed past this point. To simplify the modeling process, the PSACS tanks were made arbitrarily large in the model so the code would not stall, and the PSACS trip time was set to the desired time for the PSACS to run out of water.

The physical size of the PSACS tanks could then be calculated from the amount of energy removed by the PSACS system while it was operating.

The second simplification employed has to do with modeling of the PAHXs. Different sized PAHXs were modeled by first removing a train from the original PSACS design and then by adjusting the heat structure length parameter of the PAHX heat structures. Removing one of the two operating trains, rather than downsizing each train by 50%, was necessary because RELAP encounters computation difficulties modeling individual low power PSACS trains. The resulting single train in the model functions equivalently to two half-sized PSACS trains. Changing the heat structure length in the PAHX heat structures is a convenient way of scaling the overall PSACS power capacity. Decreasing the heat structure length parameter corresponds physically to either reducing the heat transfer area or increasing the thermal resistance of the PAHX tubes, and has no effect on pressure losses in the system. In an actual system, downsizing of the PAHXs would be likely to occur via reducing the number and length of the PAHX tubes, which is reflected in Table 2.3-5. Since use of the above two simplifications allows one to avoid explicitly modeling both PSACS water tank and PAHX geometries, the values given for the salt designs in Table 2.3-5 are given as estimates.

2.4 Salt reactor reactivity feedback implementation

In addition to steady state simulations of reactor performance, RELAP5-3D is also able to perform transient simulations using inputted reactivity data. For the purposes of RELAP modeling, beginning of life (BOL) reactivity data are used because they are more challenging in terms of transient response. Reactivity calculations were performed by Eugene Shwageraus, a

post doctorate working on the same NERI project and are documented in Todreas & Hejzlar [2008b].

Coolant temperature/density

The reactivity response to varying coolant temperature in the CR=1 and CR=0 cores is shown in Figures 2.4-1 and 2.4-2. Values implemented in RELAP are taken from the fitted equations and are given in Table 2.4-1. The “average” value of core coolant density used by RELAP to determine the reactivity response is calculated using power-squared weighing, following the power multipliers given in Table 3B.2-12.

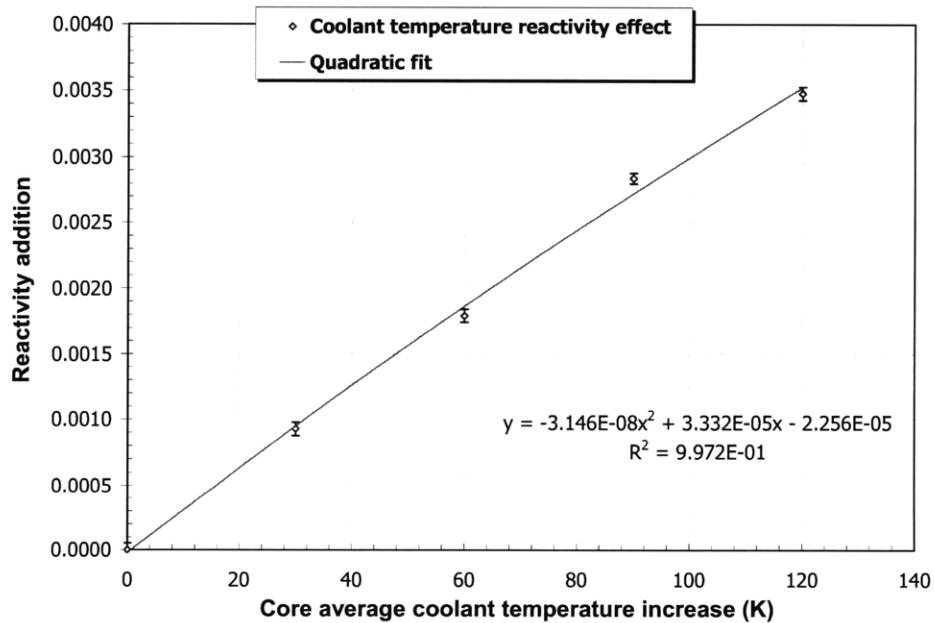


Figure 2.4-1 Reactivity insertion due to coolant thermal expansion, CR=1 BOL [Todreas & Hejzlar, 2008a]

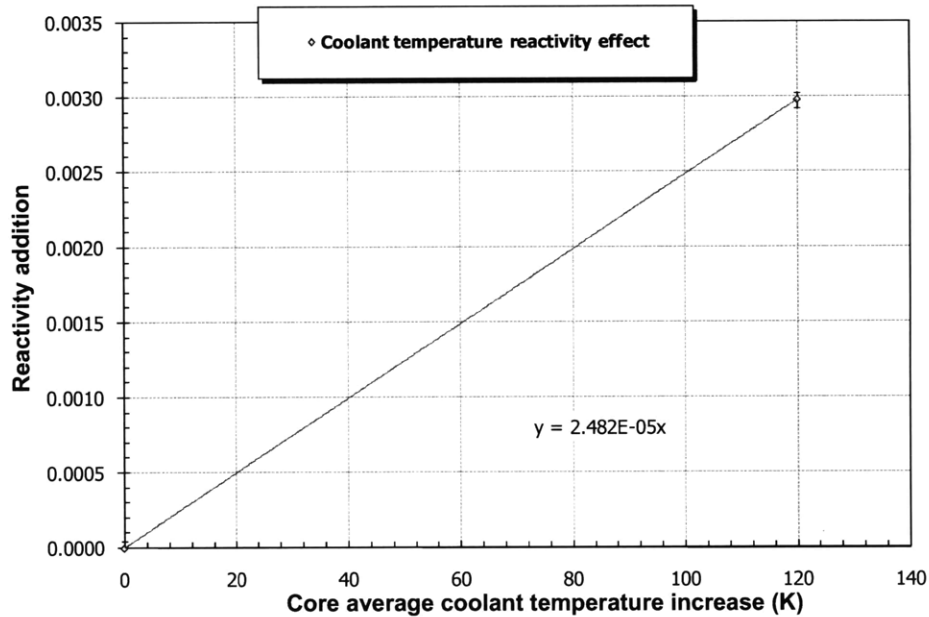


Figure 2.4-2 Reactivity insertion due to coolant thermal expansion, CR=0 BOL [Todreas & Hejzlar, 2008a]

Table 2.4-1 Salt reactor coolant density reactivity model for RELAP5-3D

T(°C)	Salt density (kg/m ³)	CR=1 reactivity (\$) $\beta=0.00389$	CR=0 reactivity (\$) $\beta=0.00298$
853	1596.4	1.907E+00	2.665E+00
833	1611.9	1.836E+00	2.499E+00
813	1627.5	1.759E+00	2.332E+00
793	1643.0	1.675E+00	2.166E+00
773	1658.6	1.584E+00	1.999E+00
753	1674.2	1.487E+00	1.832E+00
733	1689.7	1.384E+00	1.666E+00
713	1705.3	1.274E+00	1.499E+00
693	1720.8	1.158E+00	1.333E+00
673	1736.4	1.035E+00	1.166E+00
653	1752.0	9.056E-01	9.995E-01
633	1767.5	7.699E-01	8.329E-01
613	1783.1	6.277E-01	6.663E-01
593	1798.6	4.790E-01	4.997E-01
573	1814.2	3.239E-01	3.332E-01
553	1829.8	1.623E-01	1.666E-01
533	1845.3	-5.799E-03	0.000E+00
513	1860.9	-1.803E-01	-1.666E-01
493	1876.4	-3.614E-01	-3.332E-01
473	1892.0	-5.488E-01	-4.997E-01
453	1907.6	-7.428E-01	-6.663E-01
433	1923.1	-9.432E-01	-8.329E-01
413	1938.7	-1.150E+00	-9.995E-01

Fuel temperature (Doppler)

The reactivity response to varying coolant temperature in the CR=1 and CR=0 cores is shown in Figures 2.4-3 and 2.4-4. Values implemented in RELAP are taken from the fitted power equations and are given in Table 2.4-2. The “average” value of fuel temperature used by RELAP to determine the reactivity response is calculated using power-squared weighing, following the power multipliers given in Table 2.3-2.

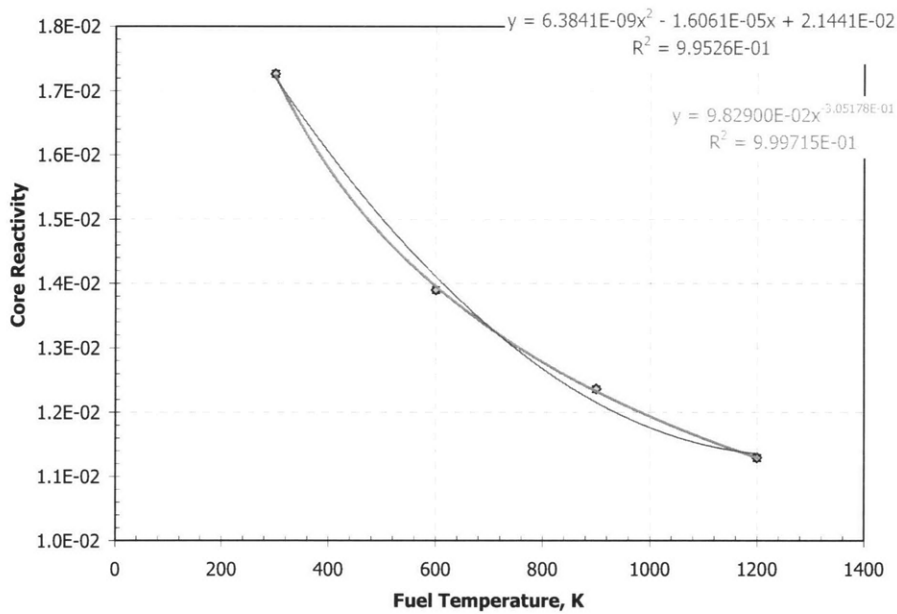


Figure 2.4-3 Reactivity insertion due to fuel temperature increase, CR=1 BOL [Todreas & Hejzlar, 2008a]

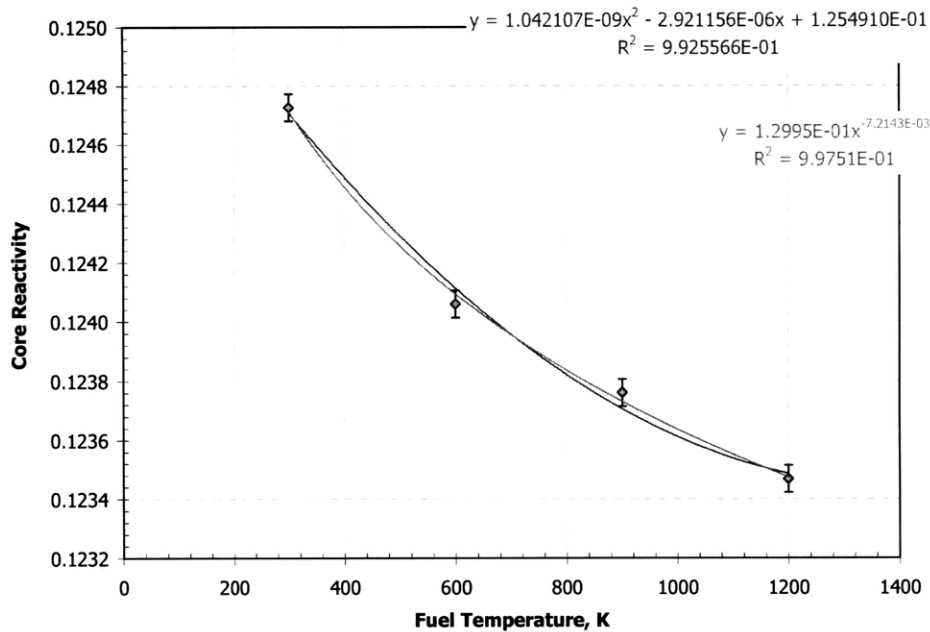


Figure 2.4-4 Reactivity insertion due to fuel temperature increase, CR=0 BOL [Todreas & Hejzlar, 2008a]

Table 2.42 Salt reactor fuel temperature reactivity model for RELAP5-3D

T (K) of fuel	CR=1 reactivity (\$) $\beta=0.00389$	CR=0 reactivity (\$) $\beta=0.00298$
300.0	0.0	0.0
400.0	-0.4225	-0.13667
600.0	-0.9950	-0.3709
900.0	-1.5625	-0.6759
1000.0	-1.7128	-0.7707
1200.0	-1.9789	-0.9540
1500.0	-2.3200	-1.2174
1600.0	-2.4229	-1.3030
1800.0	-2.6168	-1.4715

Core radial expansion and control rod drive expansion

Constant values are used for the core radial expansion and control rod drive expansion coefficients. For core radial expansion, the CR=1 and CR=0 reactivity coefficients were calculated to be -0.00159\$/K and -0.00229\$/K respectively. These reactivity coefficients are based on the average core coolant temperature, defined as the linear average of the coolant

temperatures in the 11 axial meshes of the “average” channel in the core. The control rod drive expansion coefficient is conservatively assumed to be zero.

Lithium expansion modules

Results from the lithium expansion module design were incorporated into RELAP5-3D as shown in Figure 2.4-5 and Table 2.4-3. As described in Section 4.3, these curves were obtained by taking the characteristic cosine shape of the LEM reactivity response and expanding it to fit the needed temperature range, as well as to ensure a sufficiently low coolant reactivity coefficient at steady state. These curves do not incorporate a bottlenecked LEM design, which would reduce the positive reactivity from lower LEM temperatures. However, since none of the bounding accidents considered result in the LEM reservoir temperature decreasing, this has no effect on the results obtained. As described in Section 2.3 of this thesis, the LEM reservoir temperature is calculated through the use of heat structures which explicitly model the LEMs above the core.

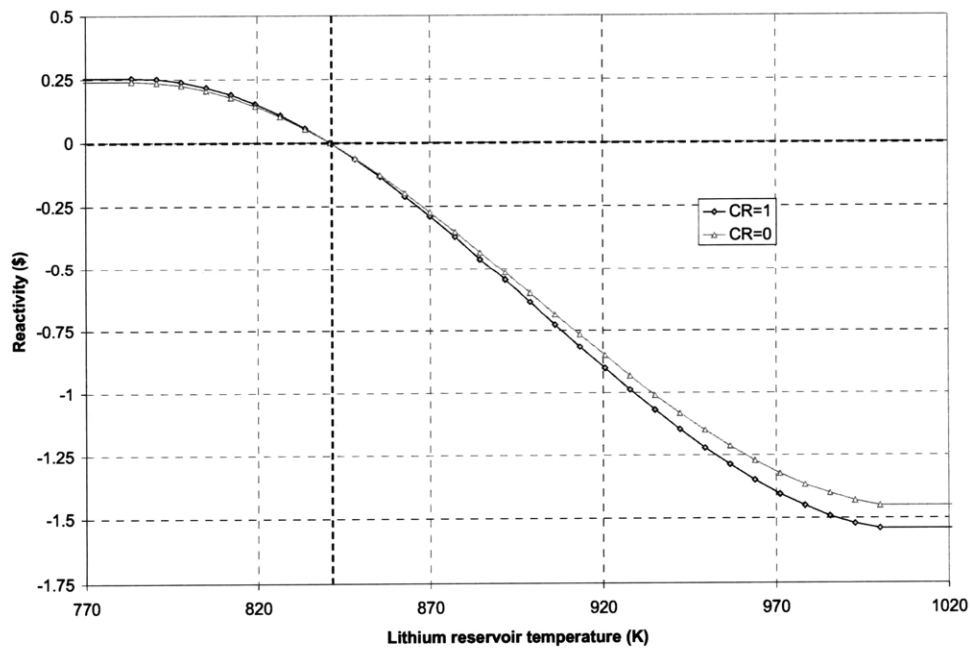


Figure 2.4-5 Reactivity insertion due to lithium expansion modules (dashed lines indicate steady state values)

Table 2.4-3 Salt reactor LEM reactivity model for RELAP5-3D

Temperature (K) of LEM reservoir	CR=1 reactivity (\$) $\beta=0.00389$	CR=0 reactivity (\$) $\beta=0.00298$
676	2.56E-01	2.41E-01
783	2.56E-01	2.41E-01
791	2.52E-01	2.37E-01
798	2.39E-01	2.25E-01
805	2.19E-01	2.06E-01
812	1.90E-01	1.79E-01
819	1.53E-01	1.44E-01
827	1.10E-01	1.03E-01
834	5.79E-02	5.48E-02
841	0.00E+00	0.00E+00
848	-6.42E-02	-6.06E-02
856	-1.33E-01	-1.27E-01
863	-2.11E-01	-1.97E-01
870	-2.89E-01	-2.73E-01
877	-3.71E-01	-3.50E-01
884	-4.60E-01	-4.33E-01
892	-5.45E-01	-5.15E-01
899	-6.34E-01	-5.98E-01
906	-7.27E-01	-6.85E-01
913	-8.16E-01	-7.67E-01
921	-9.02E-01	-8.50E-01
928	-9.87E-01	-9.32E-01
935	-1.07E+00	-1.01E+00
942	-1.15E+00	-1.08E+00
949	-1.22E+00	-1.15E+00
957	-1.29E+00	-1.21E+00
964	-1.35E+00	-1.27E+00
971	-1.41E+00	-1.32E+00
978	-1.45E+00	-1.37E+00
986	-1.49E+00	-1.40E+00
993	-1.52E+00	-1.43E+00
1000	-1.54E+00	-1.45E+00
1276	-1.54E+00	-1.45E+00

3. Salt Selection

The choice of a primary coolant is central to the design of a nuclear reactor since it directly affects reactor physics, thermal hydraulic performance, and corrosion behavior. An ideal fast reactor coolant would be chemically compatible with air, water, CO₂, and all structural materials, weakly moderating, and a poor absorber over the spectrum of interest. Thermal hydraulically it should have high heat capacity, high thermal conductivity, and low viscosity. More practical issues such as coolant cost, opacity/transparency, and ease of chemical control also need to be considered. Because choice of coolant is so important, a significant portion of this project was spent identifying the most promising coolant salts and characterizing their properties.

3.1 Preliminary fluoride selection

There are a large number of primary coolant salt options available for liquid salt reactors, each with different physical, chemical, and nuclear properties. Many possible coolant salts are listed in Williams et al., [2006a], Williams and Toth [2006b] and Forsberg [2004], selected based on chemical stability and a reasonably low (<525°C) melting point. The list of considered salts and their thermal-hydraulic properties are given in Table 3.1-1.

Table 3.1-1 Physical properties of candidate coolant salts⁵

Salt (composition)	T _{melt} (°C)	μ at 550°C (kg/m-s) ¹	k (W/m-K) ²	Th.exp. c. (%/K) ³	Density (kg/m ³) ³	c _p (cal /gK) ⁴	ρc_p (cal/cm ³ K)
Alkali fluorides							
⁷ LiF-NaF-KF (46.5-11.5-42)	454	6.3E-3	0.6 [0.85]	0.034 [0.029]	2129 [2070]	0.45 [0.387]	0.96
⁷ LiF-RbF (44-56)	475	6.2E-3	[0.53]	0.034 [0.029]	2772 [2850]	0.284 [0.226]	0.79
⁷ LiF-NaF-RbF (42-6-52)	435		[0.54]	[0.029]	[2816]	[0.236]	0.66
Beryllium fluorides							
⁷ LiF-BeF ₂ (67-33)	458	11.1E-3	1.0 [1.04]	0.024 [0.021]	2012 [1980]	0.577 [0.566]	1.16
NaF-BeF ₂ (57-43)	340	18.1E-3	[0.80]	0.018 [0.022]	2067 [2123]	0.52 [0.440]	1.07
⁷ LiF-NaF-BeF ₂ (31-31-38)	315		[0.89]	[0.022]	[2066]	[0.489]	1.01
Zirconium fluorides							
⁷ LiF-ZrF ₄ (51-49)	509		[0.41]	[0.029]	[3230]	[0.292]	0.94
NaF-ZrF ₄ (59.5-40.5)	500	11.2E-3	[0.42]	0.028 [0.029]	3166 [3095]	0.28 [0.275]	0.89
KF-ZrF ₄ (58-42)	390	7.6E-3	[0.38]	[0.030]	[2928]	[0.251]	0.73
RbF-ZrF ₄ (58-42)	410		[0.32]	[0.030]	[3371]	[0.200]	0.67
⁷ LiF-NaF-ZrF ₄ (26-37-37)	436	16.6E-3	[0.45]	0.028 [0.028]	2914 [3055]	0.35 [0.296]	1.02
NaF-KF-ZrF ₄ (10-48-42)	385		[0.38]	[0.030]	[2956]	0.26 [0.255]	0.77
NaF-RbF-ZrF ₄ (8-50-42)	400		[0.33]	[0.030]	[3342]	[0.207]	0.69
Chlorides							
NaCl-MgCl ₂ (63-37)	475						
NaCl-MgCl ₂ (58-42)	445	1.6E-3	(0.43)	0.025	2018	0.258 [0.262]	0.52
KCl-MgCl ₂ (68-32)	426	2.2E-3	(0.39)	0.024	1994	0.276 [0.229]	0.55
⁷ LiCl-KCl- MgCl ₂ (9-63-28)	402						
NaCl-KCl- MgCl ₂ (30-20-50)	396	2.1E-3	(0.39)	0.043	1798	[0.250]	0.45

Salt (composition)	T _{melt} (°C)	μ at 550°C (kg/m-s) ¹	k (W/m-K) ²	Th.exp. c. (%/K) ³	Density (kg/m ³) ³	c _p (cal/gK) ⁴	ρc_p (cal/cm ³ K)
⁷ LiCl-KCl (59.5-40.5)	355	1.8E-3	0.28-0.69 (0.43)	0.062	1399	0.287 [0.289]	0.40
⁷ LiCl-KCl-MgCl ₂ (55-40-5)	323						
⁷ LiCl-RbCl (58-42)	313		(0.39)	0.029	2363	0.213 [0.212]	0.50

¹ Values are only given for salts with measured and known viscosity temperature dependence; values are evaluated at 550°C. Multiply by 1000 to obtain centipoises.

² Very few measured values available; values in brackets are estimated using the Khoklov correlation [Williams et al., 2006a] at 550°C, values in parenthesis are estimated using a mole fraction average. There is very little data on salts containing ZrF₄ and MgCl₂.

³ Percent change in density per degree, and density, are evaluated at 550°C. Values in brackets are calculated using the method of additive molar volumes.

⁴ Measured values are taken at 700°C; values in brackets are calculated from the Dulong-Petit prediction [Williams et al., 2006a]. Temperature dependence is small and typically neglected during preliminary calculations.

⁵ Fluoroborates are not included because of the need for isotopic enrichment of boron.

In the first screening phase, chloride salts were not studied for use as primary coolants for the liquid salt FCR reactor for three reasons. First, and most important, Cl-35 absorbs thermal neutrons to produce radioactive Cl-36, with a 300,000 year half life that may create an undesirable radwaste problem. Second, compared to fluoride salts, chloride salts are difficult to purify and to keep pure during reactor operation. Finally, chloride salts have not been as extensively studied as fluoride salts for reactor purposes.

Even considering only fluoride salts, there are a large number of ways that constituent salts can be combined into binary and ternary mixtures. These can be divided into several groups: salts containing only alkali fluorides, salts containing BeF₂, and salts containing ZrF₄. Fluoroborate salts with a BF₄ anion were also considered but were excluded because the high absorption of boron-10 would necessitate isotopic separation.

From this collection of available salts, a large number can be eliminated based on nuclear properties. Primary coolant salts need to have a small absorption cross section, which excludes salts containing lithium and boron, since Li-6 and B-10 have large absorption cross sections over the spectrum of interest. While isotopic separation is possible, it would be extremely expensive at the scale required. Rubidium salts also have a large absorption cross section, and there is currently no world market for rubidium, so salts containing rubidium were excluded as well.

Eliminating salts containing lithium and rubidium leaves one beryllium fluoride: NaF-BeF₂, and several zirconium salts. The zirconium salt NaF-ZrF₄ has a melting temperature of 500°C, too close to the cladding temperature limit of 650°C to allow an appreciable margin to freezing. Therefore, the three fluoride salts selected for more extensive study were NaF-BeF₂, KF-ZrF₄, and NaF-KF-ZrF₄.

The thermal-hydraulic characteristics of an FCR reactor using NaF-BeF₂ as the primary coolant were investigated using the spreadsheet subchannel model. Thermal hydraulic performance was expected to be good for this salt, on account of its relatively high thermal conductivity and heat capacity. However, the salt's extremely high viscosity resulted in near-laminar flow in the core, which yielded unattractively low power densities. Furthermore, neutronics analyses revealed that NaF-BeF₂ coolant would be too moderating, leading to unacceptable neutronic performance. This left KF-ZrF₄ and NaF-KF-ZrF₄ as the salts of primary interest. While both these remaining salts have similar properties, the ternary salt is the most promising fluoride candidate because of its lower melting point. It should be noted this selected salt contains potassium, the chief isotope of which, K-39, is activated via an (n, α) reaction to form radioactive Cl-36, the same isotope

that makes chloride salts problematic. However, potassium does not create as large of a radwaste problem as chlorine because less Cl-36 is produced, and because it is fairly easy to remove chlorine impurities from a fluoride salt.

Thermal hydraulic analyses using the spreadsheet subchannel model were performed for a NaF-KF-ZrF₄ cooled core. Assumed properties for the salt are given in Table 3.1-2, the core geometry used is given in Table 3.1-3, and analysis results are shown in Table 3.1-4. At the time of fluoride salt analyses, LEMs were not part of the reference design, so the geometry studied still employed an extremely tight lattice (P/D = 1.086) in order to reduce the coolant temperature coefficient.

Table 3.2-2 Assumed NaF-KF-ZrF₄ physical properties

Property	Value	Method of obtaining
Melting point (°C)	385	Measured value
Density	$3450 - 0.89 * T(^{\circ}C)$	Method of additive molar volumes
Thermal expansion coefficient (% vol/K)	0.030	Method of additive molar volumes
Dynamic viscosity (cP)	$0.159 * \exp(3179/T(K))$	Measured value for KF-ZrF ₄
Thermal conductivity (W/mK)	0.32	Value for KF-ZrF ₄ , estimated from mole fraction average
Heat capacity (cal/gK)	0.26	Dulong-Petit prediction

Table 3.2-2 Reference fluoride core geometry

Total fuel pin length (m)	3.9
Fuel pin heated length (m)	1.3
Pin outer diameter (mm)	7.52
Pin cladding thickness (mm)	0.63
Pin pitch P(mm)	8.17
Pin P/D	1.086
Wire diameter (mm)	0.65
Wire axial pitch H (m)	0.184
H/D	24.5
Number of pins along each edge of the assembly	12
Number of pins per assembly	397
Assembly wall – fuel pin gap thickness (mm)	0.65
Assembly wall thickness (mm)	3.94
Assembly – assembly gap thickness (mm)	2.22
Assembly pitch (m)	0.1746
Number of fuel assemblies in core	691

Table 3.2-3 CR=1 NaF-KF-ZrF₄ salt core characteristics.

Core	NaF-KF-ZrF ₄ (CR=1)
Total Power (MWt)	1650
Maximum power density (kW/l)	70
Average power per pin (W)	6.0E3
Coolant inlet temperature (°C)	485
Average coolant outlet temperature (°C)	528*
Pressure drop across core (Pa)	1.50E6
Coolant mass flow rate through core (kg/s)	3.6E4
Pumping power through core (MW)	18
Hot channel characteristics:	
Coolant velocity (m/s)	2.9
Reynolds number	1700–2300
Nusselt number	15–25
Heat transfer coefficient (W/m ² K)	2200-3500
Peak cladding temperature (K)	650

*unorificed value; hot assembly outlet temperatures is 539°C

Table 3.2-3 shows that even with a very high core pressure drop of 1.5 MPa, 50% higher than the soft constraint on pressure drop, use of the selected fluoride salt could only yield a core power density of 70 kW/l, much less than the target power density of 100 kW/l. This difficulty in

meeting thermal hydraulic requirements, along with challenges addressing the coolant temperature coefficient of fluoride salts, spurred the investigation of chlorides. Even when LEMs were subsequently implemented, allowing the salt lattice to be loosened to a P/D of 1.19, the selected fluoride salt was still only able to achieve a power density of 70 kW/l at a core pressure drop of 700 kPa. In comparison, the most promising chloride salt, discussed below, is able to achieve a power density of over 130 kW/l for this geometry and pressure drop.

3.2 Final chloride selection

Potential chloride salts were screened in a similar manner as fluoride salts. Salts containing lithium were eliminated because the high absorption cross section of Li-6 would necessitate expensive isotopic enrichment on a large scale. This left NaCl-MgCl₂, KCl-MgCl₂, and NaCl-KCl-MgCl₂ as the three salt systems of interest. For the NaCl-MgCl₂ system, there is only enough information available about the 58% NaCl – 42% MgCl₂ eutectic to permit analysis. These three salt mixtures all have similar thermal hydraulic and neutronic properties. Since thermal hydraulics are limiting for fluorides, thermal hydraulics analyses were performed for each salt to determine the most promising candidate. Results for a near-finalized core design very similar to the reference design in this thesis are given in Table 3.2-1. Fixed conditions were used, including a 700 kPa core pressure drop and a coolant inlet temperature 100°C above each salt's melting point. Included for comparison are values for the most promising fluoride candidate, NaF-KF-ZrF₄.

Table 3.2-1 T-H analysis results of selected coolant salts

Coolant salt	NaF-KF-ZrF ₄	NaCl-MgCl ₂	KCl-MgCl ₂	NaCl-KCl-MgCl ₂
Total power (MWt)	1302	2076	2301	2516
Maximum power density (W/cc)	70	112	124	135
Average power per pin (W)	7.50E+03	1.20E+04	1.33E+04	1.45E+04
Coolant inlet temperature (°C)	496	545	526	496
Average coolant outlet temperature (°C)	532	598	583	572
Hot assembly outlet temperature (°C)	535	602	588	578
Coolant mass flow rate through core (kg/s)	3.31E+04	3.63E+04	3.47E+04	3.28E+04
Pumping power (MW)	8	13	12	12
Hot channel/hot spot characteristics:				
Inlet coolant velocity (m/s)	2.70	4.49	4.33	4.38
Reynolds number	3.19E+03	1.95E+04	1.38E+04	1.31E+04
Nusselt number	39.7	114.8	102.6	92.6
Heat transfer coefficient (W/m ² K)	3.86E+03	1.50E+04	1.22E+04	1.10E+04
Maximum film ΔT (K)	103.7	42.6	58.2	70.5
Peak cladding temperature (K)	650	650	650	650

Fluoride salts are unable to meet the desired power density target of 100 kW/l because of thermal hydraulic limitations; specifically, higher power densities would cause the cladding temperature limit of 650°C to be exceeded. Chloride salt thermal hydraulic performance is greatly superior to that of fluoride salts. The primary reason for this is an approximately five times lower viscosity over the operating temperatures of interest. Low viscosity improves coolant flow rate and heat transfer, as seen by the higher coolant velocities and heat transfer coefficients shown in Table 3.2-1. Each of the selected chloride salts performs similarly well, with the ternary NaCl-KCl-MgCl₂ yielding the best performance because of its lower melting point. Moreover, NaCl-KCl-MgCl₂ yields reactor physics benefits over the fluoride as well, since it has a significantly smaller coolant temperature reactivity coefficient and is less moderating. Because of its superior thermal hydraulic and neutronic performance, the ternary salt NaCl-KCl-MgCl₂ was selected as the most promising salt candidate for the liquid salt FCR reactor, and is the salt used in the reference design.

3.3 Properties of the most promising salt candidate

The assumed properties for NaCl-KCl-MgCl₂ are given in Table 3.3-1, with summaries of the methods used to obtain them.

Melting point, density, and viscosity are all given in a 1960 BNL report (BNL-627) on fused chloride salts. Because density and viscosity are relatively straightforward to measure, the values given can be used with reasonable certainty.

Heat capacity is estimated using a mole fraction average, using the constituent values recommend in Janz's Molten Salts Handbook [1967]: 22 W/mol-K for MgCl₂, 16 W/mol-K for NaCl and KCl. A simple mole fraction average is used because non-ideal behavior may be complex and there is insufficient data to predict such behavior. The value obtained is slightly less than that given by the Dulong-Petit prediction, which gives a heat capacity of 8 W/mol-K per atom.

Table 3.3-1 Assumed NaCl-KCl-MgCl₂ (30-20-50) physical properties.

Property	Value	Method of obtaining
Melting point (°C)	396	Measured value from BNL report*
Density (kg/m ³)	2260 – 0.778*T(°C)	Measured value from BNL report*
Thermal expansion coefficient (% vol/K)	0.043	Measured value from BNL report*
Dynamic viscosity (cP)	exp(3040/T(K)-2.96)	Measured value from BNL report*
Thermal conductivity (W/m-K)	0.39	Mole fraction average for KCl-MgCl ₂ (50-50)
Heat capacity (cal/gK)	0.24	Mole fraction average

* Raseman et. al. [1960].

Thermal conductivity is the property with the most uncertainty, largely because there is almost no thermal conductivity data on MgCl_2 or its mixtures. Only one 1974 paper by Polyakov and Gildebrandt [1974] was found to measure conductivities of MgCl_2 salts, however the thermal conductivities it quotes for KCl, a commonly measured salt, are anomalously high. Several approaches were taken to produce a range of estimates for thermal conductivity. First, one can use the approach taken by Williams and Toth [2006b] to estimate the thermal conductivities of NaCl-MgCl_2 and KCl-MgCl_2 . Williams estimated the thermal conductivity of MgCl_2 based on its formula weight (he obtained 0.39 W/m-K), and took a mole fraction average of this value with the thermal conductivities of NaCl and KCl. The value of thermal conductivity obtained in this way for KCl-MgCl_2 (50-50) can be used as a conservative estimate for the thermal conductivity of NaCl-KCl-MgCl_2 (30-20-50) because there is a clear trend of increasing thermal conductivity with decreasing formula weight. The value of thermal conductivity obtained using this method is **0.39 W/m-K**, and is the one adopted by this study, mainly because it is consistent with the thermal conductivity values given for the other chloride salts.

Other methods to estimate the thermal conductivity of NaCl-KCl-MgCl_2 incorporate the data given in Polyakov and Gildebrandt [1974]. This is done by multiplying all the Polyakov data by a constant such that its KCl thermal conductivity values agree with those of reliable modern measurements. Doing this, one obtains a thermal conductivity for KCl-MgCl_2 (50-50) of about **0.25 W/m-K**, which may be again taken as a conservative value for the ternary. Alternately, one can use the scaled value for KCl-MgCl_2 (20-80) of 0.17 W/m-K, and average it with the known conductivities of NaCl and KCl to produce a value for the desired ternary composition. Doing this yields a thermal conductivity of around **0.28 W/m-K**.

Short of performing a measurement, there appears to be no reliable method to obtain thermal conductivities for salts containing MgCl_2 at this time. Williams' method relies on an estimate based on formula weight, while methods using the Polyakov data rely on older data and an untested scaling method. Similar concerns can be raised for the other properties: viscosity and density are based on a single 1960 reference, and the mole fraction average used to estimate heat capacity is similar to the Dulong-Petit prediction, which has an uncertainty of around 20% (Williams 2006a). Because of the central position of salt properties to the following analyses, present-day measurements to confirm these values would be an economical way to reduce uncertainty.

To quantify the significance of these property uncertainties, sensitivity studies were performed to determine the maximum power density achievable for different values of density, viscosity, thermal conductivity, and heat capacity. Each property was varied from 50% to 200% of the value assumed in this report, and the reference core design reanalyzed. Results are given in Figure 3.3-1.

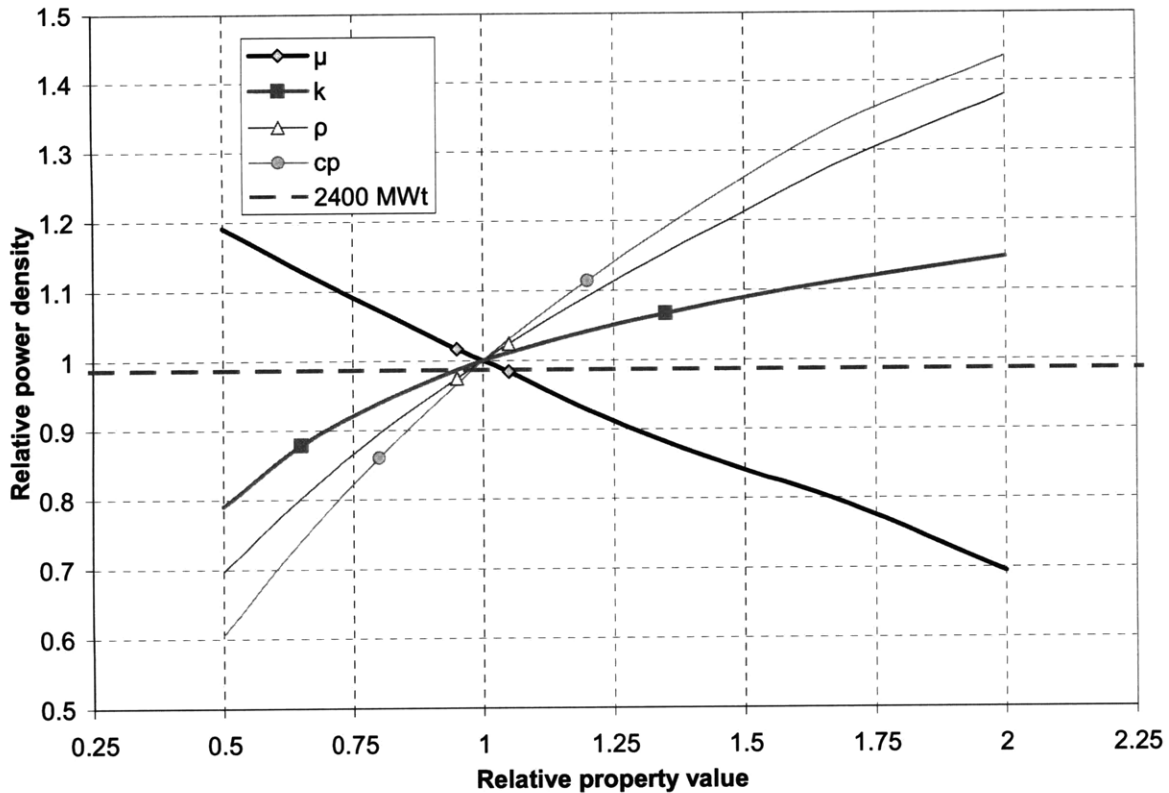


Figure 3.3-1 Power density vs. NaCl-KCl-MgCl₂ property values.

The dashed horizontal line denotes the power density that allows the target power rating of 2400 MWt to be achieved for the reference geometry. Using the assumed property values yields a power density above this line because the reference design has a maximum cladding temperature slightly below the 650°C limit, allowing some margin for the power to be increased beyond 2400 MWt. The markers on each line correspond to the likely uncertainties for each property value. Viscosity measurements from around 1960 give errors of 5% or lower, suggesting a similar uncertainty in the value used for the ternary chloride adopted. Density measurements from 1960 are similarly reliable, so the density uncertainty also should not be more than 5%. As mentioned, uncertainty in heat capacity may be as large as 20%, the uncertainty of the Dulong-Petit prediction. Finally, the conservative estimate for thermal conductivity (0.25 W/m-K), is about

35% lower than the assumed value (0.39 W/m-K), so an uncertainty of 35% is assigned to thermal conductivity.

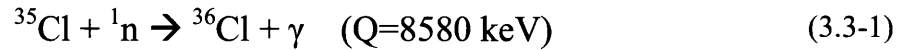
Figure 3.3-1 shows that low values of thermal conductivity or heat capacity would have the largest impact on maximum power density, and may make the target power level of 2400 MWt unachievable for the reference core design. The large uncertainties in these two properties are therefore the most in need of addressing. However, it should be noted that despite property uncertainties the original power density target of 100 kW/l can still be comfortably achieved.

Chemical & corrosion behavior

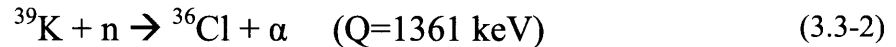
Chemical and corrosion characteristics are also important factors in evaluating the viability of a coolant. Chemically, liquid salts act as fluxing agents which prevent oxide film formation. The lack of a chemically passive film makes coolant chemistry control particularly important for liquid salt systems, and while this is easy to accomplish for fluoride salts it is somewhat more difficult for chlorides. (communications with Forsberg) Corrosion characteristics of the selected ternary chloride are presented in a 1960 BNL report (Susskind et al., Corrosion Studies for a Fused Salt-Liquid Metal Extraction Process for the Liquid Metal Fuel Reactor, BNL-585, 1960), which states that the chloride produces no serious corrosion in most of the steels tested, including a Cr-Mo steel that may be comparable to the T-91 steel used in this design. The general chemical compatibility of liquid salts with structural materials makes it reasonable to expect that no major corrosion issues will be encountered. Nevertheless, experimental tests simulating core conditions for the selected coolant and structural materials will ultimately be needed to fully assess corrosion and chemical behavior.

Neutron activation analysis

Salts containing chlorine produce the radioisotope Cl-36, which is a 0.709 MeV beta emitter with a 300,000 year half life, through the neutron absorption reaction:



Cl-35 has a natural abundance of 75.78%. Likewise, salts containing potassium also produce Cl-36 through the reaction:



K-39 has a natural abundance of 93.26%. Activation calculations were performed by first using MCNP to determine the flux-averaged cross sections for the above reactions in the three regions of the core. This value is multiplied by the average flux and the number of target nuclides in each region to obtain the rate of production of Cl-36 nuclides. The applicable data is presented in Table 3.3-2.

Each assembly has a coolant volume of $1.32\text{E-}02 \text{ m}^3$ in the radiation zone. Using the inlet coolant density of 1874 kg/m^3 , this corresponds to 351 moles of Cl-35 and 57.6 moles of K-39 per assembly. After 50 EFPY, the expected Cl-36 activity is: **2.1E+3 Ci** for the entire inventory, assuming no neutron flux outside the active core. This corresponds to **0.15 mCi** per kilogram of coolant salt, for a total coolant inventory of about $1.43\text{E+}6 \text{ kg}$. About 13% of this Cl-36 activity is due to potassium, with the rest due to chlorine.

Table 3.3-2 Neutron activation data

Core region	Cl-35 cross section (b)	K-39 cross section (b)	Average Flux (#/cm²s)	Number of assemblies
Outer – Fresh fuel	4.04E-03	3.96E-03	1.1E+15	234
Middle – Once loaded fuel	4.11E-03	3.61E-03	1.9E+15	156
Inner – Twice loaded fuel	4.14E-03	3.53E-03	2.1E+15	61

Cl-36 activation is a significant radwaste issue due to its long half life and chlorine's high mobility in water. While the amount of Cl-36 produced using this salt is not enough to immediately disqualify it, it is also non-negligible and the costs associated with handling Cl-36 need to be considered in the final design. Incidentally, this also holds true for any coolant salt containing potassium, because potassium contributes significantly to Cl-36 activation.

Nevertheless, disposal of radioactive Cl-36 is not expected to be a constraining challenge because low-level radioactive coolant salt can likely be cheaply disposed of by injection into a stable geologic salt formation. A small portion (1.90%) of Cl-36 will decay via electron capture into sulfur-36, which forms a corrosive chloride and would have to be removed as part of coolant chemical control.

In addition to long term activation due to Cl-36 production, use of the selected coolant salt will also result in significant short term activation from Na-24 ($T_{1/2} = 15$ h) and K-42 ($T_{1/2} = 12$ h). This short-term activation, similar to that in sodium fast reactors, complicates refueling as some time is needed after irradiation to allow activation products to decay.

4. Steady State Reactor Design

The purpose of this thesis is to develop a competitive design for a 2400 MWth reactor using liquid salt as coolant. Liquid salts are potentially attractive because of their optical transparency, high volumetric heat capacities, and general chemical compatibility. As described in the salt selection section, the ternary chloride eutectic NaCl-KCl-MgCl₂ (30%-20%-50%) was selected as the liquid salt most suitable for high power density fast reactor applications. The design considered is a dual-free-level pool-type reactor based on the earlier fast reactor designs [MacDonald 2002].

A successful design would be able to generate the rated power without violating any materials or pumping constraints, have a power cycle efficiency higher than or comparable to that of similar fast reactors, and fit within a similarly sized reactor vessel. Furthermore, it must be able to survive each limiting transient – unprotected station blackout, unprotected loss of flow, and transient overpower – without fuel element damage, relying only on the design's passive systems. The passive safety systems employed to address these transients are the same as those used in the lead flexible conversion ratio reactor: a reactor vessel auxiliary cooling system (RVACS), and a passive secondary auxiliary cooling system (PSACS).

Steady state design for the core was performed using a subchannel spreadsheet model described in Section 2.1. The intermediate heat exchanger model used is the same as that developed for the design of the lead-cooled FCR reactor. Results from these two models were incorporated into a RELAP5-3D model of the entire plant system in order to perform transient analyses. The salt reactor RELAP model required the implementation of virtual free levels due to a current

limitation in the RELAP code; the model and the virtual-free-level approximation are described in Section 2.3.

4.1 CR=1 reference core design

The core design selected uses wire-wrapped fuel pins (OD=0.752cm) in a triangular lattice (P/D=1.18836) arranged into hexagonal assemblies. This geometry was chosen because it is more suitable for providing the low coolant volume fraction needed to meet reactor physics requirements, and the specific value of P/D was chosen to correspond to a power density of 130 kW/l for the number of assemblies and pins in the core. As for the lead reactor system, the fuel pin active length is 1.3m, with a 1.3m gas plenum region above the core, and 30cm of reflector pins followed by 1.0m of shield pins below the core. Unlike with the lead reactor system, two rings of reflector assemblies and one ring of shield assemblies are added to the periphery of the core to improve neutron economy and protect long-life vessel structural materials. A summary of core geometry parameters is summarized in Table 4.1-1.

Table 4.1-1 Reference CR=1 salt core geometry

Total fuel pin length (m)	3.9
Fuel pin heated length (m)	1.3
Pin outer diameter (mm)	7.52
Pin cladding thickness (mm)	0.63
Pin pitch P(mm)	8.94
Pin P/D	1.18836
Wire diameter (mm)	1.42
Wire axial pitch H (m)	0.184
H/D	24.5
Number of pins along each edge of the assembly	12
Number of pins per assembly	397
Number of LEMs per assembly	25
Number of fuel pins per assembly	372
Assembly wall – fuel pin gap thickness (mm)	1.70
Assembly wall thickness (mm)	3.94
Assembly – assembly gap thickness (mm)	2.22
Assembly pitch (m)	0.191
Number of fuel assemblies in core	451

The steady state performance of this core, as calculated by the subchannel model, is given in Table 4.1-2. This data is based on several conservative assumptions present in the subchannel model, most notably the assumption that there is no intra-assembly mixing between different temperature subchannels, as well as use of an unmodified Gnielinski heat transfer correlation which is conservative for wire-wrap geometry. The coolant flow rate through the core assumes a three-zone orificing scheme: i.e. the core is divided into three zones based on peaking factors and each zone is orificed to have the smallest flow rate that does not cause the cladding temperature limit of 650°C to be exceeded. The margin of a couple degrees centigrade in the reference case was introduced when the minimum core pressure drop needed to meet this criteria was rounded up to the reference value of 700kPa.

The data in Table 4.1-2 for the reference core also includes two small non-conservative assumptions. First, the maximum assembly peaking factor, as given in Table 4.1-1, was taken as

the 1.26 rather than the BOL maximum of 1.30, based on earlier data for the CR=1 core. Second, the presence of control rods in some assemblies, which would displace some fuel rods and therefore raise the average power per pin, was neglected. Since these are both assembly-level effects, they can be addressed using orificing; an adjusted orificing scheme can distribute more coolant flow to the higher-peaked assemblies with a small increase in total pressure drop. Alternatively, the total coolant flow rate through the core can be increased a small amount (<5%) to counter the higher peaking. A study examining core flow rate (see the station blackout transient section) showed that even a 20% increase in coolant flow rate can be designed for without any performance penalties except a higher pressure drop. Since the reference design is already below the soft constraint on pressure drop, and pressure drop can be adjusted upward by using larger pumps, these non-conservative assumptions do not change the fundamental conclusions of this report.

Table 4.1-2 CR=1 NaCl-KCl-MgCl₂ salt reference core operating characteristics.

Total Power (MWt)	2400
Power density (W/cc)	130
Average power per pin (W)	1.43E4
Maximum assembly peaking factor	1.26
Maximum axial peaking factor	1.276
Coolant inlet temperature (°C)	496
Average coolant outlet temperature (°C)	569
Pressure drop across core (Pa)	7.00E5
Coolant mass flow rate through core (kg/s)	3.28E4
Pumping power through core (MWth)	12.3
Maximum guard vessel temperature (°C)	>442
Hot channel characteristics:	
Inlet coolant velocity (m/s)	4.4
Reynolds number	1.30E4
Nusselt number	92
Heat transfer coefficient (W/m ² K)	1.1E4
Maximum film ΔT (K)	71
Maximum cladding temperature (°C)	648
Maximum fuel temperature (°C)	<932
Total Power (MWt)	2400

One of the original design constraints could not be satisfied by the reference design: the steady state vessel temperature constraint of 430°C, given by the ASME code for the vessel material SS-316. The maximum guard vessel temperature modeled by RELAP for the salt reactor is 442°C, and this is along the side of the vessel where RVACS flow is highest. Directly underneath the vessel there would be less RVACS airflow, so vessel temperatures would be closer to the coolant inlet temperature of 496°C. Given the high melting point of liquid salt, lowering the coolant inlet temperature is not an option, so in order to reconcile the gap between the coolant inlet temperature and the vessel temperature limit, some additional measure would have to be employed, such as low power blowers cooling the vessel's outer surface . Alternatively, a larger insulated vessel with decay heat removal through a direct reactor auxiliary cooling system (DRACS) could be employed.

Core spacer options

The core pitch-to-diameter ratio of ~1.19 introduces the possibility of using honeycomb-shaped grid spacers instead of wire wrap spacers. A rough comparison study was performed evaluating the pressure drop and heat transfer characteristics of grid spacers; it was determined that wire-wrap and grid spacers are about equivalent when taking into account uncertainties. The reference design uses wire wrap, despite uncertainties regarding wire-wrap heat transfer, because there is more experience and literature for wire wrap at a P/D of 1.19. Nevertheless, there may be cause to use spacers depending on the configuration of LEMs chosen. Using LEMs with a reservoir diameter equal to fuel pin diameter allows wire wrap to be used along the entire pin length. Larger LEM reservoirs would reduce the number of LEMs needed (from 25 per assembly in the reference case) but would be incompatible with wire-wrap because wires would

not fit between the reservoirs and the pins adjacent to them. Using larger LEM reservoirs would require either use of grid spacers or a combination of wire-wrap in the fuel region and grids in the reservoir/plenum region.

Radiative heat transfer

Because liquid salts are transparent to infrared and optical radiation, it is important to consider if radiation contributes significantly to heat transfer in liquid salt systems. For the reference design, the average heat flux in the reference core is $4.7 \cdot 10^5 \text{ W/m}^2$. In comparison, the radiative heat flux of clad at 650°C is given by the Stefan-Boltzmann law:

$$j = \epsilon \sigma T^4 = 0.75 * 5.67 * 10^{-8} \text{ Wm}^{-2} \text{ K}^{-4} * (923\text{K})^4 = 3.1 * 10^4 \text{ W/m}^2 \quad (4.1-1)$$

Here σ is the Stefan-Boltzmann constant, and ϵ is the emissivity. (generously approximated as 0.75 for stainless steel. This value is less than 10% of the average heat flux in the core.

Considering 650°C is higher than any temperature reached on the cladding outer surface, as well as the small view factor of a pin in a pin bundle, the actual heat transfer due to radiation would be smaller than this value. Therefore, it is reasonable to neglect radiative heat transfer for the liquid salt core at steady state, as long as significantly higher cladding temperatures are not achieved.

The possibility of taking advantage of radiative heat transfer during transient scenarios has also been considered. During a transient, coolant outlet temperatures can reach over 900K, and the gas plenums and structures above the core would reach the same temperature. The top of the core is composed of many small openings (coolant channels) and would effectively have a high

emissivity, since radiation entering these openings will mostly be absorbed. Alternatively, the top of the core can be specifically engineered to have a high emissivity, such as through the use of high emissivity coatings. Generously assuming an emissivity of unity can be achieved, the top of the core can be used to reject up to 37.2 kW/m^2 , corresponding to 0.53 MW for the 14.3 m^2 area core. This amount of heat is a small fraction of the amount that can be removed via the RVACS and PSACS passive cooling systems, so there is no strong incentive to develop systems that can reject heat emitted via radiation to an ultimate heat sink. Furthermore, the view factor between the top of the core and the top of the vessel is on the order of only 4%, due to the tall chimney separating them, making radiative heat transfer even less appealing as an avenue for decay heat removal.

4.2 Heat exchanger design

Tube-in-shell intermediate heat exchangers with salt on the shell side and CO_2 on the tube side, similar to those used in the lead-cooled FCR reactor, were designed for the liquid-salt cooled reactor. Ribbed tubes were employed to enhance heat transfer on the CO_2 side, and grid spacers were used to maintain bundle geometry. One alternative to tube-in-shell heat exchangers was first considered: printed circuit heat exchangers, or PCHEs.

The use of liquid salt as coolant may enable the use of PCHEs as IHXs, since liquid salt doesn't carry the same oxide formation issues as lead coolant. PCHEs use a very large number of tiny channels, which are vulnerable to corrosion and oxide formation but allow for very high power densities and smaller pressure losses. Initial estimates of PCHE geometry and performance showed they could fit in the vessel while allowing smaller pressure losses than tube-in-shell heat

exchangers on both the primary and secondary sides. However, these reduced pressure drops did not result in a substantive enough performance increase to justify the greater uncertainties associated with designing PCHEs. Pool-type reactor designs may also not be ideally suited for PCHEs because it is awkward to fit rectangular horizontal PCHEs into the annular vertical space of the downcomer. Because the higher power density salt core allows sufficient space in the vessel for reasonably designed tube-in-shell IHXs, tube-in-shell IHXs were chosen for use in the reference design.

Intermediate heat exchangers were designed for the liquid-salt cooled reactor using the spreadsheet analysis tools developed for the lead-cooled reactor, using the Gnielinski heat transfer correlation on the salt side and substituting the appropriate salt properties and flow conditions. Primary side inlet conditions and coolant flow rates follow from the core design, while secondary side inlet conditions were kept the same as those for the lead reactor so the same power conversion system could be used for the salt reactor. With both hot-side and cold-side conditions specified, designing the IHXs involved determining what heat exchanger geometry would transfer the correct amount of power while fitting in the downcomer annulus and minimizing pressure losses.

Four kidney shaped IHXs were used to maximize use of space in the downcomer. The thickness of the heat exchanger tubes and plenums were chosen so that material stresses would not exceed the limits set by the updated ASME code for T91 steel at the operating temperatures (the hot salt temperature ($\sim 569^{\circ}\text{C}$) for the tubes and the cold salt temperature ($\sim 496^{\circ}\text{C}$) for the plenums) and lifetime (30 years) assumed.

Since both of the free levels are at the same atmospheric pressure, any pressure loss due to flow between the free levels (primarily due to the IHX) will result in a separation in the free levels, H , such that pressure rise due to gravity (ρgH) is equal to this pressure loss. Because of this, there is a maximum allowed pressure loss through the IHX that is determined by the maximum allowed separation distance between the two free levels in the vessel, i.e., the maximum value of H . This separation distance is conservatively taken as the length of the IHX itself. To better illustrate this, a to-scale diagram of the vessel is given in Figure 4.2-1. The lower “cold” free level should not be below the bottom of the IHX, since this can result in sub-atmospheric pressures beneath the IHX and lead to voiding. The upper “hot” free level must be above the top of the IHX. If it is conservatively assumed that vessel height is minimized, i.e. there is only a small clearance between the top of the vessel and the top of the IHXs, then the hot free level can be assumed to be near the top of the IHX. In this case, the maximum level separation distance H is the height of the IHX, since the cold free level cannot be below the bottom of the IHX.

This maximum level-separation distance becomes an important constraint for the salt reactor because the lower density of salt compared to lead permits a much smaller IHX pressure drop. In order to keep the primary-side pressure drop below this constraint, while maintaining a reasonable heat exchanger length and secondary-side pressure loss, it was necessary to make more room in the downcomer by using a bottlenecked chimney above the core. The bottlenecked chimney is also illustrated in Figure 4.2-1. The bottlenecked chimney is large enough to fit the entire core at its bottom but gets smaller above the core to only fit the fuel assembly control rods; this is possible because the reflector and shield assemblies surrounding

the fuel do not have control rods extending upward from them. Bottlenecking the core results in 21% more space in the surrounding annulus, which allows a dramatic 70% increase in the number of heat exchanger tubes. This much larger increase in “usable space” is due to the fact that there is a 10 cm clearance between the IHXs and the vessel walls and a nearly 15cm thick gas plenum which cannot be occupied by tubes; this area without tubes occupies a much larger fraction of the annular space in the non-bottlenecked design.

For each value of IHX tube diameter, a minimum tube P/D exists below which the salt pressure drop exceeds the constraint outlined above. Minimizing tube P/D is desirable because it maximizes the heat exchanger power density and CO₂ flow area. Selecting the diameter of the IHX tubes involves a tradeoff: smaller tubes increase power density and reduce heat exchanger length, while larger tubes reduce the secondary side pressure drop. Larger tubes were chosen because the secondary side pressure drop is important to power conversion system performance, and because fewer large tubes would be easier to produce and maintain than many small tubes. A tube diameter of 13 mm was chosen, corresponding to a P/D of 1.23 and an IHX tube length of 6.78m, which fills most of the space available for IHXs while allowing room for the CO₂ plenums. IHX geometry and performance characteristics calculated using the spreadsheet model are given in Table 4.2-1. Tube ribbing and grid spacer design are the same as for the lead reactor IHXs. A to-scale illustration of the IHX geometry in the salt reactor is given in Figure 4.2 -2.

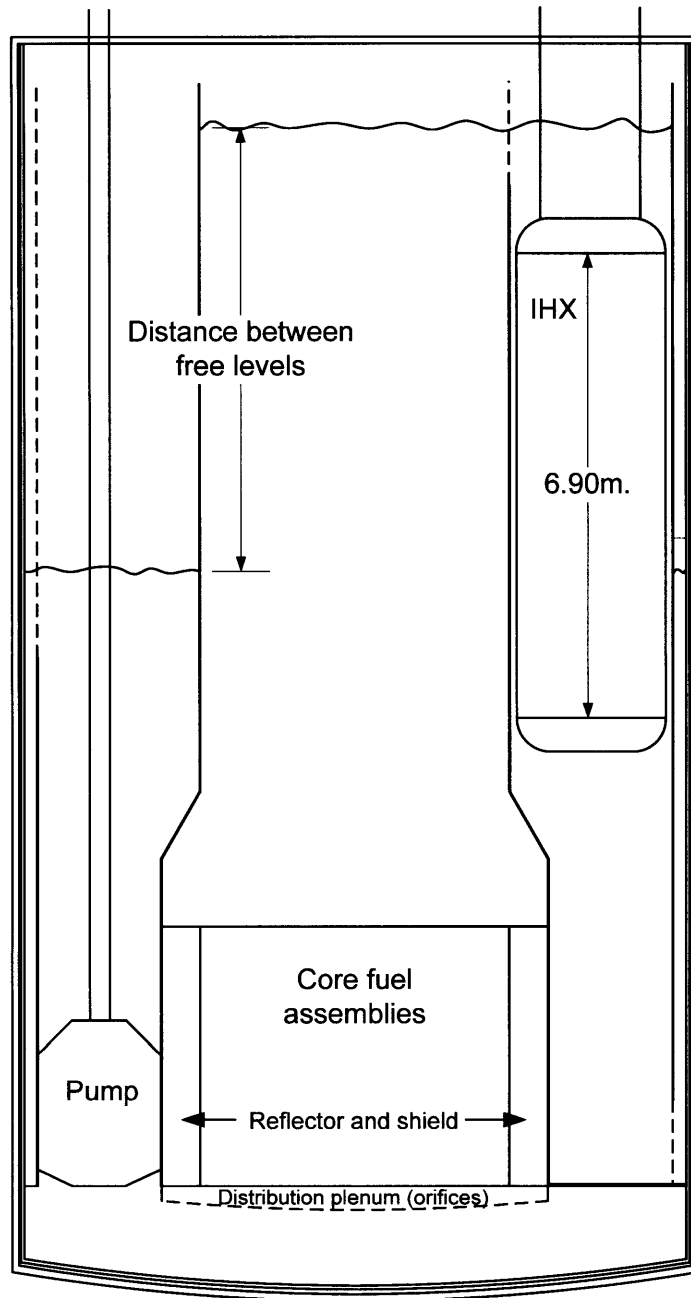


Figure 4.2-1 To-scale illustration of vessel layout

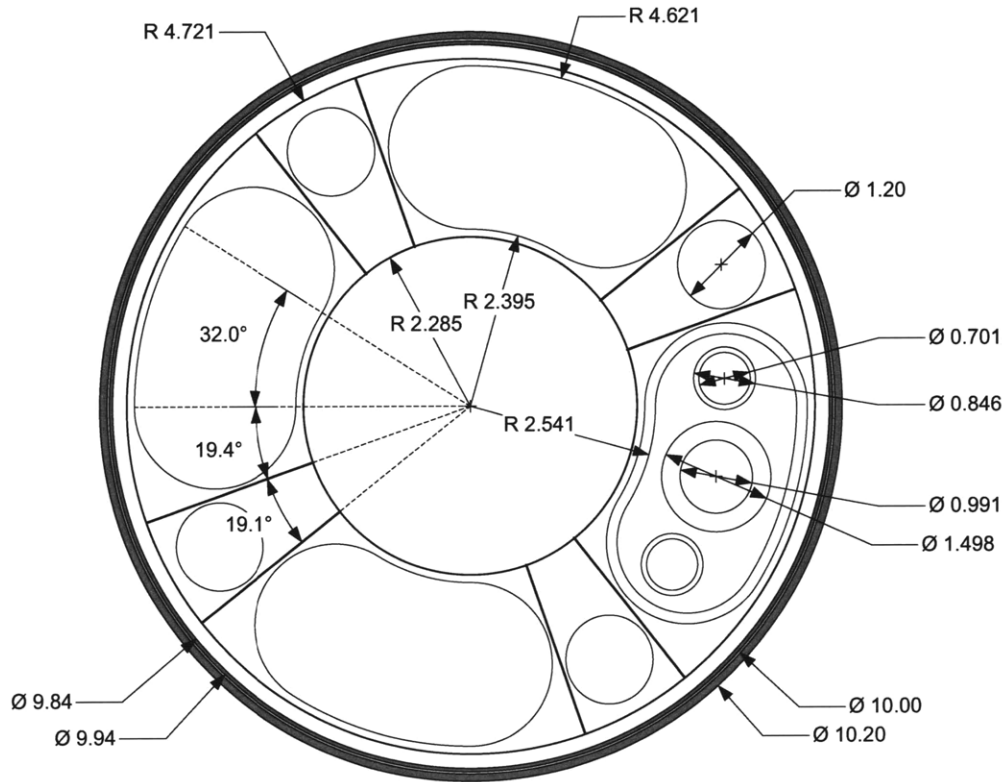


Figure 4.2-2 To-scale illustration of IHX layout

Table 4.2-1 Salt reactor IHX geometry and performance (for 1 out of 4 IHXs)

Tube outer diameter (mm)	13.0
Number of tubes	21989
P/D	1.23
Tube thickness (mm)	2.02
Tube length (m)	6.8
IHX cross-sectional area (m ²)	6.6
Power transferred (MW)	600.
Salt flow rate (kg/s)	8200.
Salt inlet temperature (°C)	568.9
Salt outlet temperature (°C)	496.0
CO ₂ flow rate(kg/s)	3212.
CO ₂ inlet temperature (°C)	396.4
CO ₂ outlet temperature (°C)	548.4
Salt flow area (m ²)	1.95
Salt side pressure loss (kPa)	116.
CO ₂ flow area (m ²)	1.38
CO ₂ side pressure loss (kPa)	292.

Figure 4.2-2 and Table 4.2-1 show the salt IHXs are somewhat larger (6.6m^2 vs. 6.0m^2 cross sectional area) and taller (6.8m vs. 5.7m tube length) than those for the lead reactor [Todreas & Hejzlar, 2008b], which is not unexpected given the poorer heat transfer characteristics of liquid salt. This poor heat transfer is evident in the distribution of thermal resistance. For the lead reactor, the thermal resistance due to convection between the primary coolant and the heat exchanger tubes constitutes 19% of the total thermal resistance, while for the salt reactor it constitutes 59%. Nevertheless, the pressure losses for the primary and secondary sides are both acceptable. The salt pressure losses do not exceed the maximum gravitational head, and the CO_2 side pressure losses are not different enough from those of the lead reactor to require significant reworking of the secondary system.

4.3 LEM design

Reactor physics issues in preliminary designs for the liquid-salt FCR reactor significantly limited thermal hydraulic performance. The poorer thermal hydraulic performance of liquid salts drives designs towards a looser lattice, but the high coolant temperature coefficient of liquid salts necessitated a tight lattice. Other measures investigated for reducing the coolant temperature coefficient – axial blankets, streaming assemblies, and zirconium hydride control rods – also reduced the achievable power density by increasing the effective hot-spot peaking factor. Taken together, these factors reduced the maximum power density for the salt reactor to below 70 kW/l, even for a high core pressure drop of over 1.0 MPa. This power density was significantly below the target value of 100 kW/l and the power densities of other liquid cooled reactors.

Replacing the aforementioned physics measures with lithium expansion modules (LEMs) alleviates the thermal hydraulic difficulties associated with them. LEMs consist of a reservoir filled with molten lithium (enriched to 90+% Li-6) situated in the gas plenum region above the active core, connected to a capillary that extends into the core. A schematic view of a LEM is shown in Figure 4.3-1. When the coolant outlet temperature increases, thermal expansion of lithium in the reservoir forces lithium into the capillary, which reduces the reactivity of the core because lithium-6 is a fast neutron absorber. LEMs can therefore be used to passively reduce the coolant temperature coefficient of the core, thus removing the reactor physics constraint on core P/D. Use of LEMs allows a large increase in P/D (to ~1.19), increasing the coolant volume fraction by over 50%. The small number of LEMs needed (25 per 397 pin assembly in the CR=1 reactor) has a much smaller impact on the hot-spot peaking factor than axial blankets, streaming assemblies, and hydride control rods. The impact on thermal hydraulics is huge: the LEM reference design has a higher power density (130 vs. 68 kW/l) and a lower core pressure drop (0.7 vs. 1.07 MPa) than the best previous design not using LEMs while maintaining the maximum cladding temperature below the 650C limit.

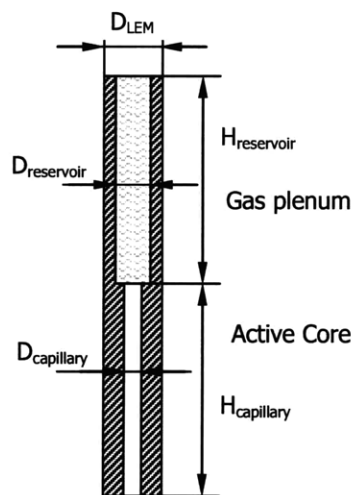


Figure 4.3-1 Schematic view of a lithium expansion module

Neutronic studies of LEM performance conducted as part of this project show that LEMs can be tailored to produce a wide range of different reactivity responses. Important LEM parameters are its operating temperature range and its total reactivity worth. The operating temperature range is the range of temperatures between when the LEM capillary is completely empty and completely full, and depends on the LEM's reservoir and capillary geometry as well as the amount of lithium present in the LEM. The total reactivity worth of an LEM is the difference in reactivity between when the capillary is full and when it is empty, and depends on the volume of the capillary. The reactivity response of LEMs is approximately linear with the number of LEMs; doubling the amount of LEMs (or their size) doubles the reactivity response. Increasing the size of an LEM reservoir reduces the temperature range of the LEM, since a smaller temperature change is needed to produce the same increase in lithium volume. Increasing the diameter of an LEM capillary increases the LEM's temperature range and total reactivity worth proportionally.

Within an LEM's operating temperature range, the reactivity response is approximately cosine shaped if the LEM capillary has a fixed diameter (Figure 4.3-2). Shrinking or bottlenecking parts of the LEM capillary can reduce the reactivity worth and temperature range of specific portions of the response curve, allowing its shape to be carefully tailored. Outside of the LEM's operating temperature range, the LEM is saturated, since an additional increase or decrease in temperature has a minimal effect on reactivity. LEM saturation is undesirable because without the reactivity contribution from LEMs, the high coolant temperature coefficient of liquid salt can lead to positive feedback. Therefore, LEMs need to be designed so their operating range encompasses the full range of possible coolant outlet temperatures.

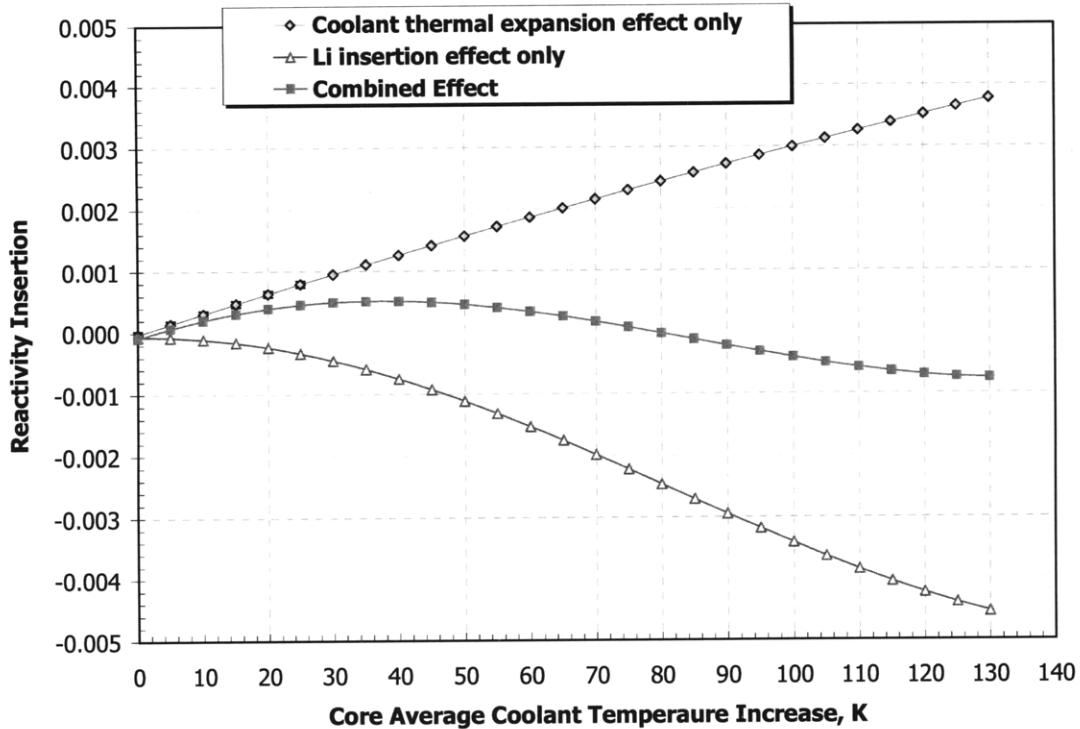


Figure 4.3-2. Example of LEM reactivity insertion curve (25 LEMs/assembly)

An important assumption was used during LEM design: the LEMs were treated as a lumped entity, with their response based on the coolant conditions at the outlet of the “average” channel in the core. In an actual core, different areas of the core will have somewhat different outlet temperatures, meaning not all LEMs will respond identically. This assumption was also used to simplify LEM modeling in both RELAP and MCNP. In principle a fully 3-D analysis could be performed that tracks the coolant outlet temperature in each assembly and the resulting LEM reactivity insertion. Furthermore, different LEMs could be specifically designed for each radial position in the core to provide a desired power shape.

To ensure passive safety, the reactivity response of the LEMs in the salt core was designed so the total coolant temperature coefficient would be zero or negative over the range of possible LEM

temperatures. This LEM response for the CR=1 core is shown in Figure 4.3-3, along with the coolant temperature response. The two reactivity responses do not add directly in practice because the LEM response depends on the coolant outlet temperature while the coolant temperature response depends on the power-squared weighted coolant average temperature. However, it is conservative to assume that a change in coolant outlet temperature is equal to the change in average temperature because the former is usually larger during the early stages of a transient, which would increase the reactivity effect of the LEMs. (This assumption is only used for design, not modeling, since LEMs are modeled explicitly in RELAP.) One can see that the “total” reactivity response in Figure 4.3-3 has a negative slope between the steady state temperature and 140K over the steady state temperature. This temperature range was selected based on thermal hydraulic analyses that showed the core outlet temperature could rise by as much as 120K during a transient; the 140K value was used to provide a margin beyond this value. Having the slope of the total reactivity curve equal zero at steady state requires that the LEMs be partially inserted at steady state, resulting in a reactivity penalty of about 25 cents. However, this penalty can be reduced by bottlenecking the top of the LEM capillary so less lithium is present in the core at steady state.

The LEM reactivity curves designed for the reference salt reactor are shown in Section 2.4. Reactor physics calculations showed that these desired LEM curves could be implemented using 25 LEMs per assembly for the CR=1 reactor and 12 LEMs per assembly for the CR=0 reactor. The CR=0 core is able to use fewer LEMs because each LEM has a greater reactivity worth in the fertile-free core, since fewer neutrons are lost to absorption, and because the CR=0 core has a smaller coolant temperature coefficient due to higher leakage. More LEMs (or larger LEMs)

could be added if a stronger reactivity response is desired, although doing so would displace additional fuel rods and lower power density somewhat.

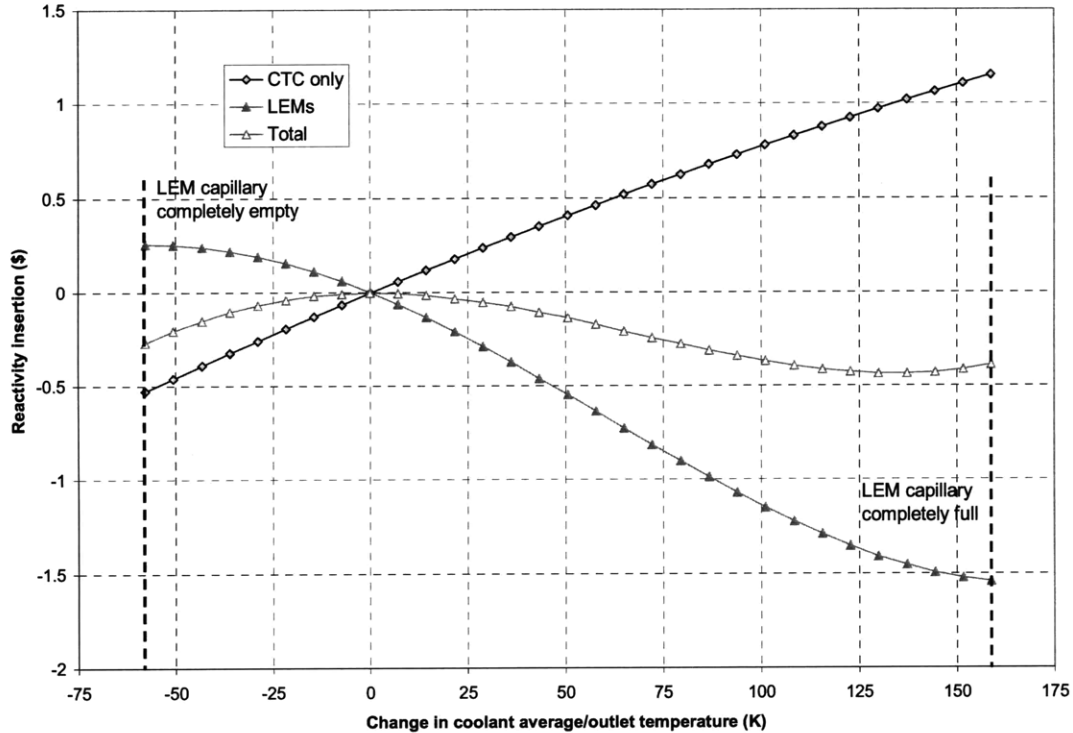


Figure 4.3-3 CR=1 LEM and CTC reactivity responses

4.4 CR=0 design

The steady state thermal hydraulic model for the CR=0 reactor is nearly identical to that of the CR=1 reactor. The primary difference is with assembly peaking factors calculated by MCNP; the CR=1 core has a maximum peaking factor of 1.26 while the CR=0 core's is 1.35. In reality, control rods can be adjusted to create a flatter radial power profile, but conservative un-rodded values are adopted to be consistent with prior analyses. The CR=0 core also has a slightly different axial power shape than the CR=1 core. Finally, the CR=0 core has 19 control rods and 12 LEMs in every assembly, compared to 25 LEMs per assembly in the CR=1 core and control

rods in only some assemblies, which displaces additional fuel pins and therefore raises the effective peaking somewhat.

The higher radial peaking in the CR=0 core means that the hot channel coolant velocity needs to be increased to keep the peak cladding temperature below the 650°C steady state limit.

Calculations using the subchannel spreadsheet model showed that a 10% coolant velocity increase is needed, corresponding to a core pressure drop increase from 700 kPa to 825 kPa. It was determined that a three-zone orificing scheme could be used to maintain the same coolant flow rate between the CR=0 and CR=1 cores despite the difference in pressure drop. The higher core pressure drop translates into a larger pumping power, which raises coolant temperatures very slightly (<1°C). A summary of the CR=0 core operating characteristics is given in Table 4.3.2-1.

Table 4.4-1 CR=0 NaCl-KCl-MgCl₂ salt reference core operating characteristics.

Total Power (MWt)	2400
Power density (W/cc)	130
Average power per pin (W)	1.45E4
Maximum assembly peaking factor	1.35
Maximum axial peaking factor	1.277
Coolant inlet temperature (°C)	496
Average coolant outlet temperature (°C)	569
Pressure drop across core (Pa)	8.25E5
Coolant mass flow rate through core (kg/s)	3.28E4
Pumping power through core (MWth)	14.4
Hot channel characteristics:	
Inlet coolant velocity (m/s)	4.8
Reynolds number	1.42E4
Nusselt number	100.
Heat transfer coefficient (W/m ² K)	1.2E4
Maximum film ΔT (K)	70
Maximum cladding temperature (°C)	648
Maximum fuel temperature (°C)	<958

Because the primary coolant flow rate and temperatures are the same for the CR=1 and CR=0 cores, the same IHX design and power conversion system can be used for both reactors. This not only satisfies one of the primary goals of the flexible conversion ratio reactor project, but also significantly simplifies modeling for the CR=0 core.

Steady state fuel performance analysis

Fuel temperatures were calculated to determine if there is likelihood for fuel failure in the CR=0 liquid salt-cooled core. This is of particular concern because of the high linear heat rates in the reference core and the low thermal conductivities of fertile-free fuel. Fuel thermal conductivity is a function of many factors, including temperature, composition, burnup, migration of fuel constituents and infiltration of bonding material. Furthermore, there is a lack of data concerning high-zirconium CR=0 fuels. A conservative value for fuel thermal conductivity was obtained by taking the recently measured value for unirradiated fuel U-29Pu-4Am-2Np-30Zr at 500°C (12 W/m-K) [Meyer, 2007] and reducing it by 50% to take into account deterioration from irradiation. The value at 500°C is used because this temperature is close to the coolant inlet temperature; since fuel thermal conductivity increases with temperature, the value obtained sets a lower limit on thermal conductivity for un-irradiated fuel. For fuel performance under irradiation, a paper by Lee et. al [2004] states that a maximum degradation of thermal conductivity of about 50% occurs during irradiation. Degradation past this value does not occur because of bonding material ingress into the fuel at higher burnups. The fuel thermal conductivity for CR=0 core is therefore assumed to be 50% of 12 W/m-K, or **6.0 W/m-K**. For this calculation, pre-irradiation dimensions are used: the fuel pellet diameter is 5.42 mm, and the gap thickness is 0.42 mm. The lead alloy bonding material is assumed to have a thermal conductivity of 8.0 W/m-K (a higher conductivity sodium bond could also be used). Assuming

uniform power in the pin, the thermal resistance between the fuel centerline and the cladding inner wall is therefore:

$$R_T = \frac{\Delta T}{q'} = \frac{1}{4\pi k_f} + \frac{\ln\left(\frac{R_o}{R_i}\right)}{2\pi k_g} = \frac{1}{4\pi * 6.0 W / mK} + \frac{\ln\left(\frac{3.13mm}{2.71mm}\right)}{2\pi * 8.0 W / mK} = 0.016 K/Wm^{-1} \quad (4.4-1)$$

Here k_f is the fuel thermal conductivity, k_g is the gap bonding material thermal conductivity, R_o and R_i the inner and outer radii of the gap. The maximum linear heat rate q' in the CR=0 reference design is 20 kW/m; multiplying by the thermal resistance yields a ΔT between the fuel centerline and cladding inner wall of **320°C**. Since the maximum cladding temperature of 648°C allows a 552°C ΔT to fuel failure at 1200°C, there is a large margin to fuel failure even under conservative assumptions.

The 6.0 W/mK value for thermal conductivity is conservative for determining steady state fuel performance, but is not conservative for reactor transient behavior. A low value for fuel thermal conductivity magnifies fuel temperature reactivity feedbacks, which are generally negative. Therefore for transient studies, unirradiated values for metal fuel thermal conductivity were used, since they are larger and therefore yield conservative reactor physics parameters. This approach is appropriate because for most transients, cladding temperature is more limiting than fuel temperature.

5. Transient Performance

Four transients were selected as a basis for evaluating the safety characteristics of the salt-cooled FCR reactor. These are: an unprotected station blackout (SBO), a loss of flow accident (LOFA), an unprotected transient overpower (UTOP), as well as a generic protected transient.

Descriptions of each transient and how they were modeled are given in the corresponding subsections. The first three transients were selected because they constitute limiting “worst case” scenarios; successful mitigation of these transients demonstrates that the reactor is safe in virtually all realistic scenarios. The protected transient scenario was selected not due to its severity, but because it is much more likely to occur than the limiting transients considered. It is considered in order to demonstrate that protected transients can be mitigated using only natural circulation and passive decay heat removal without fuel failure or coolant freezing.

Subsequently, results from the protected transient analysis can be applied to any transient in which a scram occurs. For each of the above transients, mitigation is considered successful if both fuel element failure and coolant freezing can be avoided for seventy two hours, in correspondence to safety standards being adopted by the next generation of nuclear power plants [EPRI 1992].

5.1 CR=1 unprotected station blackout

The unprotected station blackout (SBO) accident analyzed for the salt reactor assumes that at time 0s, the reactor coolant pumps and pre-cooler pumps lose power, the generators become isolated due to loss of load, and the core fails to scram. Loss of pre-cooler pump power means that heat cannot be removed via the secondary system to the ultimate heat sink. Also, loss of

generator load puts the turbines at risk of damage due to overspeed, so the turbines need to be isolated following an SBO. Failure to scram means that the reactor must either shut down or reach a safe steady state through inherent reactivity feedbacks. Finally, core decay heat needs to be removed to avoid damage to the fuel cladding or other core structural materials. Decay heat removal is accomplished through two passive systems: the reactor vessel auxiliary cooling system (RVACS), and the passive secondary auxiliary cooling system (PSACS), systems originally developed for the lead-cooled FCR reactor. The RVACS functions via natural circulation of air past the exterior of the reactor vessel. The PSACS functions by passing secondary side CO₂ flow through a heat exchanger immersed in a tank of water; heat is removed via heating and boiling of the water.

The SBO accident is initiated in the RELAP model by tripping the reactor cooling pumps at time zero, closing the power conversion system isolation valves (valve 302 and 326 in the model), and opening the PSACS valves (323 and 324). Valve actuation occurs within the first half second of the accident sequence. These valves are ordinarily held open/shut in the actual system via powered solenoids or instrument air, so loss of power would cause them to automatically fail into the correct position. To be conservative, only two PSACS trains are opened to account for one train in maintenance and one train failing. Therefore, all results below assume that the PSACS system is operating at half of maximum capacity. Because the secondary system is not involved in the accident sequence once it has initiated, it is taken out of the RELAP model and replaced with time-dependant volumes as boundary conditions in order to reduce computational time; this simplification has no effect on transient behavior.

Reactor decay power for the salt CR=1 core was calculated using the code BGCore [Fridman, 2008] and implemented into RELAP, while reactor fission power is calculated using the point kinetics model built into RELAP using the reactivity data given in Section 2.4. The reactivity feedbacks implemented are: coolant temperature, fuel temperature, core radial expansion, and LEM feedback. The first two are calculated based on power-squared weighting of the coolant and fuel temperatures, the third is based on the average coolant temperature in the core, while LEM feedback is based on the temperatures calculated for explicitly modeled LEM reservoirs above the core.

Short term SBO response

The core peak cladding, core inlet, and core outlet temperature response to a station blackout for the first 1000 seconds is shown in Figure 5.1-1, for the reference salt reactor. Figure 5.1-1 shows that the salt reactor's peak cladding temperature exceeds its limit of 725°C less than three minutes after an SBO begins, reaching a maximum close to 750°C. The PCT data also show unusual double peaked behavior between 50 and 200 seconds. The reason for this unusual behavior is a transition from turbulent to laminar flow. The presence of this transition can be seen by plotting the coolant heat transfer coefficient in the core during the transient; this is done in Figure 5.1-2.

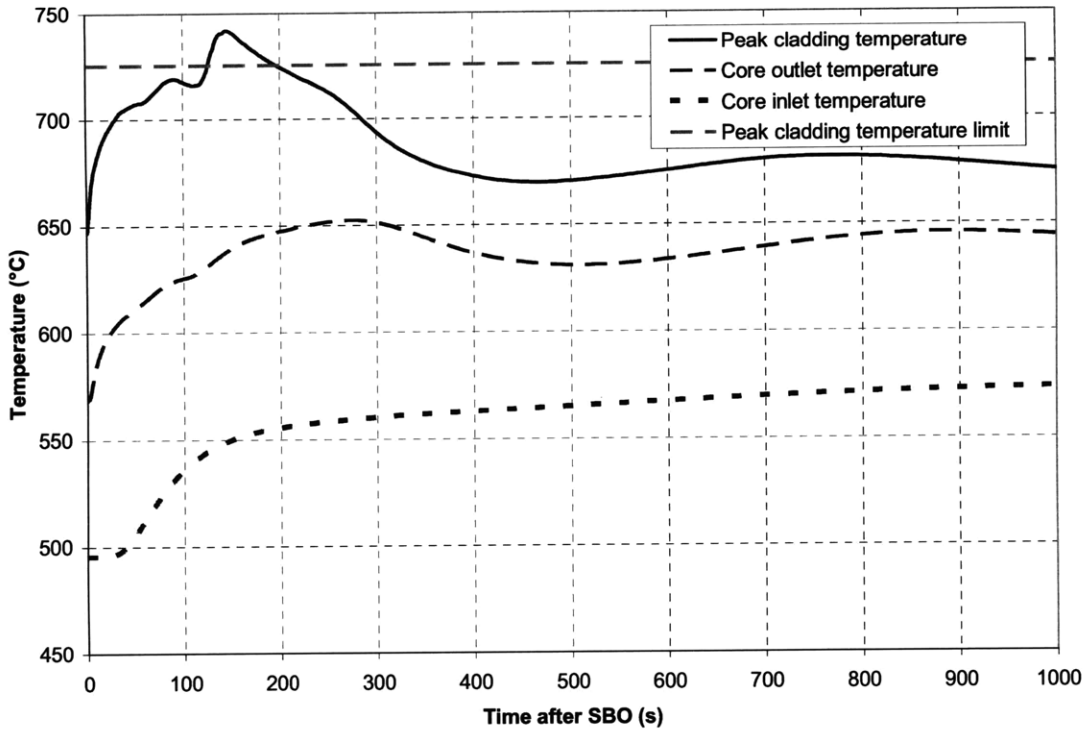


Figure 5.1-1 Short-term CR=1 salt reactor response to an SBO

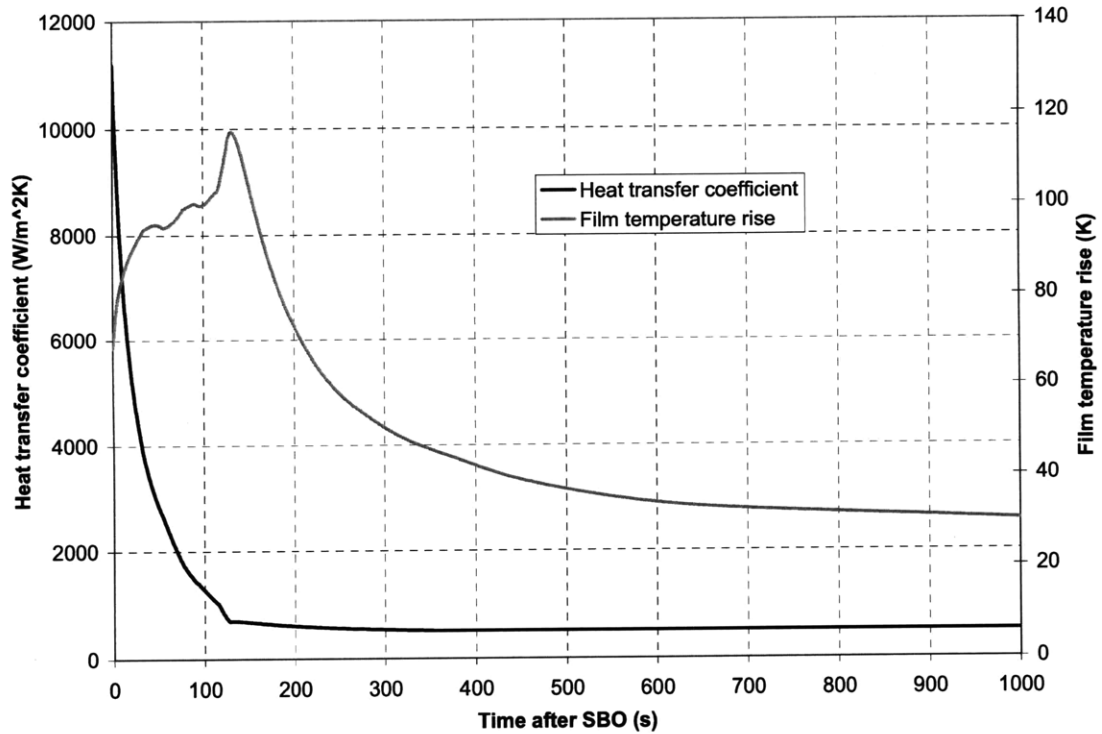


Figure 5.1-2 Core midplane heat transfer coefficient and film temperature rise

Figure 5.1-2 shows how RELAP models the heat transfer coefficient as coolant flow transitions from turbulent to laminar (the Gnielinski correlation is used for turbulent flow with $Re > 3000$). The heat transfer coefficient does not decrease smoothly, there is a slight knee at about 110 seconds, and a sharp discontinuity in slope at approximately 130 seconds. Meanwhile, heat flux decreases smoothly, so the film temperature rise, which is the ratio of heat flux to heat transfer coefficient, exhibits the strange peaked behavior shown. This behavior is in turn responsible for the shape of the peak cladding temperature curve.

The fact that the shape of the peak cladding temperature curve during an SBO is an artifact of the correlations adopted highlights one of the challenges of salt reactor transient modeling. The high viscosity and low density of salt cause it to operate at much lower Reynolds numbers; during loss of flow transients these Reynolds numbers become sufficiently low to result in transition and laminar flow. Accurately characterizing a salt reactor therefore requires a better understanding of wire-wrap heat transfer not only for turbulent flow, but for transition and laminar flow as well. For RELAP specifically, the pressure drop across the core is also inaccurately modeled during loss of flow, since RELAP uses the Colebrook-White correlation for tubes modified (via the surface roughness factor) to match the more accurate Cheng-Todreas wire-wrap correlation at steady state. The modeling artifacts due to the correlations used also occur at the IHXs and the reactor vessel wall, where there is also heat transfer from the salt; the effect of this on RVACS heat transfer is shown in Figure 5.1-3. Again around 100 seconds there is non-smooth behavior attributable to modeling flow regime transitions.

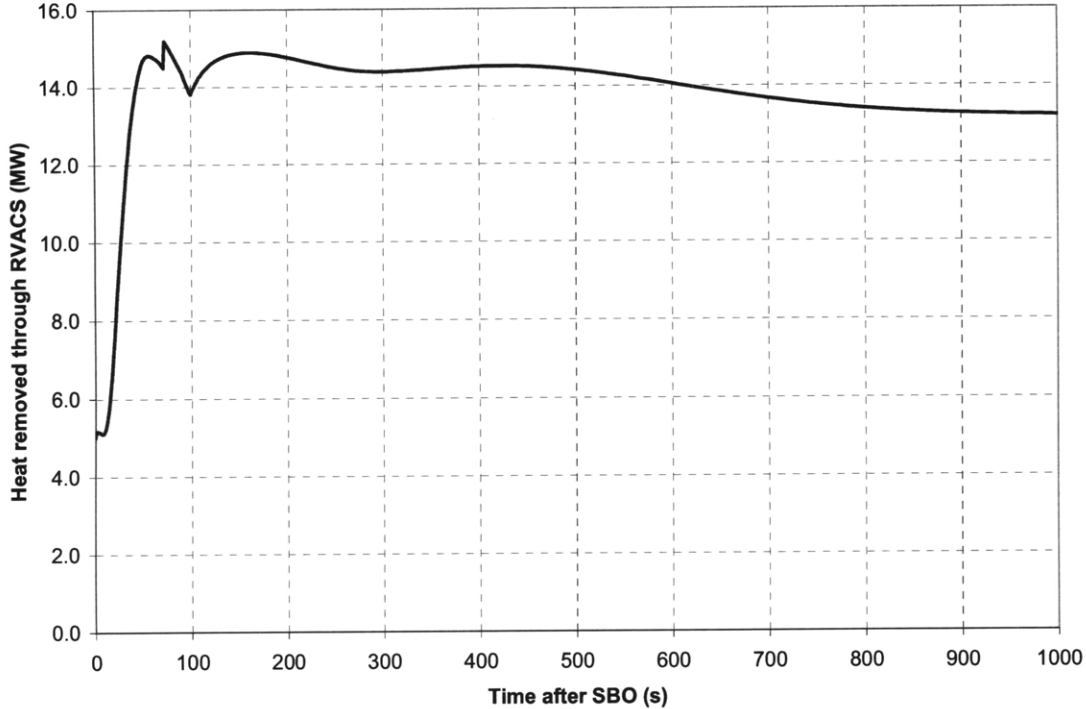


Figure 5.1-3 Heat removal through the RVACS after SBO

Despite the modeling challenges present with flow regime transitions, the results obtained can nevertheless be considered conservative estimates of actual transient behavior. With this being the case, it is apparent from Figure 5.1-1 that the unmodified salt reactor design exceeds the transient peak cladding temperature limit during an SBO. The primary reason is the poor heat transfer characteristics of salt leading to a high film temperature rise; while coolant temperatures are actually lower than those for the lead-cooled reactor, the difference between the peak cladding temperature and the coolant temperatures are much higher for the salt core. This situation is exacerbated during a loss of flow situation; the rapid drop off in the heat transfer coefficient leads to a ~70% increase in the film temperature rise (Figure 5.1-2).

Several strategies were tested to reduce the peak cladding temperature during an SBO transient. First, the amount of heat removed by the PSACS was adjusted; results are shown in Figure 5.1-4. The percentages shown in the legend roughly correspond to the amount of the heat each PSACS would remove for a given steady state in the primary system, as compared to an older reference design. In reality the heat removal capacity of the PSACS is determined by the design of the passive auxiliary heat exchanger (PAHX) in the PSACS water tank. In RELAP the different PSACS capacities are modeled by changing the PAHX heat structures as well as by varying the number of trains from two to one; this latter approach is necessary because of computational slowdowns for low values of heat removal in a single train. The 200% PSACS design corresponds to the one used in the reference lead-cooled FCR reactor design, correspondingly the 100% power PSACS operates at half the power of this original lead system. Figure 5.1-4 shows that changing the PSACS design does not have a large effect on short term performance, and essentially no effect on the initial peak that exceeds the peak cladding temperature limit. This is not surprising because the primary issue during the early stages of the transient is film temperature rise rather than primary coolant temperature.

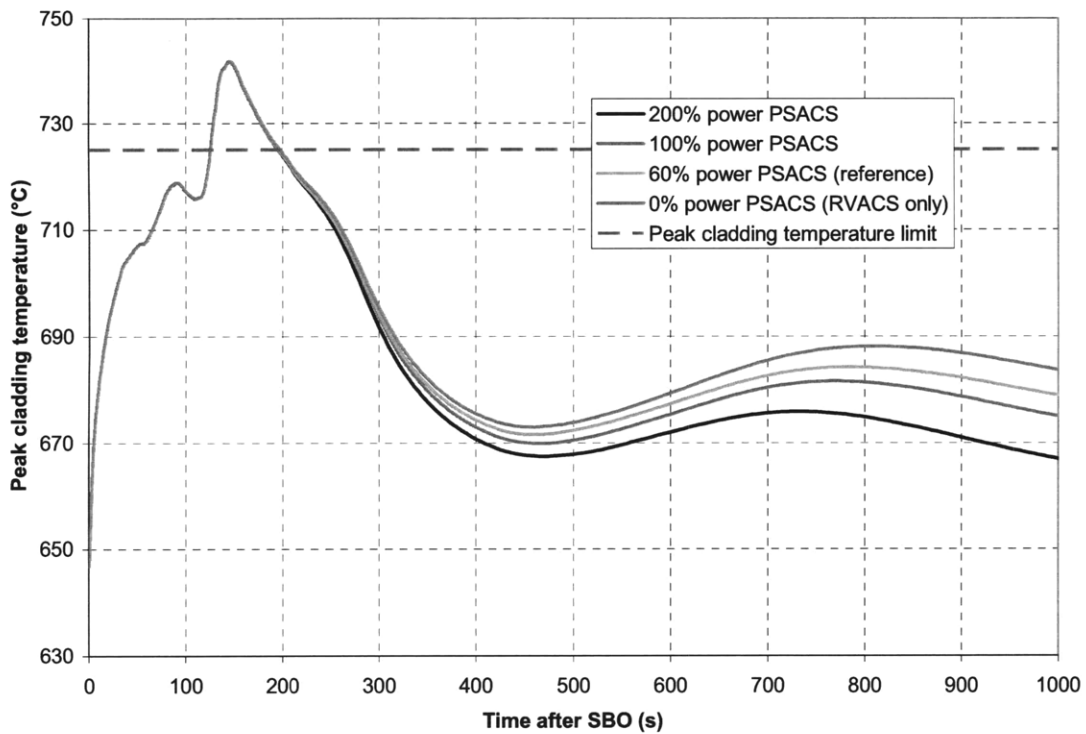


Figure 5.1-4 Effect of changing SBO decay heat removal

An alternative means of addressing reactor transient performance is to modify core steady-state operating characteristics to provide a larger margin to cladding failure. This can be implemented in several ways: the coolant inlet temperature can be decreased, core power density can be decreased, or the coolant flow rate can be increased. Decreasing the coolant inlet temperature by 20°C would also reduce the transient peak cladding temperature by about 20°C, below the 725°C limit. However, this option would also reduce the margin to coolant freezing, and lower system temperatures would also reduce the efficiency of the power conversion system (a 20°C decrease corresponds to a ~5% reduction in Carnot efficiency.) Lowering the core power density below 130 kW/l would reduce the film temperature rise and the transient peak cladding temperature, but would require either a lower power level or a larger reactor vessel. Even though a 100 kW/l

lead-cooled core is able to fit in a 10.2 m diameter vessel, a 100 kW/l salt-cooled core would not because it requires larger IHXs.

Increasing the steady-state coolant flow rate is a way to increase the cladding temperature margin without sacrificing system performance. A new primary system was designed that could accommodate a coolant flow rate of 40,000 kg/s, versus 32,800 kg/s for the reference design. The high-flow-rate core has coolant inlet and outlet temperatures of 505°C and 565°C respectively, versus 496°C and 569°C for the reference core, and the IHXs were redesigned to maintain the same secondary side temperatures and pressures. Increasing the coolant flow rate therefore doesn't impact overall system performance outside of raising system pressure losses, which can be overcome through the use of larger pumps. Most importantly, the high-flow-rate core has a steady-state peak cladding temperature of 633°C, 15°C lower than that of the reference core. However, this increased margin does not translate to the same larger margin during a transient; rerunning the SBO transient yields the results shown in Figure 5.1-5. While there is a slight reduction in peak cladding temperature during the transient, about 5°C, the higher flow rate core similarly experiences a rapid decrease in core flow rate and quickly loses its extra coolant velocity. In summary, adjusting the liquid-salt core's steady-state parameters to reduce peak cladding temperature during an SBO requires a sacrifice in reactor performance, since the only method which doesn't sacrifice performance, increasing the core flow rate, does not have a large effect on transient peak cladding temperature.

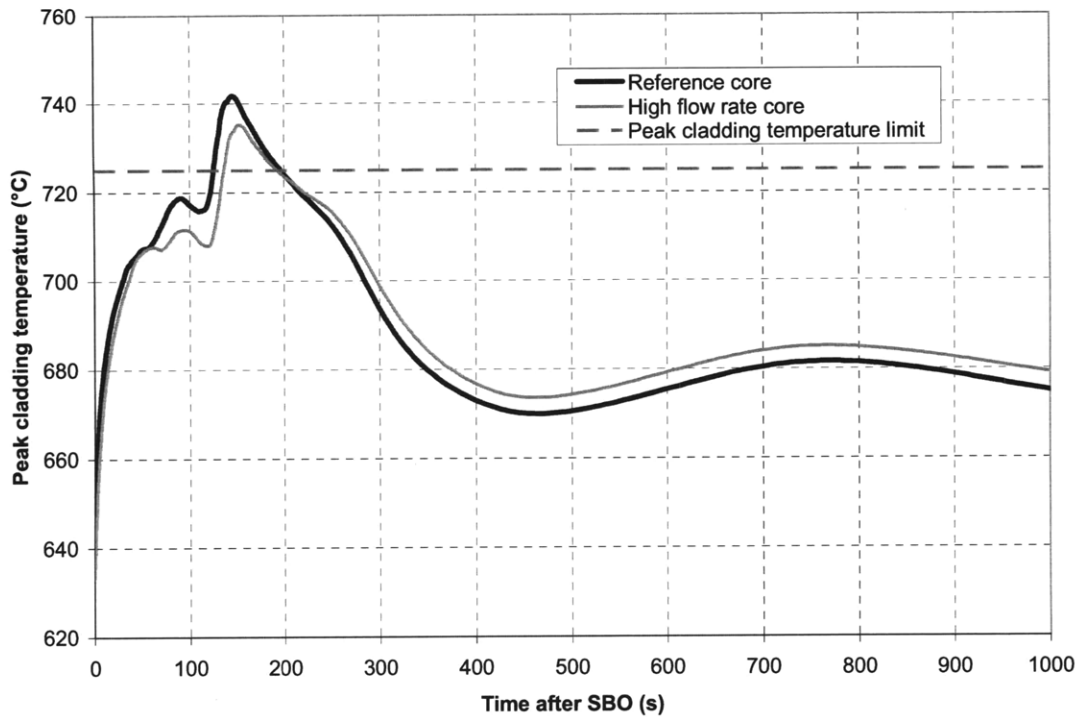


Figure 5.1-5 Peak cladding temperatures for a high flow rate core

The initial peak in the maximum cladding temperature occurs primarily because the heat transfer coefficient decreases more quickly than reactor power, so it can be lowered either by making reactor power decrease more quickly or the coolant flow rate decrease more slowly. For example, in the bounding case of a reactor scram, reactor power decreases very quickly and the peak cladding temperature actually falls instead of rising immediately after an SBO. Reactor power can also be made to decrease more quickly through stronger reactivity feedbacks, which can be instituted by adding LEMs, however this approach would displace fuel rods and therefore increase peaking. Another option is to add flywheels or another form of energy storage to the reactor coolant pumps, so the coolant flow rate and heat transfer coefficient don't decrease as rapidly. Peak cladding temperatures for the flywheel case and the reactor scram case are illustrated in Figure 5.1-6. The same double peaked behavior can be observed in the flywheel

case, although the second peak now occurs later because the coolant flow rate decreases more gradually.

Increasing pump inertia is an attractive solution because it does not require sacrificing core steady-state performance. However, implementing this solution could be challenging: the case plotted in Figure 5.1-6 assumes that the pumps' moment of inertia increases from 28,700 kg-m² to 50,000 kg-m², or 5,325 kg-m² per pump. This inertia increase is equivalent to the addition of a depleted uranium ring 20 cm thick (50cm inner radius, 70cm outer radius), 1 m tall, and weighing 14.4 metric tons to each reactor coolant pump. At steady state, each cylinder would store approximately 380MJ in rotational energy. Different energy storage mechanisms (such as batteries) may be an option if the mechanical engineering of such large flywheels is problematic.

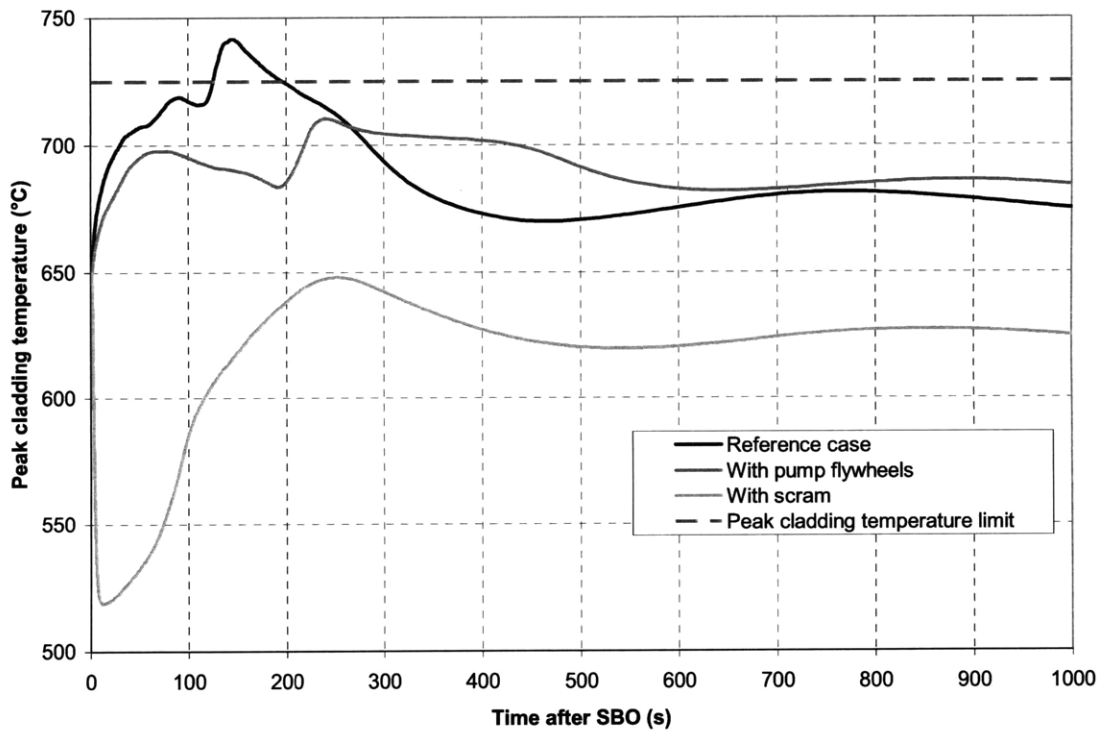


Figure 5.1-6 Effect of pump flywheels and a reactor scram on SBO response

Finally, it may be possible that a peak cladding temperature exceeding 725°C for a brief period of time may be acceptable. The 725°C limit was established because it corresponds to the temperature at which fuel-cladding eutectic formation begins. However, not much interaction occurs at this onset temperature, and even at 100°C above the eutectic temperature, the eutectic penetration into cladding is minimal in one hour [Chang, 2007]. Therefore, it is unlikely that the short-duration temperature excursion above 725°C encountered during an SBO would lead to cladding failure. Furthermore, since the cladding would already not be reusable for structural reasons after a high-temperature transient, the presence of some fuel-cladding interaction would not change the implications of an SBO. Another possibility would be to use a multilayer rolled metal foil that is laser tackwelded to form a tube, which can be inserted between the fuel and the cladding to form a barrier and prevent eutectic formation [Taylor and Wadkamper, 1994].

In summary, the SBO transient is more challenging for a liquid salt reactor than for a lead-cooled reactor in the short term because of tighter thermal hydraulic margins and the poorer heat transfer characteristics of liquid salt. The salt heat transfer coefficient decreases more rapidly than core power, causing the film temperature rise to increase about 70% during a transient, although there is some uncertainty in the exact behavior because the calculated behavior depends on the correlations adopted. This in turn causes the peak cladding temperature to briefly exceed the 725°C limit. Several measures can be adopted to reduce the peak cladding temperature. First, the core can be redesigned to provide a larger peak cladding temperature margin, but doing so would require sacrificing steady-state performance. Another set of solutions would be to strengthen reactivity feedbacks by adding LEMs or to store energy in the primary coolant pumps so the coolant flow rate does not decrease as rapidly. However, it is unlikely that exceeding

725°C for a few minutes during an SBO would lead to fuel failure, which suggests that the transient behavior of the unmodified reference core could also be found acceptable.

Long term SBO response

The long term response of a reactor system to an SBO transient is primarily governed by the design of its passive heat removal systems, since no heat is removed through the power conversion system. With the RVACS design being more or less been fixed to remove as much heat as possible through the vessel walls, the major design options available involve the design of the PSACS system. The PSACS has two major parameters that can be adjusted: the amount of power it can remove, based mainly on the design of the PAHXs, and how much total energy it can absorb, based on the sizing of the PSACS water tanks. By varying these parameters, several long term response behaviors are possible, discussed below.

Figures 5.1-7 and 5.1-8 show the reactivity and fission power of the salt core following an SBO transient for a variety of PSACS power capacities. These figures show that irrespective of PSACS design, the high temperatures of the short-term SBO response introduce significant negative reactivity that shut down the reactor within the first 2000 seconds. (Note that fission power in an actual reactor has a minimum background value due to spontaneous fission; the RELAP model employed does not account for this minimum and allows fission power to drop to 2E-38W.)

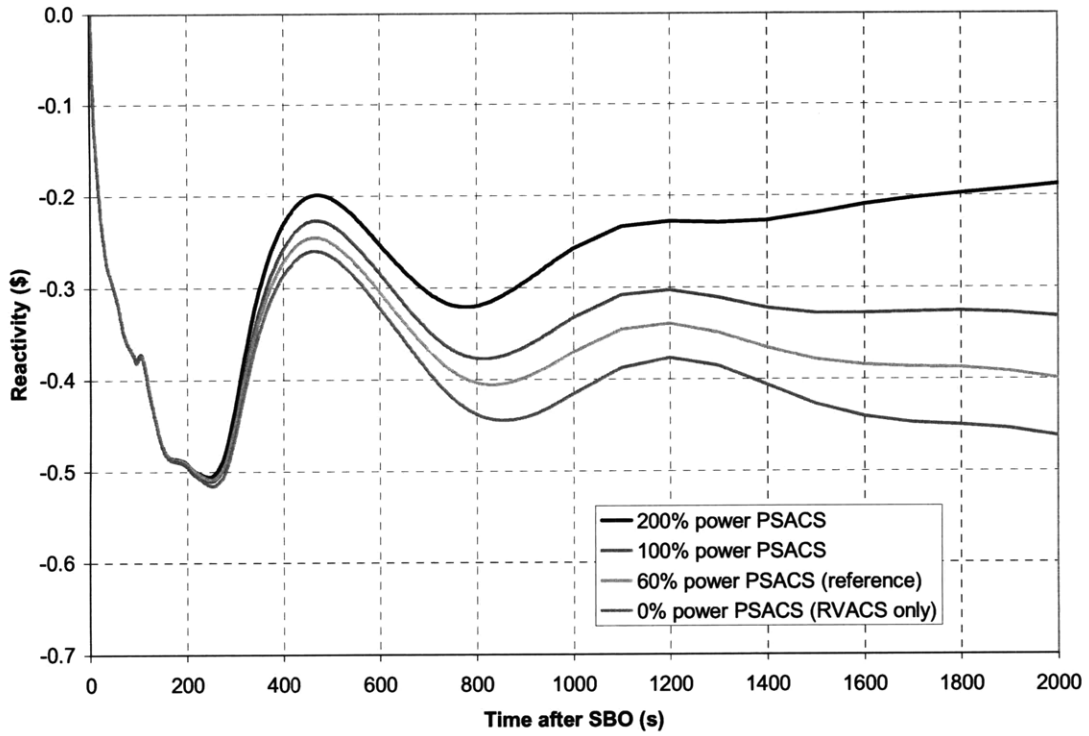


Figure 5.1-7 CR=1 reactivity following an SBO

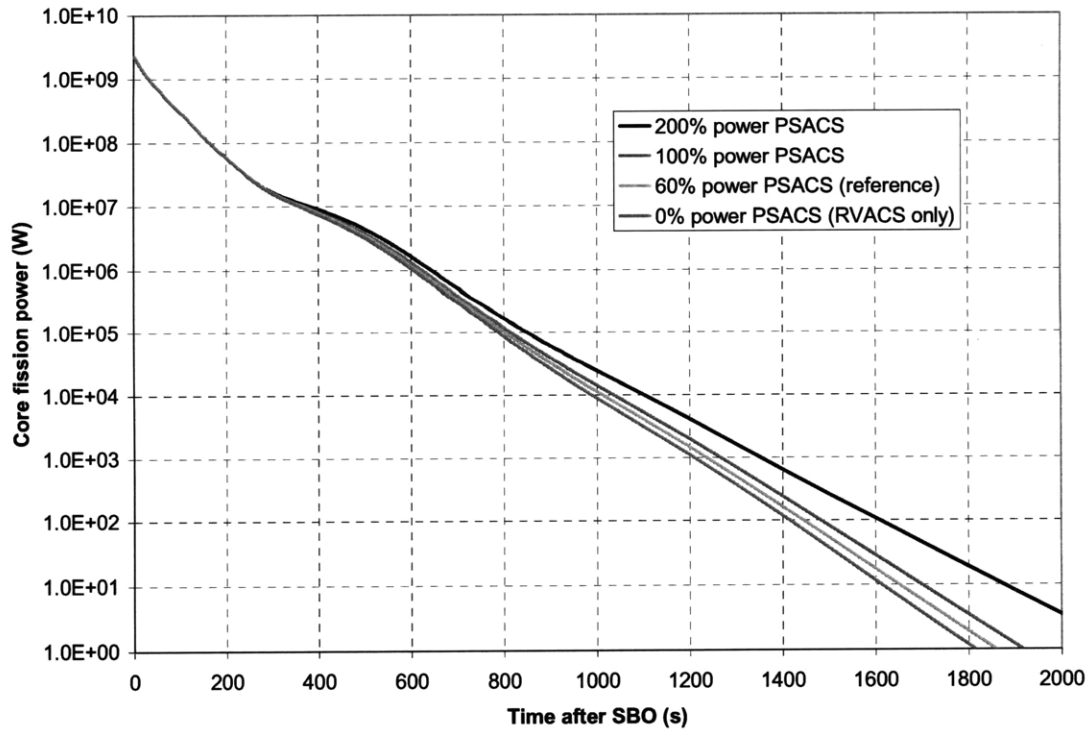


Figure 5.1-8 CR=1 Fission power following an SBO

Past this initial shutdown, several possibilities exist depending on the design of the PSACS system. The designations and geometries of the different PSACS design iterations are given in Table 2.3-5. The first design considered was the reference design for the lead reactor PSACS: 700 four-meter-long heat exchanger tubes per PAHX, with a 6m diameter, 12m tall PSACS water tank. This corresponds to the 200% PSACS power case shown in the short-term response results. Long term peak cladding temperature, reactivity, and power results for this design are shown in Figures 5.1-9 through 5.1-11. Several important features are evident: first, at around 1.6 hours into the transient, reactivity becomes positive. This occurs because the amount of the heat removed by the RVACS and PSACS exceeds the decay heat, causing coolant and fuel temperatures to decrease and reactivity to increase. About one hour after reactivity becomes positive, the reactor restarts and quickly settles on a steady state power of about 30 MW, corresponding to a peak cladding temperature of 632°C. In reality, there would not be such a long delay between reactivity becoming positive and a reactor restart. The lengthy delay is an artifact of the model used; it does not take into account the minimum background fission power, so RELAP calculates the fission power as falling for all 1.6 hours reactivity is negative, reaching a minimum of 3E-8W. As a result, it takes a long time for fission power to grow from this tiny value to the 30 MW steady state power. An actual reactor would drop to a minimum fission power on the order of 100W due to spontaneous fissions, which would more quickly grow to several MW once reactivity becomes positive. Overall this inaccuracy does not qualitatively affect the results obtained; if minimum fission power had been taken into account one would simply expect smaller oscillations as the system approached steady state.

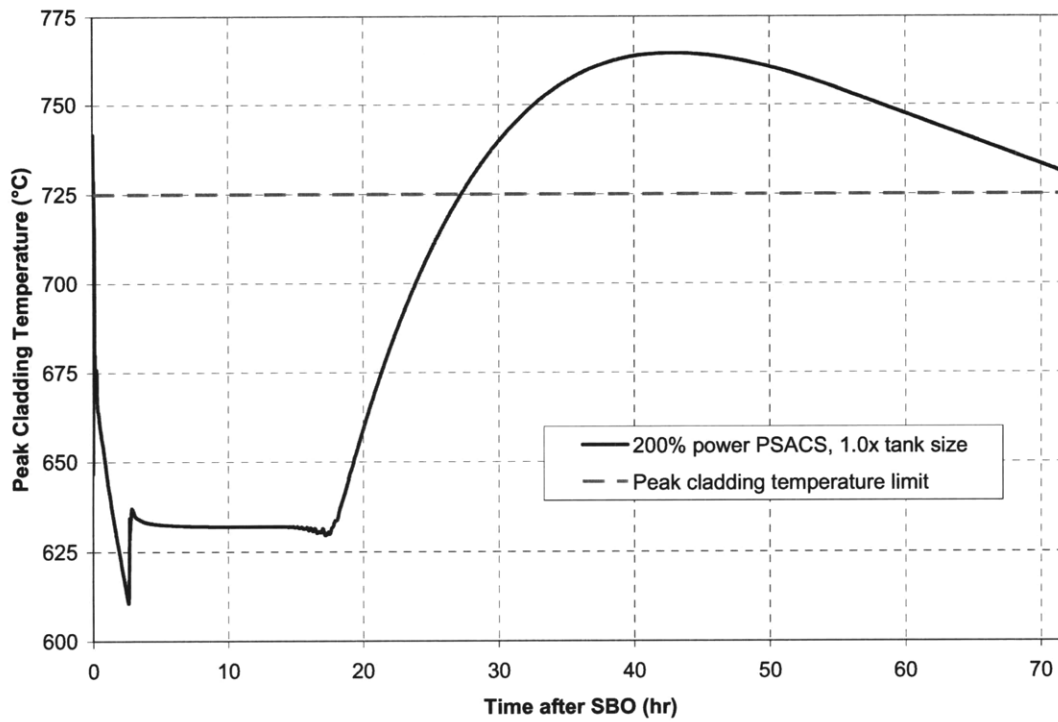


Figure 5.1-9 CR=1 long term peak cladding temperature response to an SBO

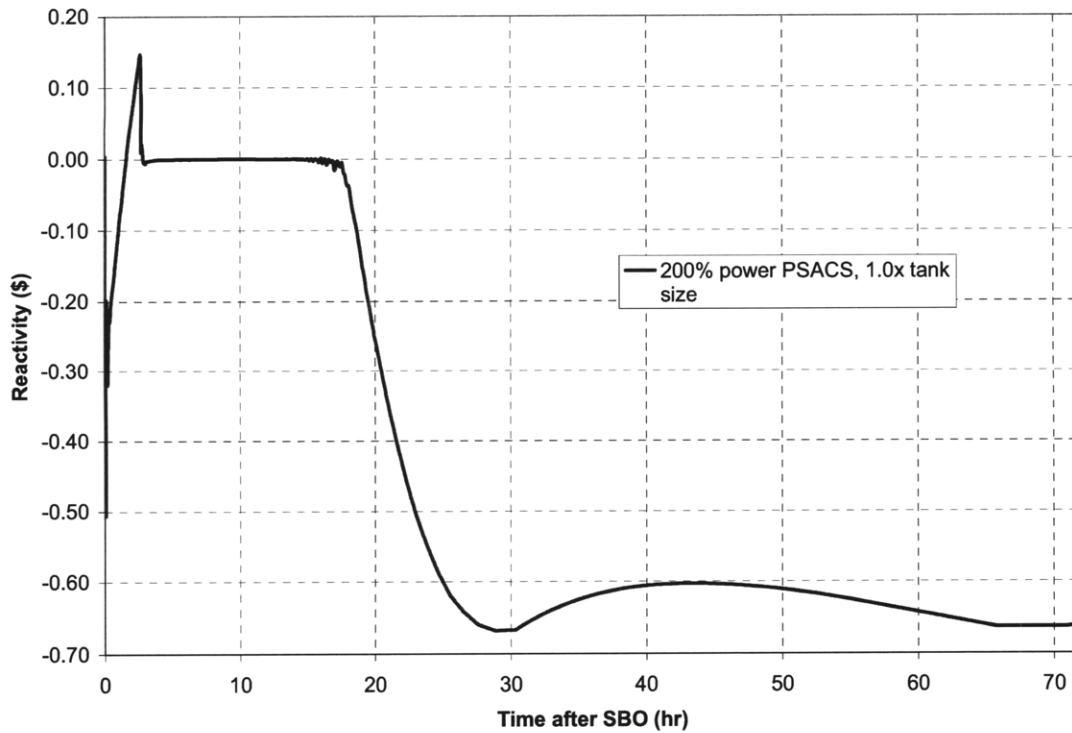


Figure 5.1-10 CR=1 long term reactivity response to an SBO

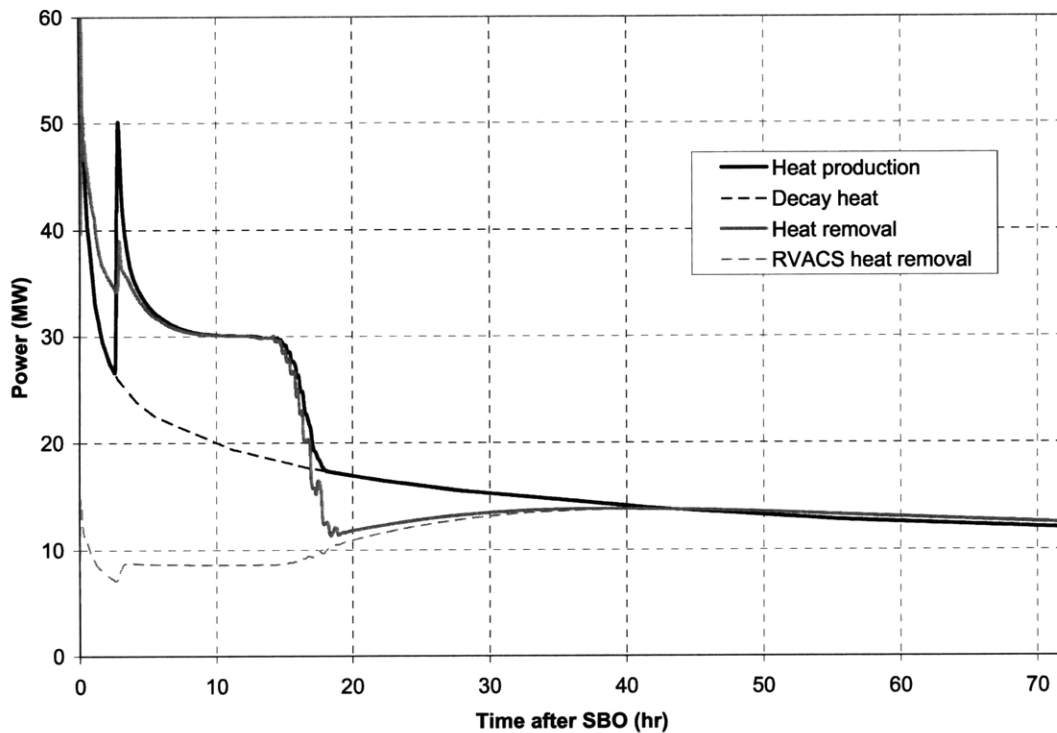


Figure 5.1-11 CR=1 long term power response to an SBO; 200% power PSACS, 1.0x tank size case

At approximately 18 hours, the system leaves steady state and begins to heat up, and the reactor shuts down once again. This is due to evaporation in the PSACS water tanks; the power removed via the PSACS rapidly falls to zero as the water level falls below the heat exchanger tubes. RELAP has difficulty modeling the PSACS system after this occurs (possibly because of nearly stagnant CO₂ flow conditions or heat transfer to air by the PAHXs), so the PSACS system is disconnected at 68,000 seconds (18.9 hours) by closing the PSACS valves (323 and 324). Doing this has little effect on results because the PSACS is already removing very little heat at this point. With the PSACS operating at nearly zero power, heat removal past 18 hours occurs exclusively through the RVACS. Between 18 and 43 hours into the SBO transient, decay heat from the core is greater than the heat removal capacity of the RVACS, so coolant and peak cladding temperatures rise, with the peak cladding temperature exceeding the 725°C limit at

about 27 hours. Unlike during the short term SBO response, the temperature limit is exceeded for a long time, upwards of 45 hours, which could allow significant fuel-cladding eutectic formation and lead to fuel failure. Therefore a different PSACS design is needed to ensure passive long-term safety for the liquid salt reactor.

One option is to increase the size of the PSACS water tanks. This would allow the low-power steady-state period to last longer and give more time for reactor decay heat to subside. This was implemented in RELAP by making the PSACS water tanks much larger (34m high) and setting the PSACS disconnect time to correspond to a desired amount of energy removed. For example, to simulate PSACS tanks that are approximately twice as large, a PSACS disconnect time of 130,000 seconds (~36 hours) is chosen, since 36 hours is roughly twice the 18 hour duration the initial tank design can remove heat for. This approach is used so that tank size can be simulated by varying only one parameter (disconnect time), rather than having to manually adjust the tank size and then determining the appropriate disconnect time needed for computational stability. Since the power removed through the PSACS drops rapidly as the PAHX heat exchanger tubes become exposed to air, switching PSACS power quickly to zero by disconnecting the PSACS is a reasonable approximation. Later the total amount of energy removed via the PSACS can be computed to determine the equivalent amount of water needed in the PSACS tank.

Peak cladding temperature results for the large-tank case are shown in Figure 5.1-12. The total amount of energy removed through the PSACS in this case is 2.1 times that removed in the initial case, corresponding to a PSACS tank containing 2.1 times as much water. Larger PSACS tanks give decay heat more time to diminish, allowing the RVACS to keep the reactor below the

peak cladding temperature limit once the PSACS is depleted. However, doubling the size of PSACS tanks would raise capital costs, since the starting design has tanks that are already a large 6m in diameter and 12m high. Also, the 200% power PSACS design encounters the same difficulty as the 100% power design discussed later: during protected transients the high heat removal rate through the PSACS can lead to coolant freezing.

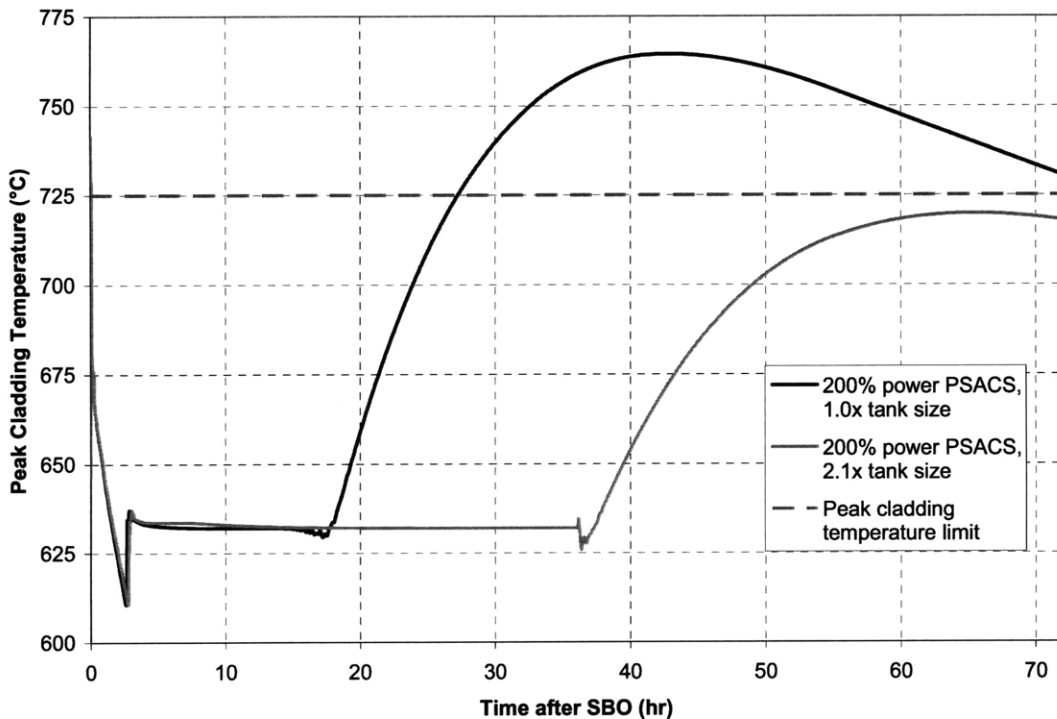


Figure 5.1-12 CR=1 long term peak cladding temperature response to an SBO

Another approach that would yield the same benefit as larger tanks without raising capital costs would be to decrease the heat removal capacity of the PSACS. This can be accomplished in practice by reducing the number and length of heat exchanger tubes in the PAHXs. Doing so would reduce the rate at which PSACS water is boiled off and therefore extend the duration over which the PSACS is effective. A half-power PSACS system was implemented in RELAP by disabling one of the two active PSACS trains. This approach was needed instead of downsizing

the PAHXs because RELAP encounters computational difficulties modeling low-power PSACS trains. Again a PSACS disconnect time of 130,000 seconds was used to simulate the PSACS running out of water. Peak cladding temperature results for this case are shown in Figure 5.1-13. While the smaller PSACS causes temperatures to rise somewhat initially, it is able to sustain low-power steady state operation long enough to prevent overheating, while only requiring a PSACS tank 1.1 times larger than the initial design.

This low-power PSACS design was originally selected as the reference design because of its ability to successfully mitigate an unprotected SBO without increasing capital cost requirements. Because it utilizes a reactor restart, it is a robust design in that its performance is largely independent of the number of PSACS trains operating. As long as more than 2 trains are running the reactor will not exceed 725°C after the initial shutdown. After the subsequent restart, the reactor will assume steady state operation at a power level equal to that removed by all the PSACS trains and the RVACS: about 20 MW when two PSACS trains are operating (11MW through PSACS and 9 MW through RVACS) and about 30 MW when all four trains are operating (21MW through PSACS and 9 MW through RVACS). Due to the favorable reactivity coefficients made possible by LEMs, the coolant and fuel temperatures are very similar regardless of the restart power level. Since each PSACS train has its own water tank, this steady state will last until approximately 36 hours into the transient regardless of how many PSACS trains are operating. An unprotected SBO with all PSACS trains running would result in a response similar to the large tank case shown in 5.1-12.

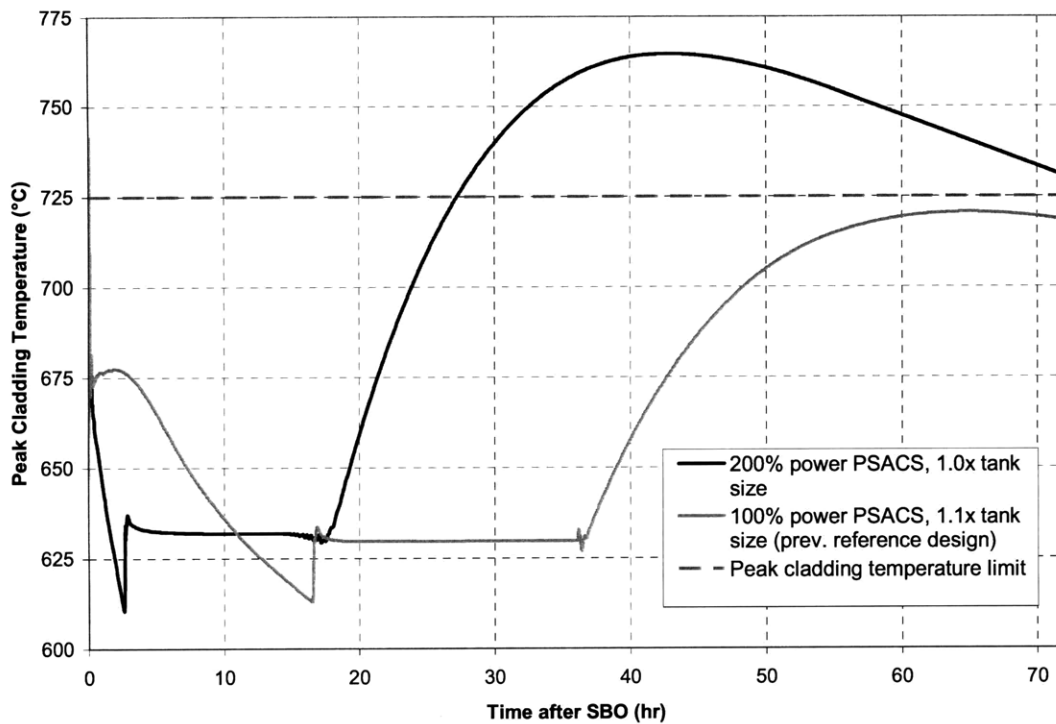


Figure 5.1-13 CR=1 long term peak cladding temperature response to an SBO

While reliance on a reactor restart in the original reference design makes for a robust system, it means that transient behavior during a protected transient would be different, since a scram would prevent a restart from occurring. Investigations of a protected transient showed that with all four 100% power PSACS trains operating, decay heat removal through the PSACS was sufficient to cause coolant freezing within the first 20 hours of an SBO transient. The details of this analysis are given in the protected transient subsection.

To resolve the issue of coolant freezing during protected transients, the power level of the PSACS system was further reduced. Through trial and error it was found that PSACS with a heat removal capacity 60% that of the reference case is just sufficient to prevent the peak cladding temperature from exceeding 725°C with only two trains operating. Peak cladding

temperature, reactivity, and power results for this case are shown in Figure 5.1-14 through 5.1-16. By sizing the PSACS tanks such that each tank runs out of water 36 hours or later into the transient (about 75% the size of the initially designed tanks) allows the peak cladding temperature limit to be satisfied for times past 36 hours. Note that in this reduced-power PSACS design, reactor temperatures never become low enough to cause a restart with just two trains running. With three or four trains running, a reactor restart would occur like with the 100% power PSACS case, and the transient would similarly be safely mitigated. Because of the similar robustness of the 60% power PSACS design and its additional ability to mitigate protected transients, it was selected as the reference PSACS design for the salt-cooled FCR reactor.

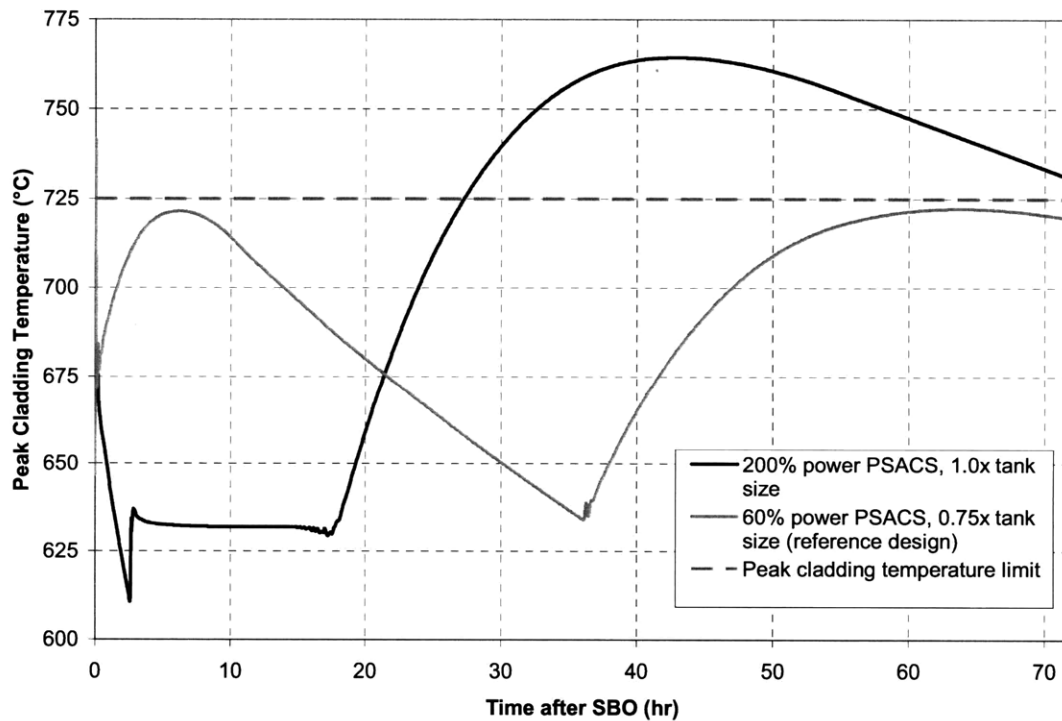


Figure 5.1-14 CR=1 long term peak cladding temperature response to an SBO

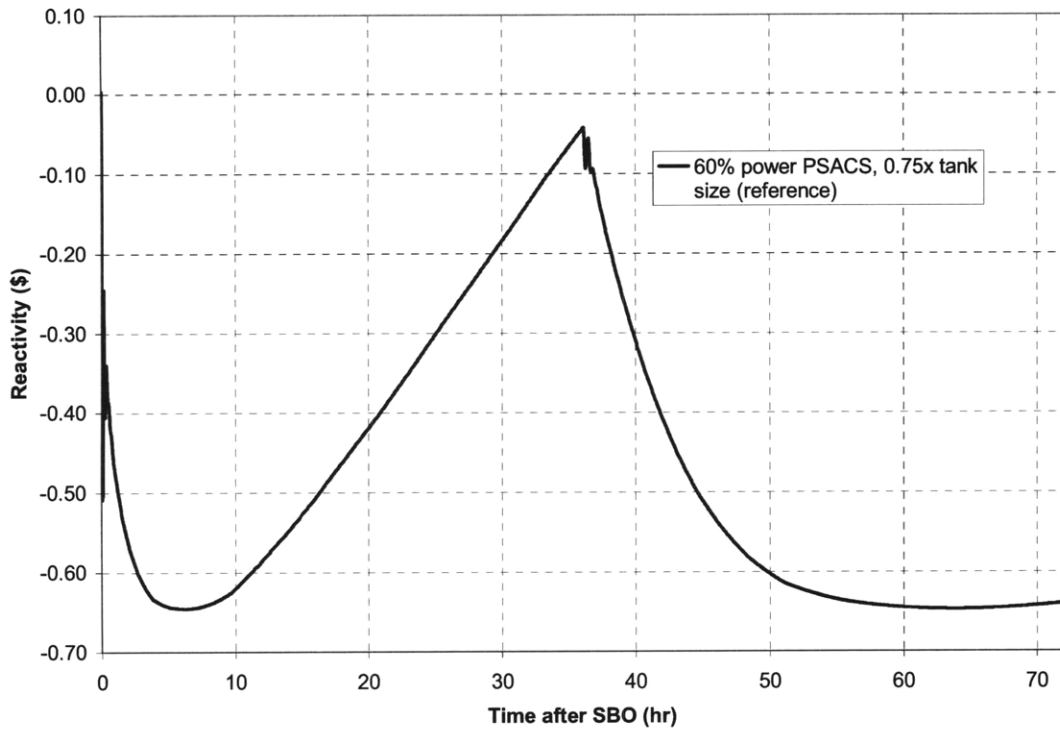


Figure 5.1-15 CR=1 long term reactivity response to an SBO

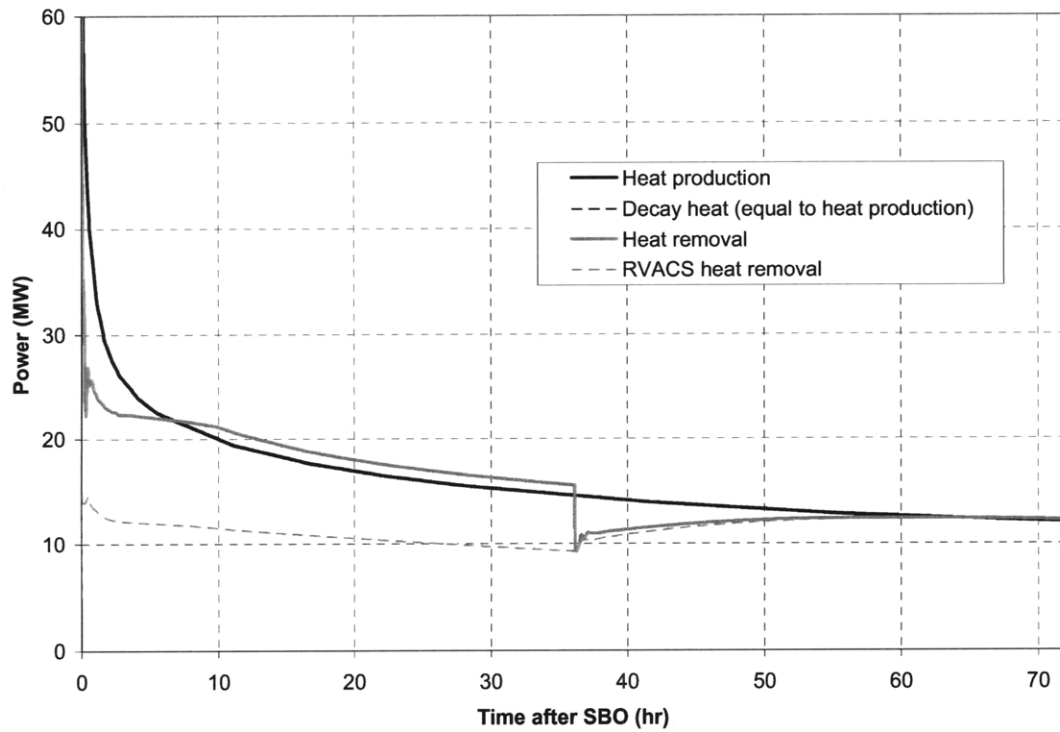


Figure 5.1-16 CR=1 long term power response to an SBO; 60% power PSACS, 0.75x tank size case

Overall, a liquid salt reactor can be designed to passively mitigate an unprotected station blackout transient. Short and long term responses for the reference design are shown in Figures 5.1-4 and 5.1-14. The poor heat transfer characteristics of liquid salt cause it to briefly exceed the cladding temperature limit of 725°C immediately after the transient begins, but this is unlikely to cause fuel failure and can be avoided through the use of higher inertia pumps. Reactivity feedbacks, including that due to LEMs, cause the reactor to shut down within the first 1000 seconds. Past this initial shutdown, cooling by the PSACS and RVACS causes reactivity to rise again, resulting in a reactor restart into a low-power steady state if three or four PSACS trains are operating. Regardless of the number of PSACS trains operating (2, 3, or 4), PSACS operation is sustained until about 36 hours after the transient begins, after which the PSACS tanks are depleted and all cooling occurs through the RVACS. At 36 hours, decay heat is low enough that the RVACS is sufficient to keep the core peak cladding temperature below its 725°C limit.

5.2 CR=1 unprotected loss of flow

An unprotected loss of flow accident (LOFA) is similar to an unprotected SBO in that power to the reactor coolant pumps is lost, generators are decoupled due to loss of load, and there is a failure to scram. Therefore, a LOFA transient can be mitigated in exactly the same manner as an SBO: by diverting secondary side flow from the power conversion system to the PSACS.

However, unlike during an SBO, pre-cooler pumps are assumed to be operational and controllable during a LOFA, which allows the power conversion system to be used for heat removal, thus removing the need to operate the PSACS.

As for during an SBO, loss of load at the generators can cause turbine overspeed unless part or all of the secondary flow through the turbines can be diverted. In an SBO, where the secondary system cannot be used to remove decay heat, this is done by shutting the power conversion system isolation valves (valves 302 and 326 in the model) and opening the PSACS valves (323 and 324). During a LOFA, some flow through the power conversion system is desired to remove heat through the precoolers, so instead turbine bypass valves (306) are used to allow a fraction of the secondary flow to bypass the turbines completely. Flow in the secondary is maintained by the spinning turbines, which remain connected to the secondary-side compressors. The amount of heat removed via the power conversion system depends on the flow rate in the secondary, which in turn depends on turbine speed. Turbine speed can be controlled by adjusting the position of the turbine bypass valves. By controlling the bypass valves with proportional-integral controllers, turbine speed can be brought to a desired setpoint following a LOFA.

The proportional-integral controller is implemented in RELAP by setting the valve stem position of the turbine bypass valve to a proportional-integral control variable. The functional form of this control variable is:

$$Y = S \left[A_1(V - V_i) + A_2 \int_0^t V - V_{\text{set}} dt \right] \quad (5.2-1)$$

Here Y is valve stem position, which has a value between 0 and 1 and is related to the normalized valve area by the function shown in Figure 5.2-1. A larger valve stem position corresponds to a more opened bypass valve and less flow through the turbine. S is a scaling factor which has the value 0.02. V is the turbine angular velocity, with V_i being the initial velocity (376.99 rad/s) and

V_{set} the turbine setpoint velocity. A_1 and A_2 are the proportional and integral weights; adjusting these weights and the setpoint velocity fully determines the behavior of the valves.

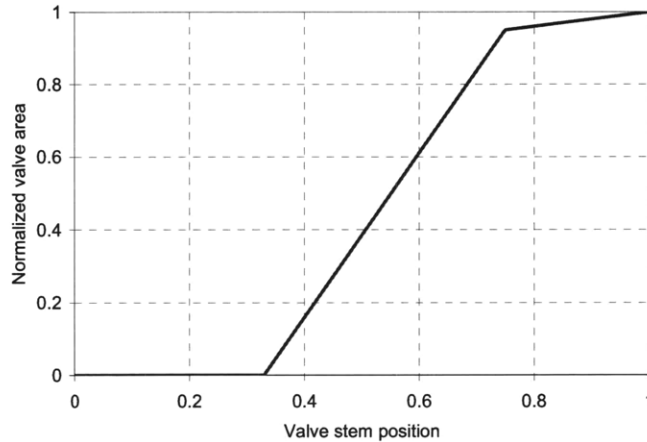


Figure 5.2-1 Normalized valve area as a function of valve stem position

Depending on the design of the proportional integral valve controller, two LOFA mitigation strategies are possible. The first strategy, adopted as the reference case, uses a turbine speed setpoint of 25 rad/s, and proportional and integral weights of 2.9 and 0.02 respectively. The LOFA transient was implemented in RELAP by tripping the reactor coolant pumps and generators at time zero, and opening the turbine bypass valve according to the proportional integral controlled parameters. Also, the water flow rate through the precoolers is reduced to 5% its steady state value to reflect the falling reactor power level. Peak cladding temperature, coolant inlet and outlet temperature, reactivity, and power results for this case are given in Figures 5.2-2 through 5.2-4.

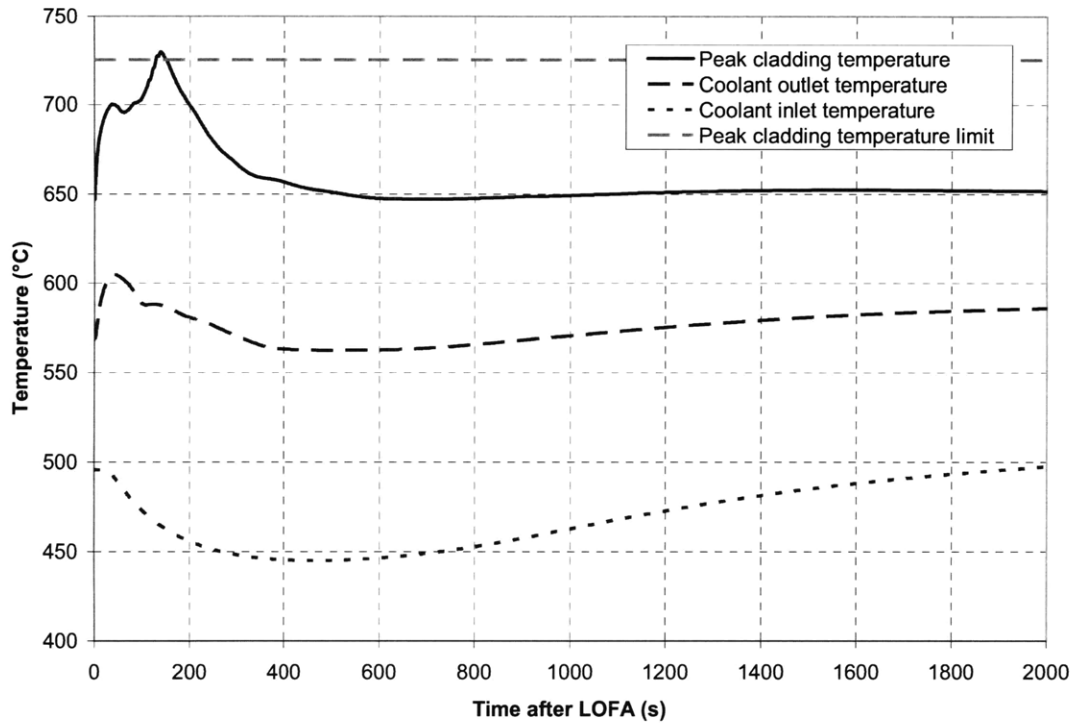


Figure 5.2-2 CR=1 salt reactor temperature response to a LOFA

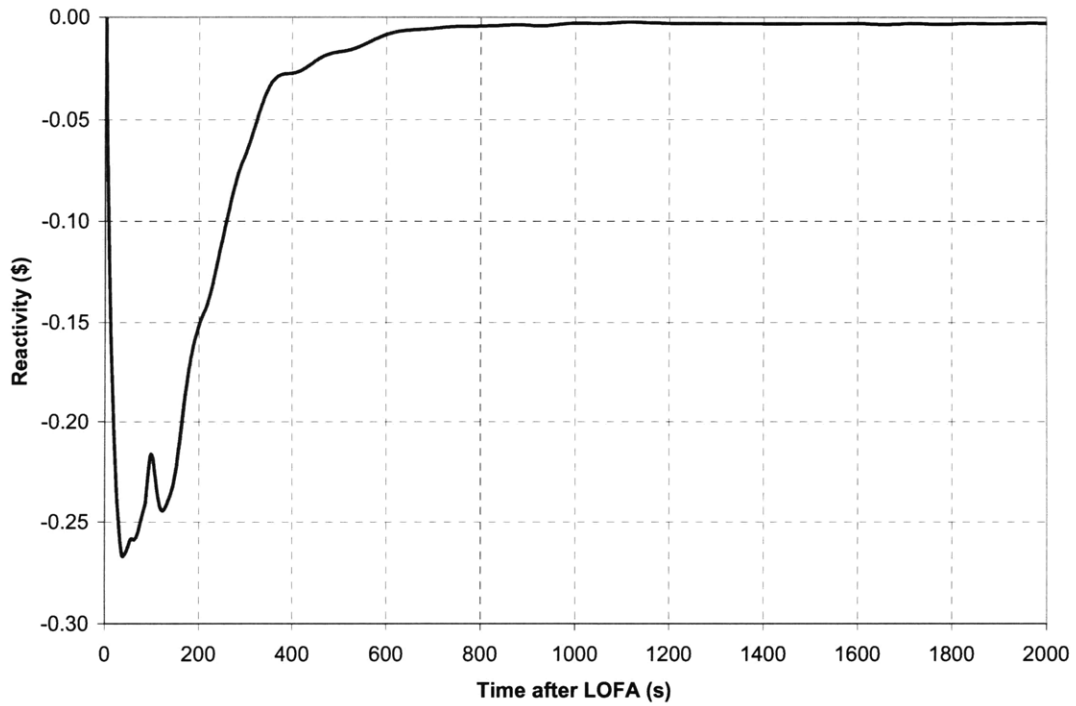


Figure 5.2-3 CR=1 salt reactor reactivity response to a LOFA

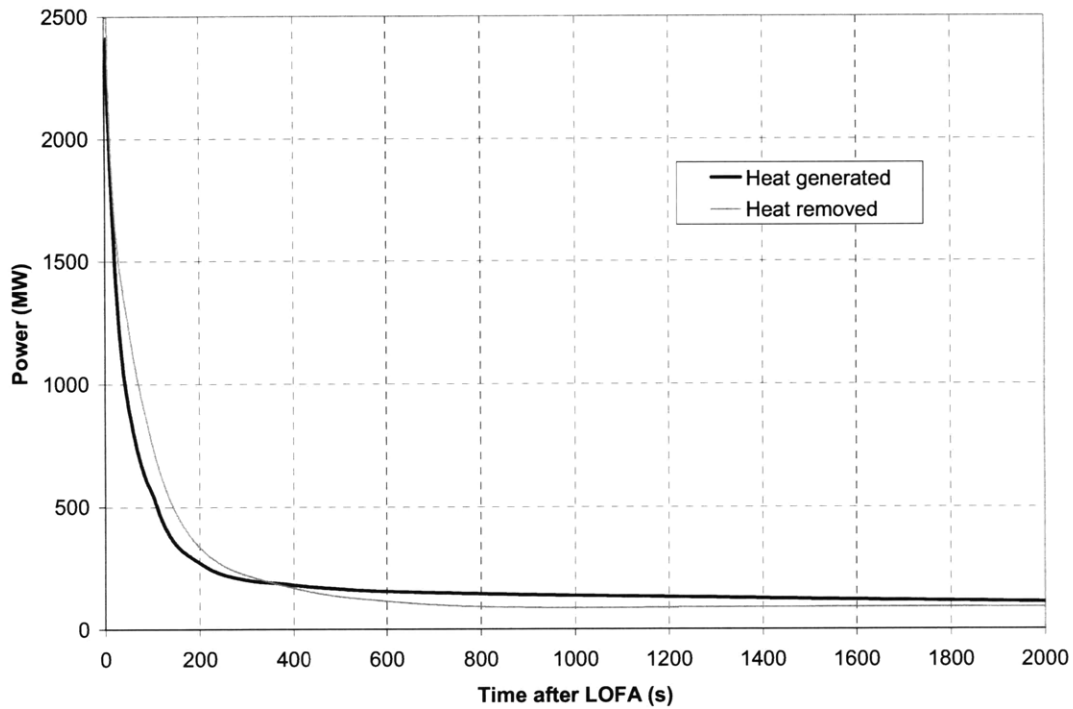


Figure 5.2-4 CR=1 salt reactor power response to a LOFA

Like with an SBO, loss of power to the reactor coolant pumps causes the primary flow rate to fall, which increases the film temperature rise in the core and creates a peak in the maximum cladding temperature. Increases in fuel and coolant outlet temperatures (thus LEM temperatures) introduce negative reactivity, which drops the reactor power level. Unlike with an SBO, the high amount of heat removal with the power conversion system actually exceeds reactor power for the first 350 seconds of the transient, so coolant inlet temperatures fall instead of rise. As a result, the initial peak cladding temperature rise is not as severe as for an SBO, and the cladding temperature limit of 725°C is exceeded for only 20 seconds, with a maximum of 730°C. Like for an SBO, this initial peak is unlikely to cause fuel failure and can be avoided using high inertia pumps.

The high rate of heat removal through the power conversion system keeps coolant temperatures low, which means that there is a smaller negative reactivity insertion during a LOFA than during an SBO. As a result the core never experiences a shutdown, instead it settles smoothly into a new steady state at a reactor power of approximately 87 MW, matching the heat removed by the RVACS and power conversion system. This behavior is possible because of the use of a proportional integral controller, which is able to decrease the heat removal capacity of the power conversion system in a similar fashion to the decrease in reactor power. As a result, the system stays close to steady state and doesn't experience the large reactivity swings seen in the SBO case. The PSACS, which are a simpler system that removes an approximately constant power, does not similarly match the drop in reactor power during an SBO, leading to a reactor shutdown and subsequent restart.

Another LOFA mitigation strategy is possible due to the use of LEMs in the salt reactor design. By using the power conversion system to aggressively remove heat from the primary system, it is possible to cool the system enough to cause the LEMs to be fully withdrawn from the core. As shown in Figure 4.3-3 in the LEM design section, this occurs at a coolant outlet temperature approximately 58 degrees below its steady state value. Even before this temperature is reached, the reactivity worth of the LEMs decreases, resulting in a positive overall coolant temperature coefficient. At these decreased temperatures, it is possible for the power reactivity coefficient to reverse sign and become positive, with lower power decreasing reactivity instead of increasing it. This positive feedback quickly shuts down the reactor without the need for a scram.

This rapid cooling shutdown strategy can be implemented simply by adjusting the parameters of the proportional integral controller governing the turbine bypass valve. To do this, the turbine

setpoint velocity is changed to 50 rad/s, and the proportional and integral weights are changed to 2.5 and 0.01 respectively. Results for this case are given in figures 5.2-5 through 5.2-7. Figure 5.2-7 shows how the new controller causes more heat to be removed from the primary system; the effect of this on system reactivity is shown in Figure 5.2-6. Reactivity increases between about 50 and 400 seconds then dramatically turns around in the shutdown case as the LEMs stop contributing reactivity. Results are only given for the first 1300 seconds because at that point the primary coolant freezes at the IHX outlet and the RELAP simulation halts.

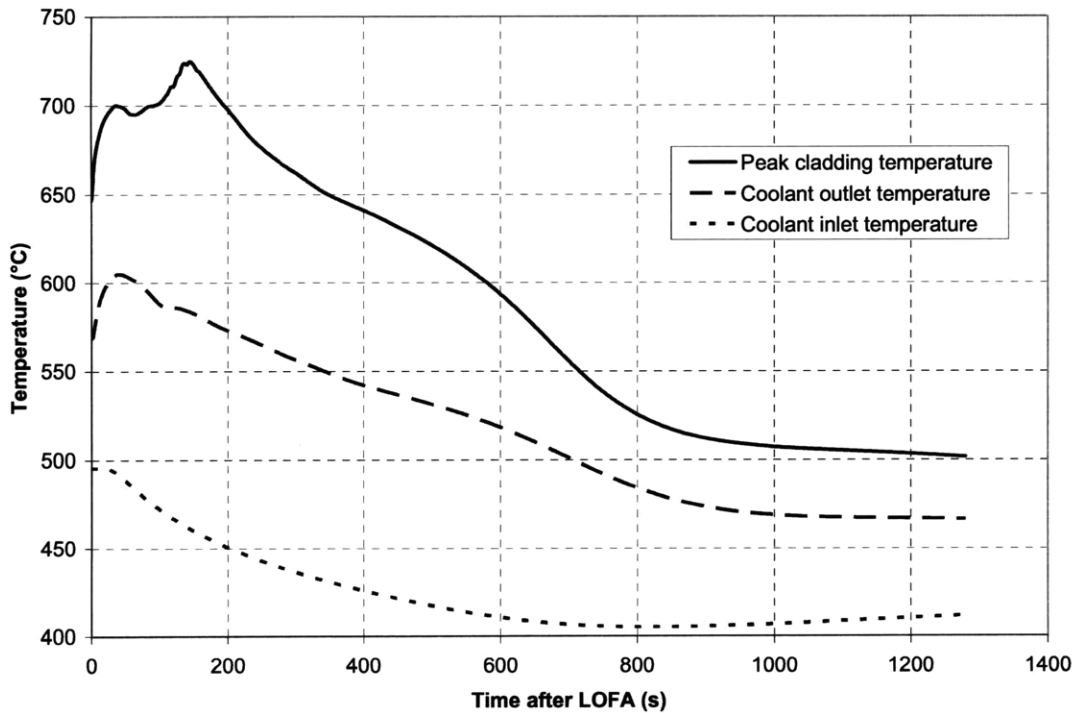


Figure 5.2-5 CR=1 salt reactor temperature response to a LOFA (shutdown case)

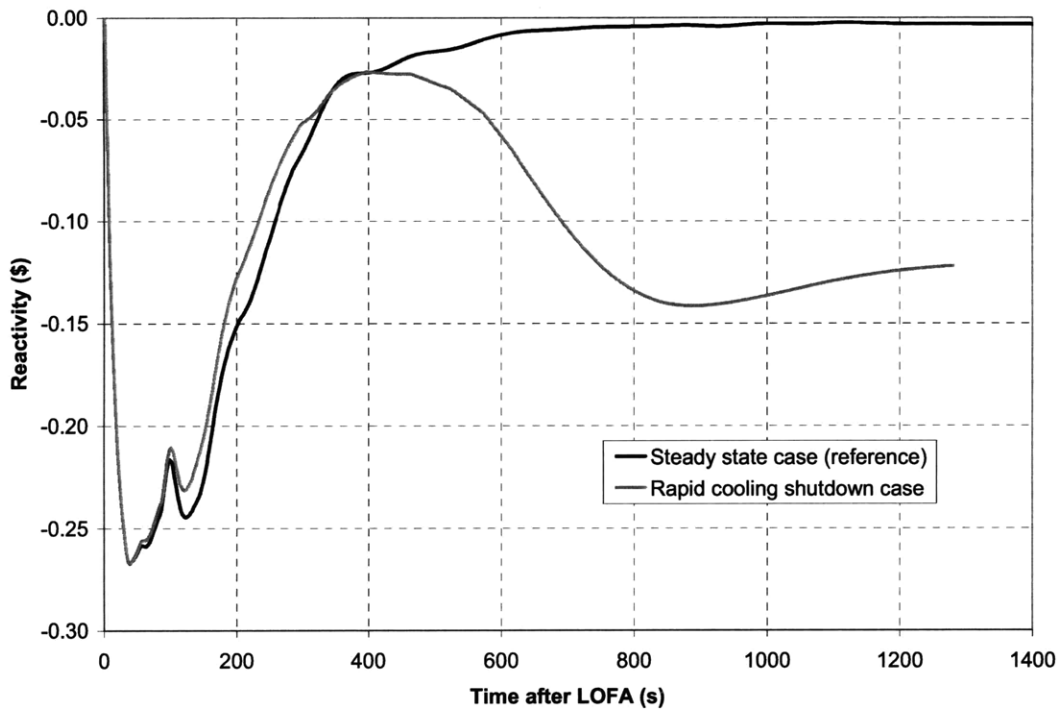


Figure 5.2-6 CR=1 salt reactor reactivity response to a LOFA

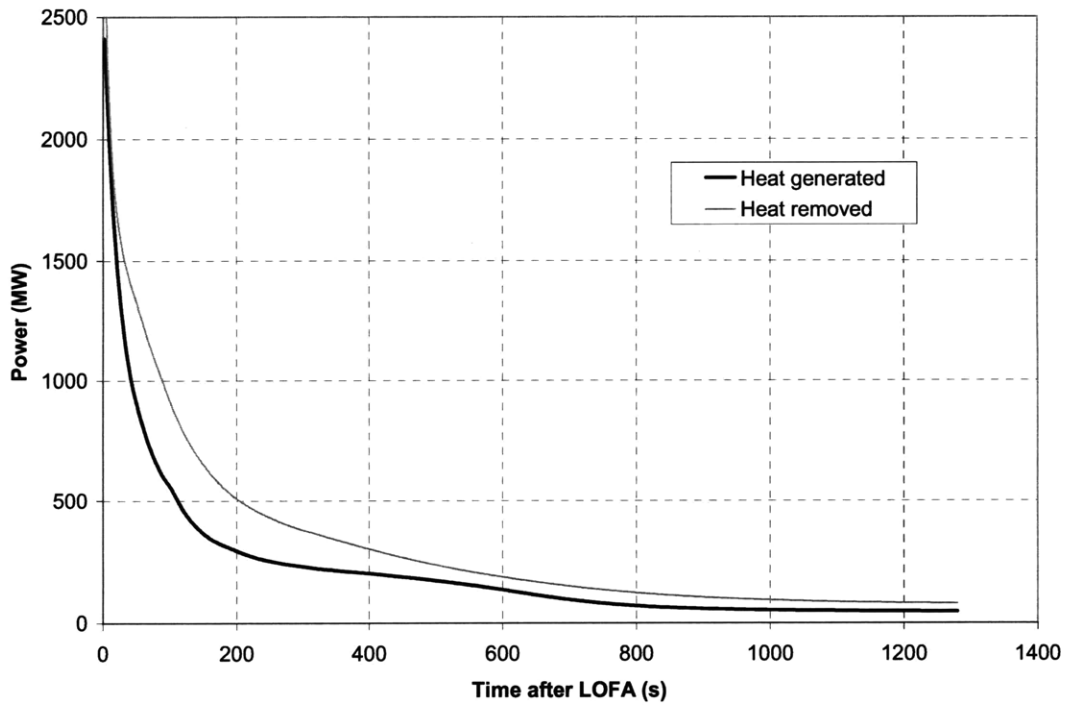


Figure 5.2-7 CR=1 salt reactor power response to a LOFA (shutdown case)

While a passive automatic shutdown may be desirable, this second mitigation strategy as shown would not be employed in practice because it rapidly results in coolant freezing. It is shown here to illustrate that the use of LEMs allows a low temperature reactor shutdown without a scram. In an actual reactor system, an additional control scheme would be needed to reduce the power removed by the PCS following a shutdown to more closely match the decay heat produced. Heaters may also be needed to prevent the coolant from freezing. These additional measures would introduce additional operational challenges, and due to the small margin to coolant freezing, they would need to be employed within the first 25 minutes of a LOFA. Because of this, the earlier case that can automatically converge to a safe steady state was selected as the reference case. Like for the lead reactor, the use of a proportional integral controller to control turbine bypass valves can successfully mitigate a LOFA accident without requiring use of the PSACS system.

5.3 CR=1 unprotected transient overpower

A UTOP assumes that the highest worth control rod cluster in the core is withdrawn at the drive speed of the control rod mechanism, without an accompanying scram to shut down the core. The primary coolant pumps and secondary system continue operating as normal, with the generators remaining attached to the grid.

The unprotected overpower accident (or UTOP, for unprotected transient overpower) is simpler to model than the other transients considered because it does not involve any special response from the secondary system. To calculate the reactivity worth of the highest worth control rod assembly, the maximum reactivity of the core was first determined. For the salt fast reactor,

reactivity is highest when the core average coolant temperature is high, the fuel temperature is low, and when the LEMs are fully withdrawn (corresponding to a low coolant outlet temperature); in other words during hot zero power conditions. MCNP calculations determined the maximum k-effective during hot full power (HFP) conditions with LEMs fully withdrawn (1.0144 for the CR=1 core), corresponding to a reactivity of 3.65 dollars. To obtain the hot zero power (HZIP) reactivity, the difference in reactivity between the fuel at the fuel average temperature (922K, assuming unirradiated values for thermal conductivity) and the fuel at the coolant average temperature (808K) was added to the hot full power reactivity. The total reactivity was divided by the number of control rod clusters to obtain the average worth per cluster. Finally, the maximum control cluster worth was determined by multiplying the average worth by the highest assembly peaking factor squared. A summary of these calculations is given in Table 5.3-1. The rate of withdrawal is taken from IFR safety studies [Wade, 1997].

Modeling a UTOP in RELAP simply involves inserting the calculated amount of reactivity (9.82 cents) at the assumed rate (0.5 cents/second) at time zero. Results for cladding and fuel temperatures, reactivity, and relative power are shown in Figures 5.3-1 through 5.3-3. The initial reactivity insertion quickly raises the power level in the core, which heats up the fuel and coolant and drives reactivity back down. Reactivity peaks at about 3.7 cents and returns to zero at 82 seconds, at which point reactor power reaches a maximum of about 113% its steady state value. Shortly after the peak cladding temperature reaches a maximum of about 668°C, much lower than the 725°C transient limit. Due to the high thermal conductivity of metal fuel, the peak fuel temperature is only 781°C, well below the 1000°C limit. Within the first 1000 seconds the

reactor settles at a new steady state at 101% reactor power and a peak cladding temperature of 666°C.

Table 5.3-1 CR=1 maximum control rod worth

k-effective (max)	1.0144
Excess reactivity (\$)	3.649
HFP to HZP (\$)	0.207
Maximum reactivity (\$)	3.856
# of CR clusters	67
\$/cluster (x25 rods)	0.058
Maximum peaking factor	1.26
Maximum rod worth (\$)	0.091
Rate of withdrawal (\$/s)	0.005

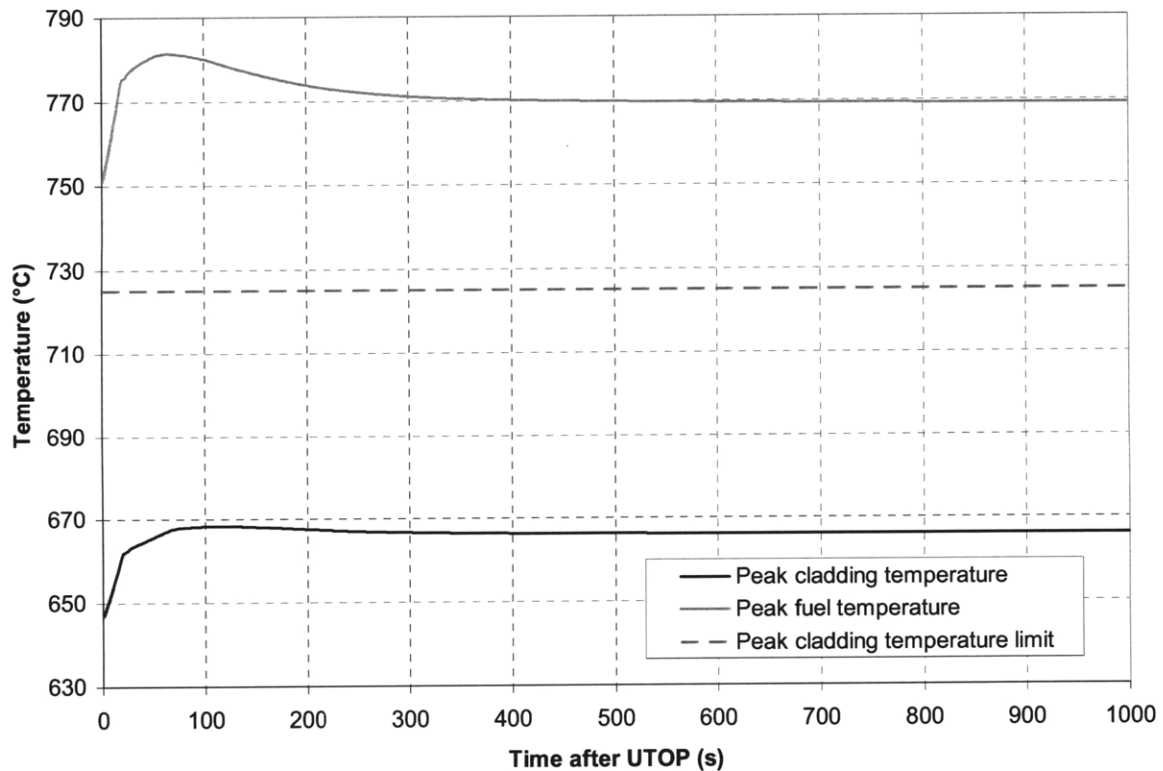


Figure 5.3-1 CR=1 salt reactor temperature response to a UTOP

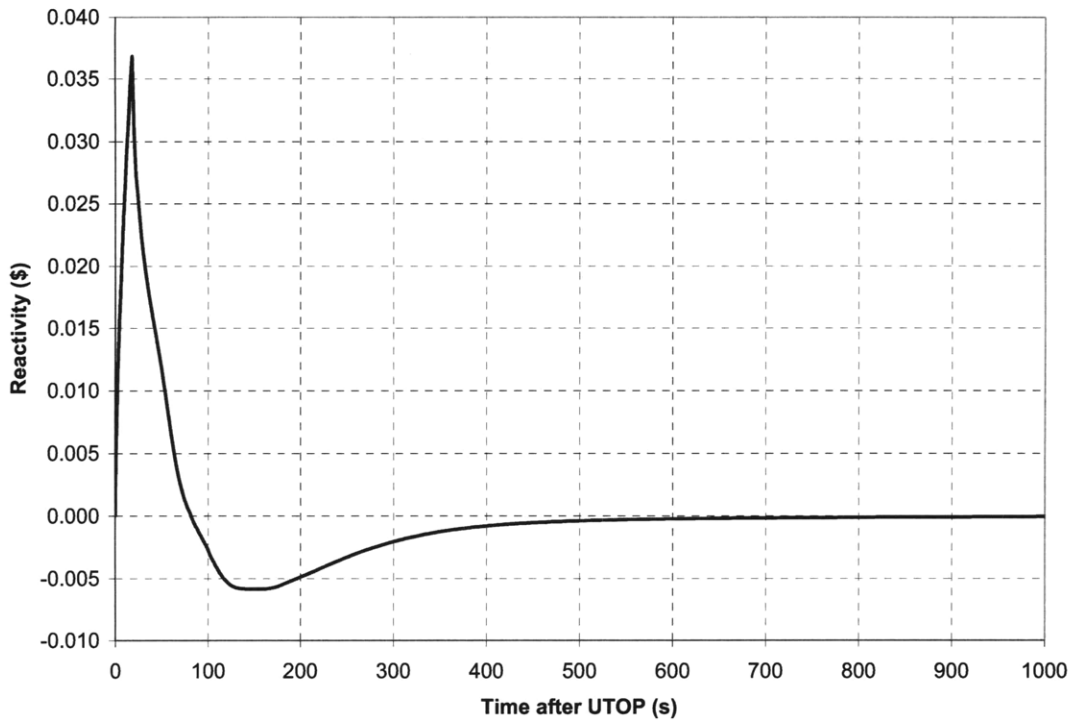


Figure 5.3-2 CR=1 salt reactor reactivity response to a UTOP

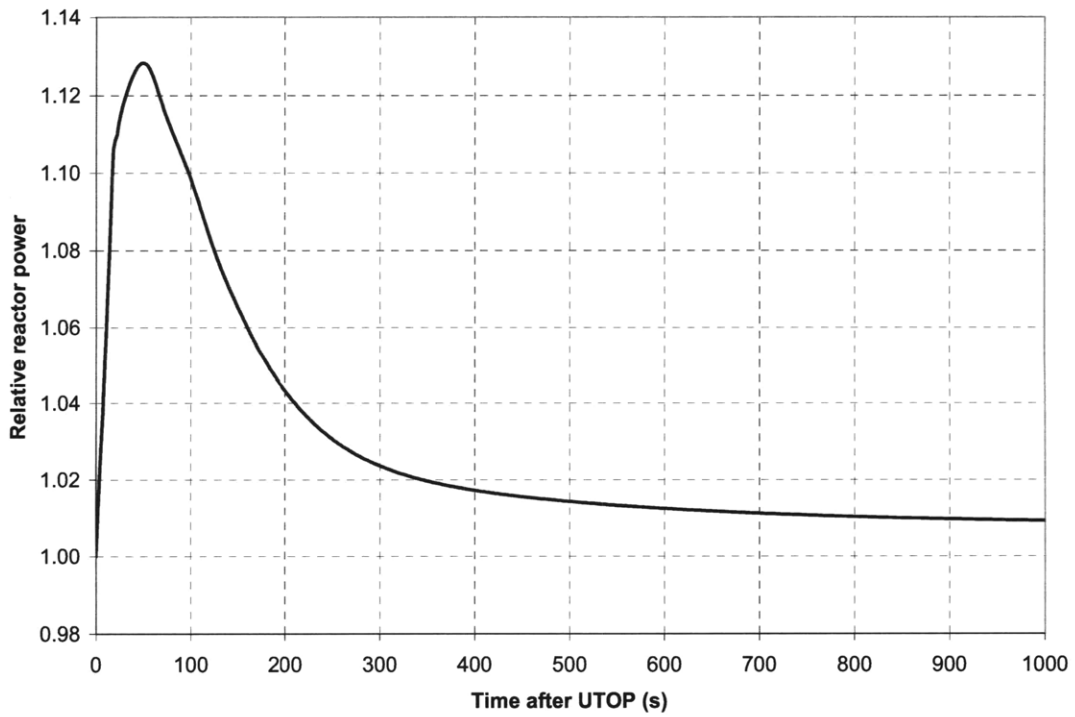


Figure 5.3-3 CR=1 salt reactor power response to a UTOP

The reference salt reactor design displays a very good response to an unprotected overpower transient. This is partly due to small control rod worth of CR=1 design and partly due to the strong reactivity feedback possible through the use of LEMs, which are able to operate rapidly enough to limit positive reactivity and keep reactor power at an acceptable level.

5.4 CR=0 transients

Unprotected station blackout

A detailed description of the unprotected station blackout transient is given in Section 5.1. The CR=0 system was modeled using the same PSACS design as in the CR=1 reference case (the 60% PSACS power, 0.75x tank size case). Short term temperature and reactivity results are given in Figures 5.4-1 and 5.4-2. The reactivity curves are extremely similar, owing to the ability to use LEMs to obtain a desired reactivity response. As a result, the temperature response of the CR=0 core is nearly identical to that of the CR=1 core, with only a slightly higher maximum peak clad temperature (748°C vs. 742°C). Long term peak cladding temperature, reactivity, and power results are shown in Figures 5.4-3 through 5.4-5. Again, results are very similar to the CR=1 case, although there is a brief low-power restart in CR=0 long term response because decay heat from the CR=0 core is significantly less, so temperatures become low enough to cause reactivity to become positive. Overall, the same conclusions can be drawn for the CR=0 core as for the CR=1 core. Following an initial temperature spike the core quickly shuts itself down. Subsequent cooling by the PSACS introduces sufficient reactivity to restart the reactor. A low-power steady state is maintained until the PSACS tanks run out of water, about 36 hours after the SBO begins, after which cooling occurs through only the RVACS.

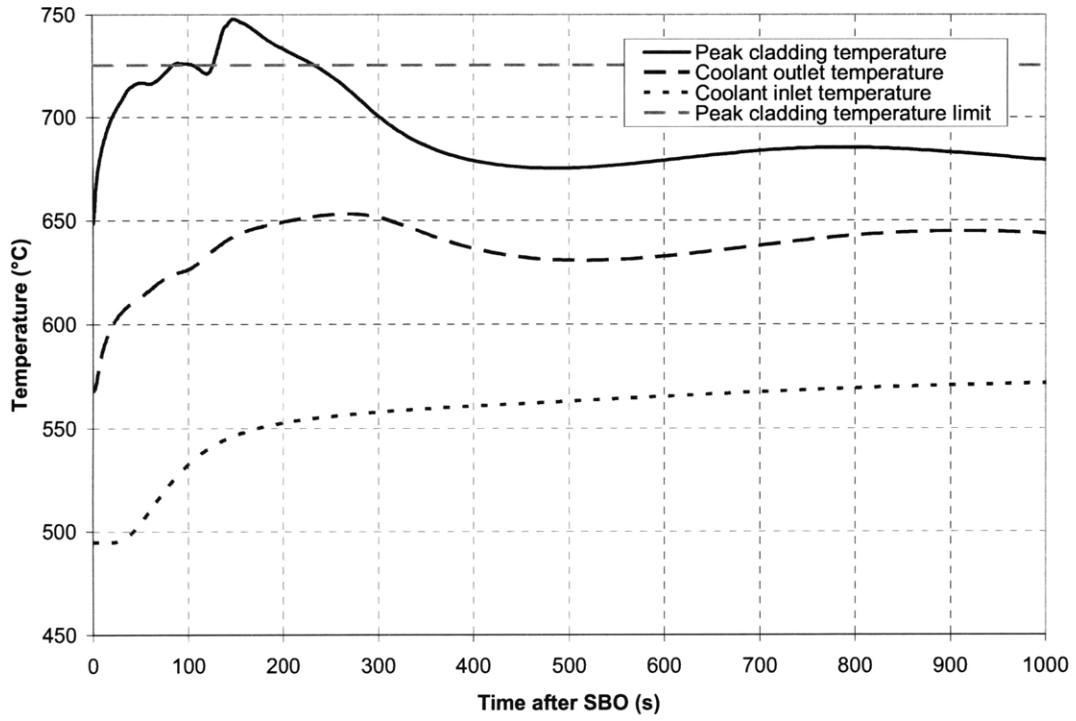


Figure 5.4-1 Short-term CR=0 temperature response to an SBO

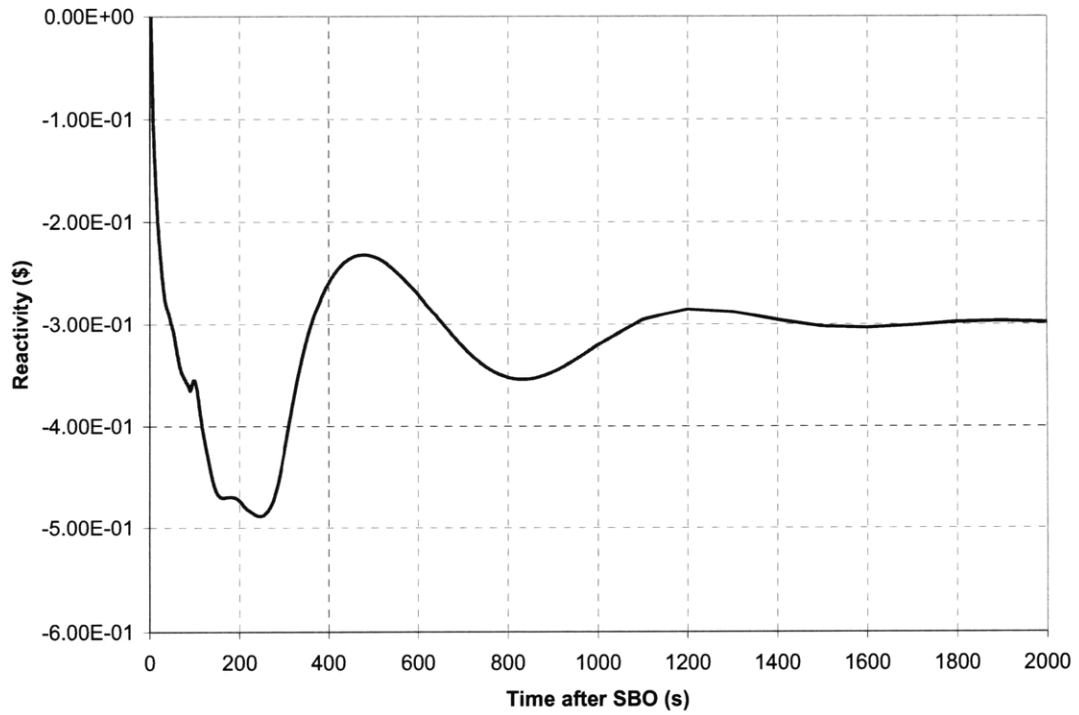


Figure 5.4-2 Short-term CR=0 reactivity response to an SBO

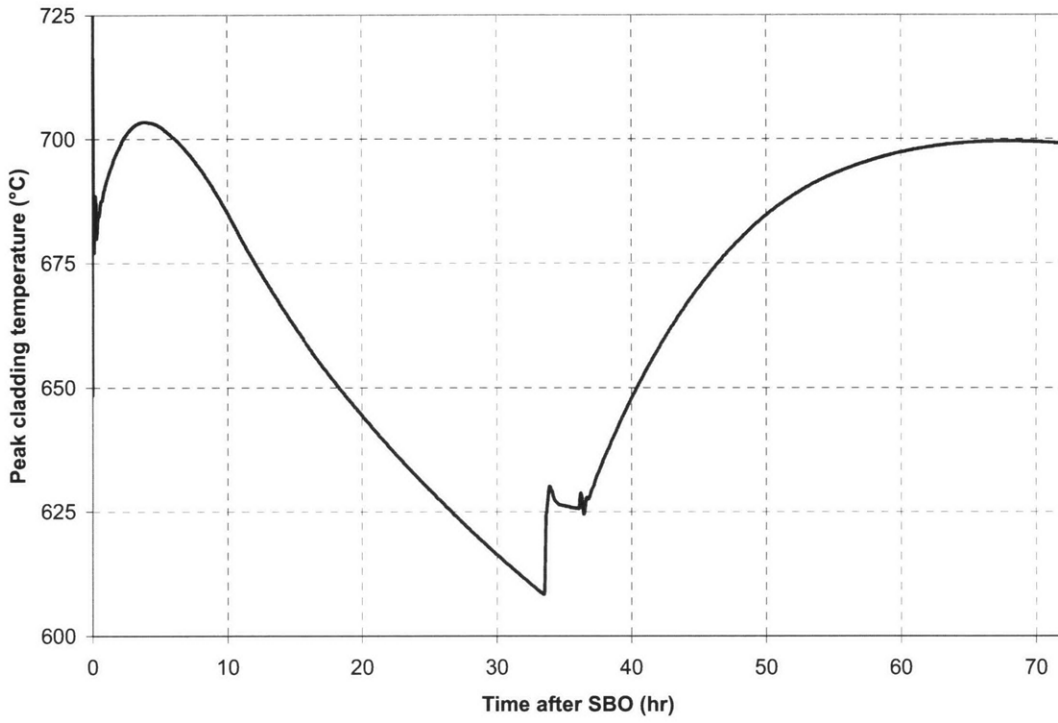


Figure 5.4-3 Long-term CR=0 temperature response to an SBO

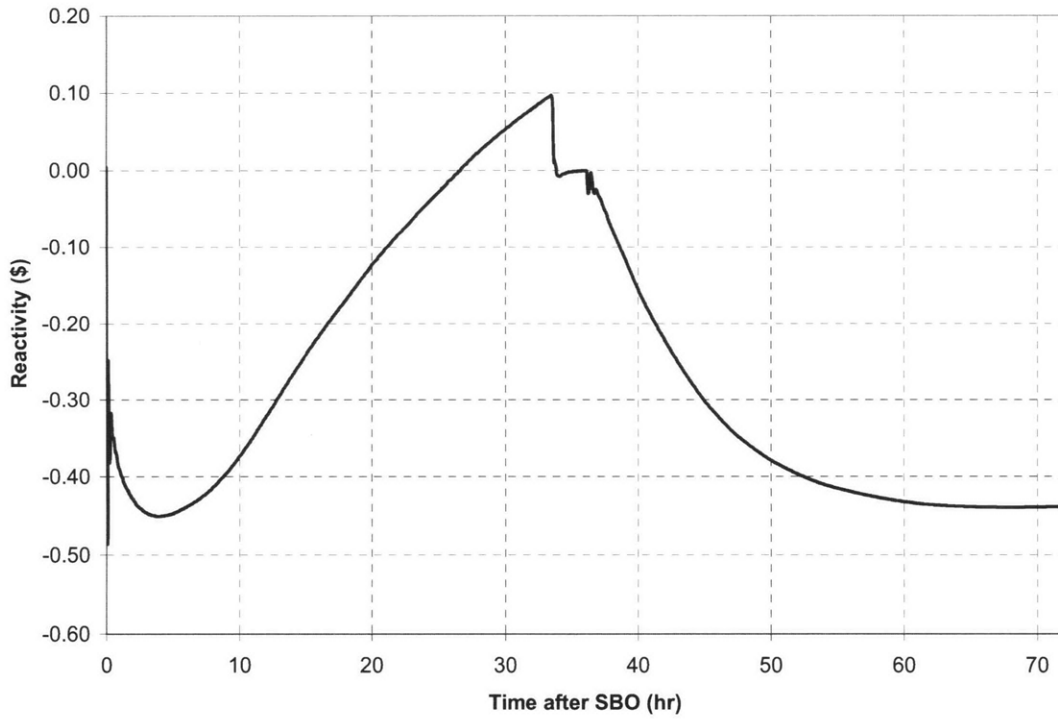


Figure 5.4-4 Long-term CR=0 reactivity response to an SBO

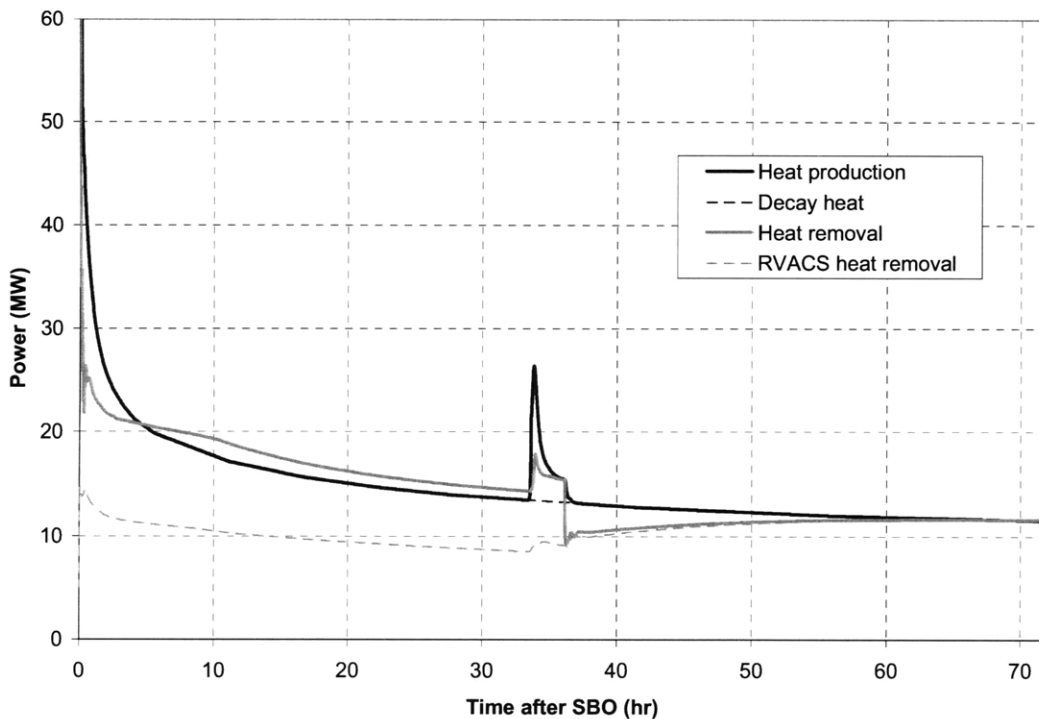


Figure 5.4-5 Long-term CR=0 power response to an SBO

Unprotected loss of flow accident

A description of the loss of flow accident sequence is given in Section 5.2. The same mitigation strategy was tested for the CR=0 system, using a turbine bypass valve governed by a proportional integral controller with a setpoint of 25 rad/s, a proportional weight of 2.9 and an integral weight of 0.02. Results are shown in Figures 5.4-6 through 5.4-8. As with the SBO transient, results are very similar for the CR=0 and CR=1 cores, with the maximum CR=0 temperatures being a few degrees higher. Again the same conclusions can be drawn for the CR=0 core as for the CR=1 core; use of the turbine bypass valve controller allows the heat removed to fairly closely match the heat generated, smoothly bringing the reactor to an 86MW steady state.

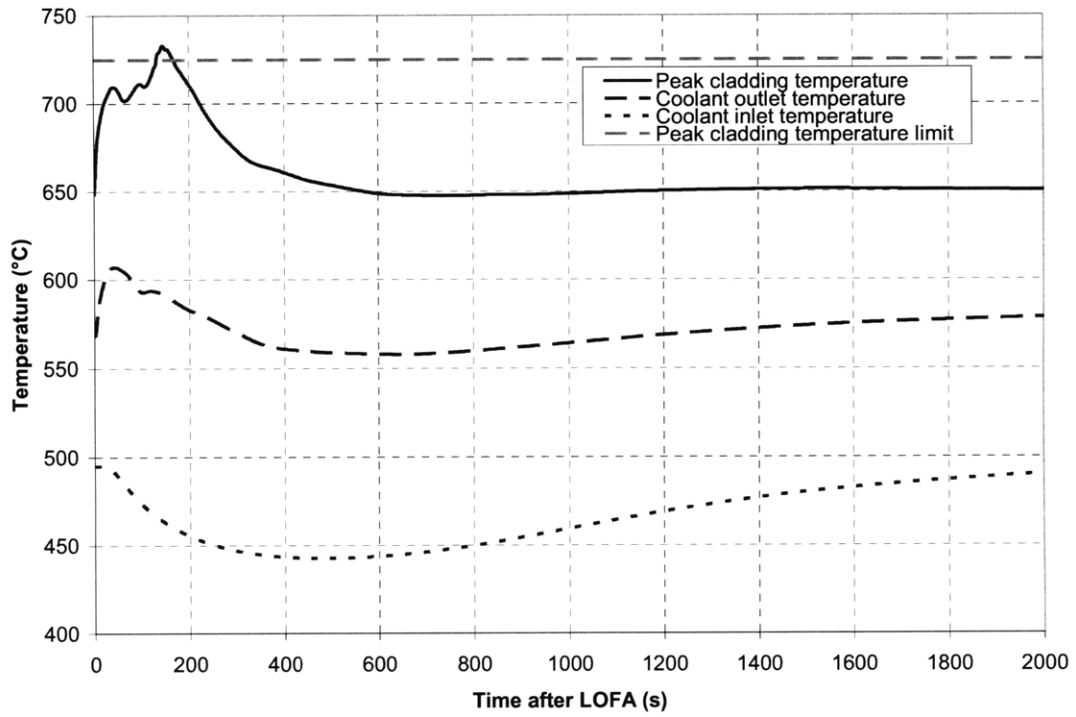


Figure 5.4-6 CR=0 temperature response to a LOFA

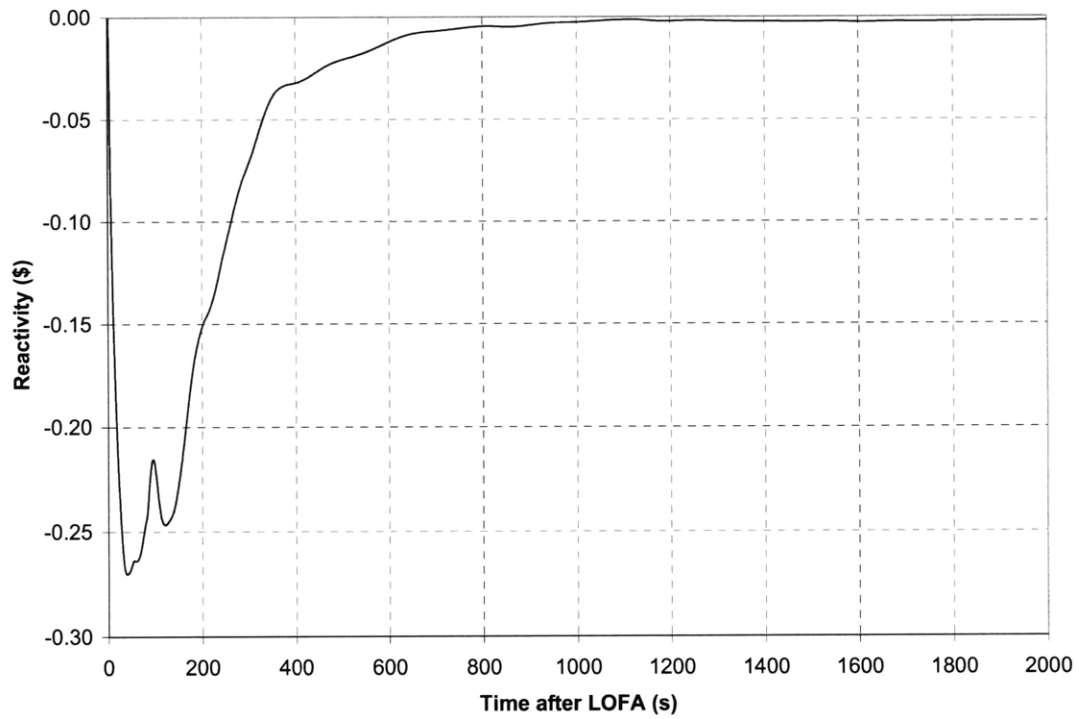


Figure 5.4-7 CR=0 reactivity response to a LOFA

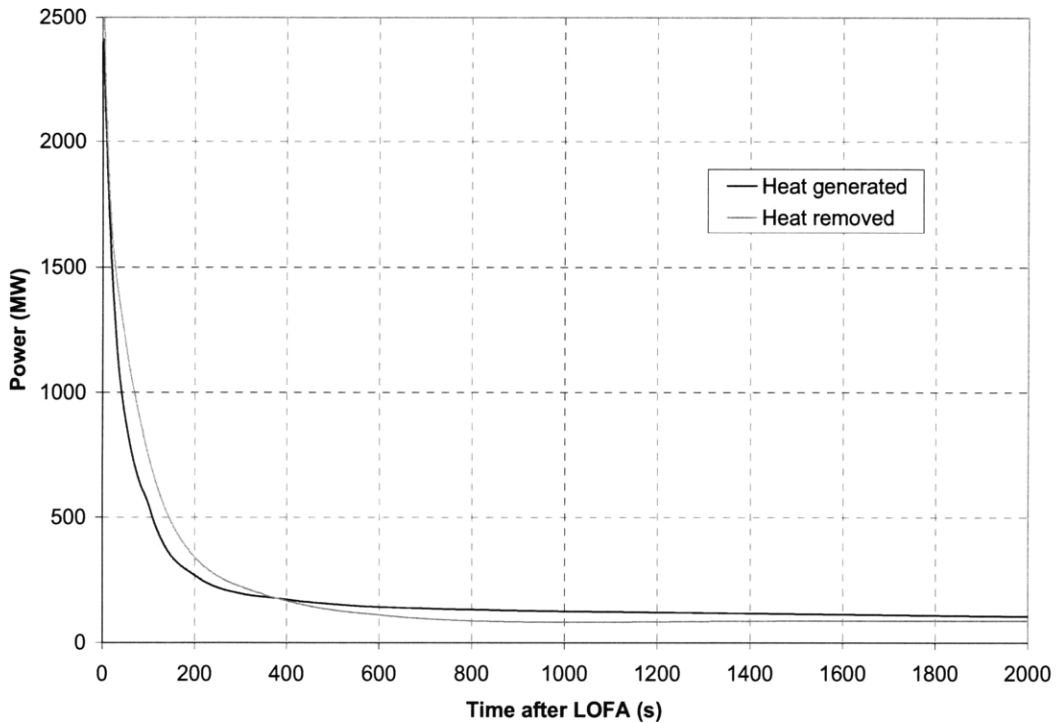


Figure 5.4-8 CR=0 power response to a LOFA

Unprotected transient overpower response

Unlike for the SBO and LOFA transients, the CR=0 reactor UTOP response is different from that for the CR=1 core because the maximum control rod worth is higher for the CR=0 design. Again, maximum rod worth is obtained by dividing the hot zero power excess reactivity by the number of control rod clusters, then multiplying by the assembly peaking factor squared. The specific values used are given in Table 5.4-1. The rate of reactivity withdrawal assumed is twice that of the CR=1 core, corresponding to roughly the same linear speed. Results for the CR=0 UTOP are given in Figures 5.4-9 through 5.4-11.

Table 5.4-1 CR=0 maximum control rod worth

k-effective (max)	1.15
Excess reactivity (\$)	43.770
HFP to HZP (\$)	0.116
Maximum reactivity (\$)	43.886
# of CR clusters	451
\$/cluster (x25 rods)	0.097
Maximum peaking factor	1.35
Maximum rod worth (\$)	0.177
Rate of withdrawal (\$/s)	0.01

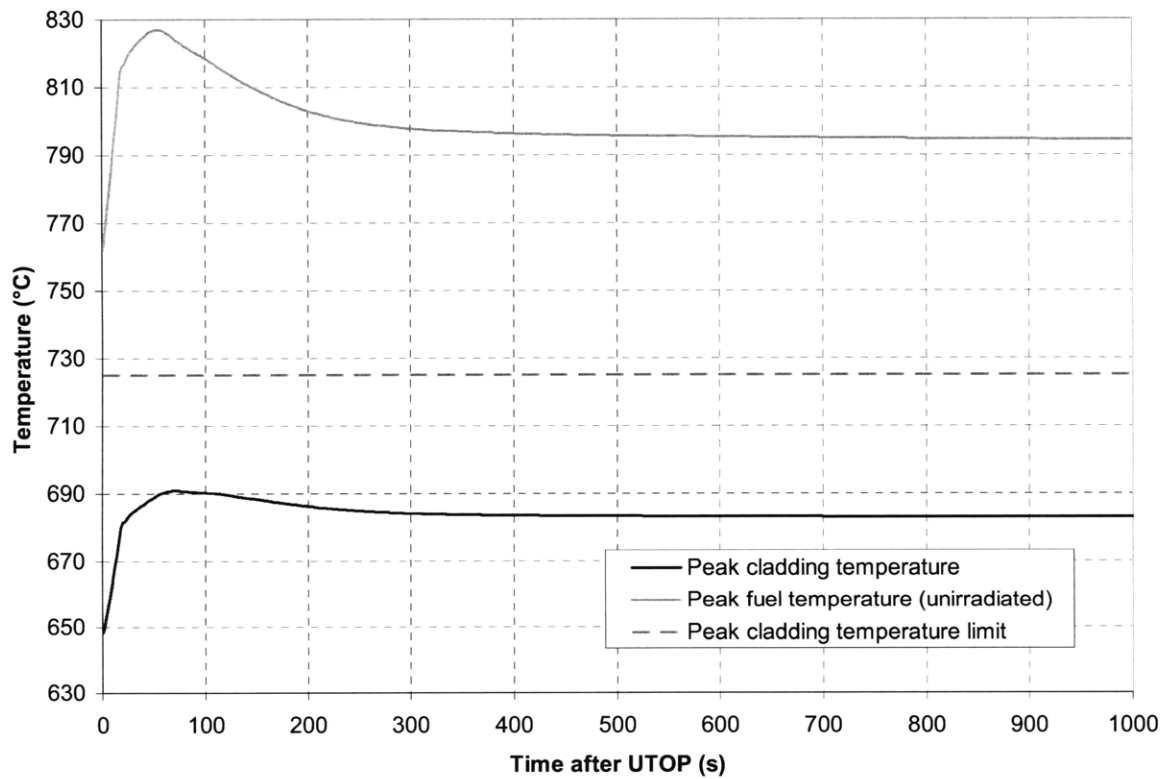


Figure 5.4-9 CR=0 temperature response to a UTOP

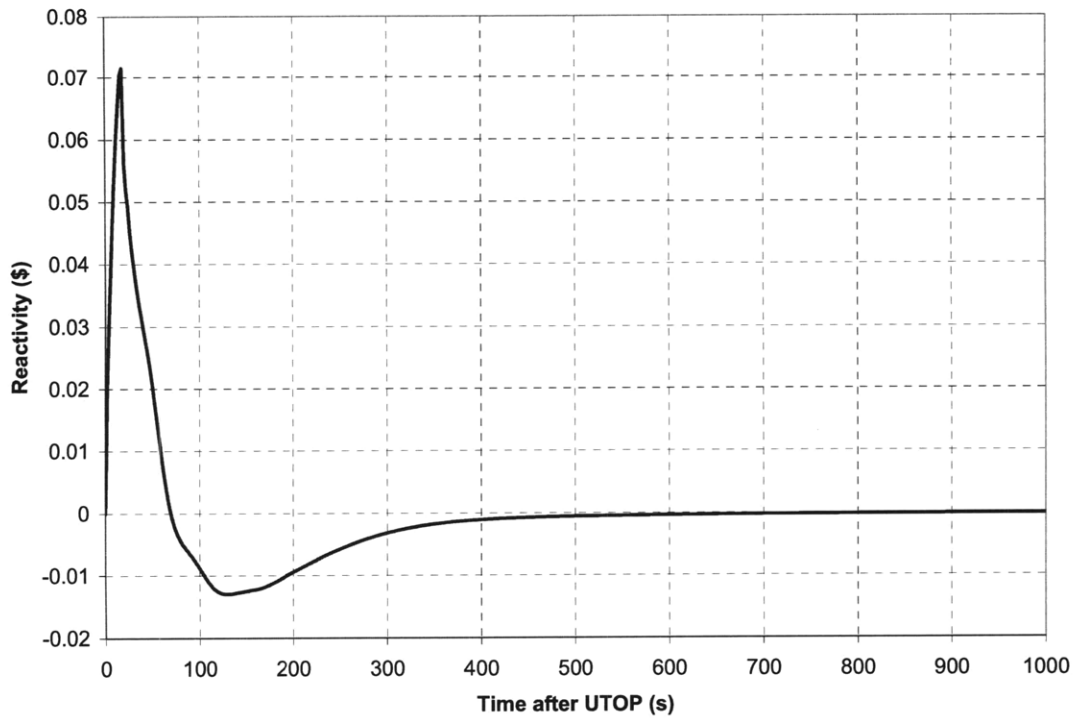


Figure 5.4-10 CR=0 reactivity response to a UTOP

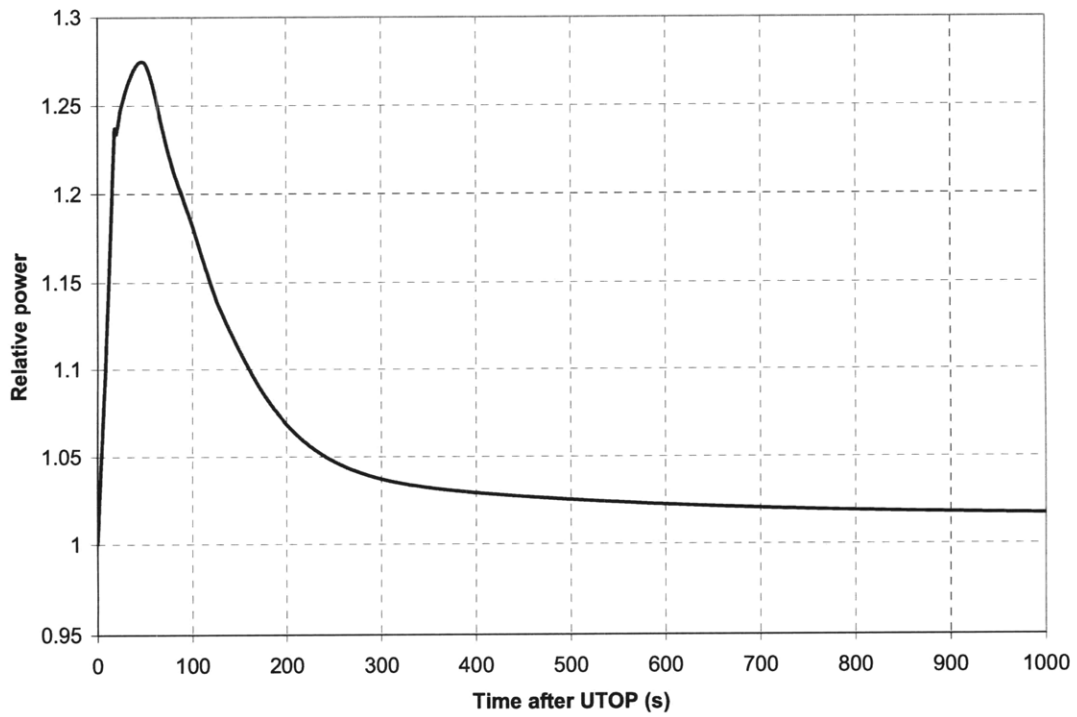


Figure 5.4-11 CR=0 power response to a UTOP

The CR=0 response to a UTOP exhibits higher a maximum reactivity, power, and peak cladding temperature than the CR=1 case. This is a result of the greater reactivity insertion for the CR=0 UTOP. The maximum cladding temperature of 691°C is below the 725°C transient limit, and the peak fuel temperature of 827°C is well below the 1200°C limit. However, this result assumes a thermal conductivity value for unirradiated fuel; the degradation of thermal conductivity with irradiation introduces the possibility of fuel failure. However, repeating the same fuel performance calculation in Section 4.4 following Equation 4.4-1 with a 28% higher linear heat rate (from Figure 5.4-11) shows the maximum temperature rise between the cladding and the fuel is $1.28 \times 320^\circ\text{C} = 410^\circ\text{C}$. Adding this to the maximum cladding temperature of 691°C shows the maximum fuel temperature cannot exceed 1101°C, which is below the 1200°C fuel failure limit. Therefore, there is no risk of cladding or fuel failure during an unprotected overpower.

5.5 Protected Transients

The three transient cases above are all assumed to be unprotected; i.e. the reactor is not scrammed in response to the transient. Furthermore, all three of the reference mitigation strategies employed (with the exception of the two-PSACS-train CR=1 SBO) involve operating the reactor at a safe steady state, i.e. at zero reactivity and some level of fission power.

Therefore, the response to a protected transient in which the reactor is scrammed must be different from but still consistent with the reference mitigation strategies given above. Such a mitigation strategy must be able to remove enough decay heat to prevent fuel element damage (cladding temperature over 725°C) but not so much that the coolant freezes. Due to redundant scram systems, protected transients are much more likely than unprotected ones, so the mitigation of protected transients is an important consideration in reactor design.

Because of the high 2400 MWth power level of the reference reactor, the RVACS by itself is insufficient for removing core decay heat after a shutdown. The power conversion system is better suited for removing large amounts of power (as in the unprotected LOFA) and would be overly expensive to qualify as safety grade equipment. Therefore, the PSACS was developed to provide an additional avenue of heat removal during transients. However, if too much energy is removed through the PSACS during a protected transient, coolant freezing can result. Freezing is very undesirable because it can result in complete flow blockage or damage reactor components. This behavior was observed when simulating a protected transient with four 100% power PSACS trains operating. A protected transient was simulated in RELAP as an SBO (reactor coolant pump trip, isolation of power conversion system), except with a large negative reactivity insertion (the scram) that immediately shuts down the reactor and prevents a restart. For the protected transient simulations, infinitely large PSACS tanks were simulated in the model in order to determine how much energy could be removed through the PSACS before coolant freezing occurred. This information can then be used to determine the maximum tank size that would avoid coolant freezing. For the protected transient, all four PSACS trains were activated (instead of two for the SBO) to create a worst case scenario for coolant freezing. Results of these simulations are shown for the 100% power PSACS and 60% power PSACS for the two conversion ratios in Figures 5.5-1 and 5.5-2.

With all four trains of the 100% power PSACS operating, freezing occurs approximately 19.6 hours into a protected transient for the CR=1 core, and sooner (~13.4 hours) for the lower decay heat CR=0 core. Sizing the PSACS tanks to run out of water before this point would yield

unacceptable behavior during unprotected transients, since the PSACS needs to operate for approximately 36 hours before reactor decay heat is low enough to be removed solely by the RVACS. Therefore, the earlier reference design had to be changed to avoid this behavior; this was done by redesigning the PSACS to remove heat at a lower rate (60% vs. 100% power). With all four 60% power PSACS operating, coolant freezing wouldn't occur during the first 72 hours after a protected transient for the CR=1 reactor, and the first 69 hours for the CR=0 reactor. Since this happens past 72 hours in the CR=1 case, there is no maximum PSACS tank size for the CR=1 reactor since the 72 hour criteria is satisfied even with infinitely large tanks. In the CR=0 case, if the PSACS tanks are too large, then coolant freezing will occur at 69 hours; therefore there is a maximum limit on tank size that needs to be met to avoid coolant freezing. Based on the energy removed by the PSACS during these 69 hours, this maximum tank size was calculated to be 106% the size of the reference PSACS tanks. Since the reference PSACS tanks are below the minimum size that causes coolant freezing, the coolant freezing behavior seen at 69 hours in the CR=0 case would never be encountered. With the actual reference PSACS system in place, it was calculated that the PSACS water tanks would be depleted at 64 hours, about five hours before coolant freezing would occur. This shows that there is some margin for sizing PSACS tanks so they can remove enough energy during an unprotected transient but not too much during a protected transient. The PSACS tanks of the reference design, 6 meters in diameter and 9 meters high (designated as 0.75x tank size in Table 2.3-5), are sufficient to meet both these criteria. Because of the versatility of the 60% power PSACS system to passively mitigate both unprotected transients and protected transients with 2, 3, or 4 trains operating, they were selected for the salt FCR reactor reference design.

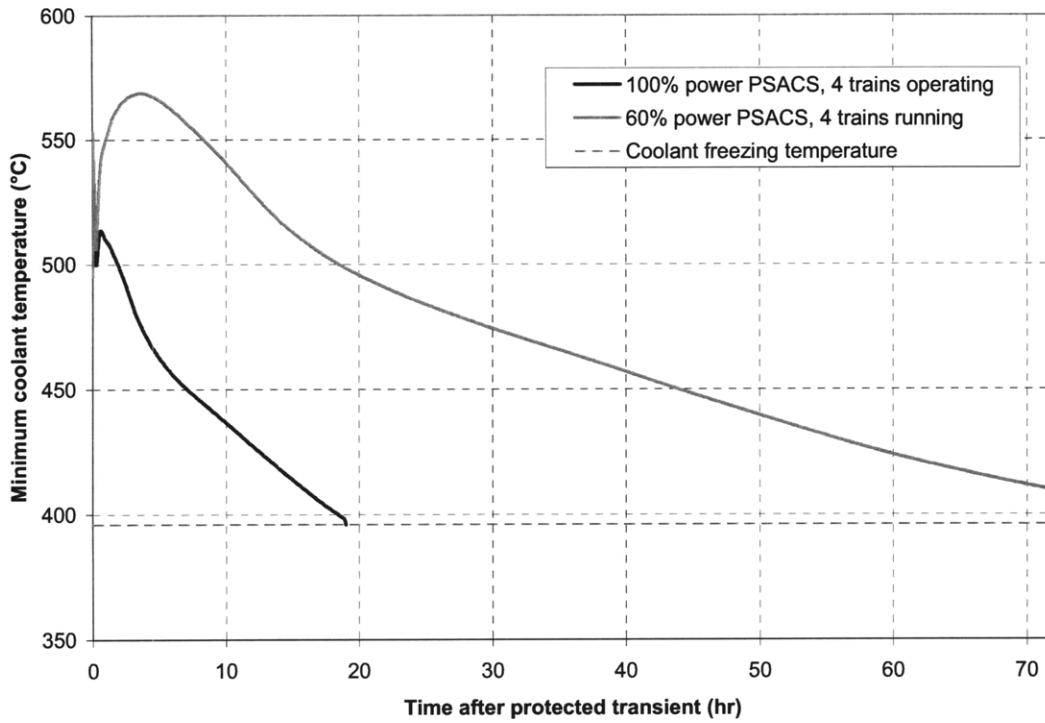


Figure 5.5-1 CR=1 response to a protected transient

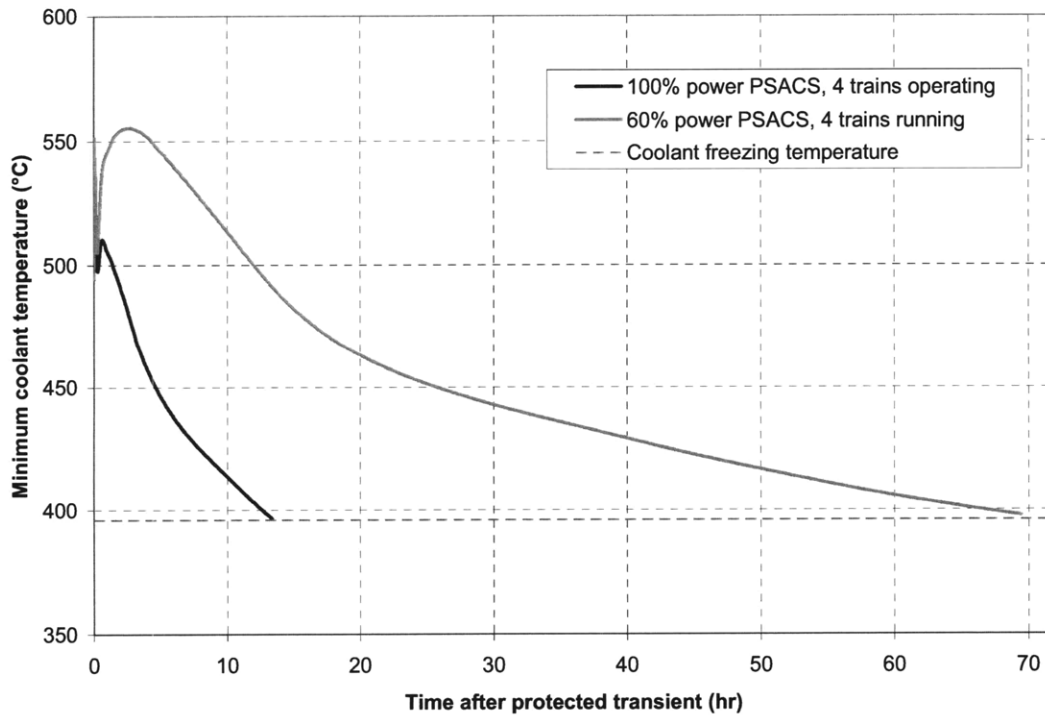


Figure 5.5-2 CR=0 response to a protected transient

6. Conclusions and Future Work

A 2400 MWth liquid-salt cooled flexible conversion ratio reactor can be designed, although doing so is challenging because of the high melting points and poor thermal hydraulics of liquid salts. A system with acceptable power density, temperatures, and overall vessel size was achieved through the use of lithium expansion modules, while operating under reasonable but conservative assumptions on key unknown thermal hydraulic properties of the selected coolant salt. Generally, salt thermal hydraulic properties are inferior to those of liquid metals, owing to a very high viscosity and low thermal conductivities. For thermal hydraulic reasons, a minimum coolant fraction is needed for a core to have a power density over 100 kW/l, however, this coolant fraction was incompatible with achieving acceptable reactivity coefficients. To reconcile this incompatibility, lithium expansion modules were introduced to improve reactivity coefficients and allow a higher coolant fraction. The higher coolant fraction allowed a 130 kW/l power density design to be developed. Although this value is higher than that of the reference lead reactor, it does not translate to a smaller core or vessel because the salt reactor uses peripheral reflector and shield assemblies as well as larger intermediate heat exchangers. A bottlenecked chimney was required to accommodate both these features without increasing the overall vessel size. The non-corrosiveness of liquid salt makes the use of compact printed circuit heat exchangers a possibility for reducing vessel size, but they could be difficult to implement in a pool type design.

The poor heat transfer characteristics of liquid salt mean that for similar coolant temperatures, the cladding temperatures for a liquid salt system would be significantly higher than cladding temperatures for a liquid metal system. As a result, the liquid salt reactor displays a smaller

margin to the cladding temperature limit at steady state as well as higher peak cladding temperatures during transient scenarios. However, due to the use of LEMs, the reactivity response of the salt reactor to transients is very good, and overall transient performance is acceptable. The short term responses to unprotected SBO and LOFA transients briefly exceed the transient cladding temperature limit but are still unlikely to result in fuel failure. Meanwhile, the long term responses to these transients are very good; the reactor is able to safely and passively mitigate them for over 72 hours. Performance following a UTOP is also very good due to the strong reactivity feedbacks.

Continued development of liquid-salt cooled reactor concepts will require addressing some of the uncertainties associated with liquid salt thermal hydraulics. Salt properties for many candidate coolant salts are not well studied. Heat transfer for high Prandtl number fluids in a wire-wrap geometry has also not been studied, which has important implications for a liquid salt reactor because film temperature rises are very significant. Also, heat transfer for transition and laminar flow needs to be better understood to properly characterize salt reactor performance during loss of flow conditions. The ability to use printed circuit heat exchangers represents a potentially significant advantage of liquid salt coolants; designs of these heat exchangers for reactor applications should be developed and compared with PCHEs utilizing other coolants. Liquid salt may be better suited for higher temperature applications due to its lower viscosities at high temperatures and chemical compatibility; higher temperatures would also permit a wider margin to freezing, which is needed because of the high melting points of liquid salts. One remaining challenge for the current liquid salt reactor design is the development of higher temperature vessel materials or the implementation of a means, such as DRACS, to keep vessel temperatures

low. Also, while the PSACS is an effective means of heat removal during transients, it operates in a fairly binary, on/off type manner, so both its power removal capacity and water tank size need to be designed correctly for it to react suitably to both protected and unprotected transients. Even with a proper design, only a small temperature margin to cladding failure is left because of the needed downsizing of the PSACS power removal rate. A passive means of automatically keeping coolant temperatures within an acceptable range independent of design specifics would simplify transient mitigation strategies and could ultimately be easier to license.

References

ASME, "Boiler & Pressure Vessel Code. An International Code. Section III, Division 1, Subsection NH (Class 1 Components in Elevated Temperature Service)." ASME, 2001

Cheng S. K. and Todreas N. E., "Hydrodynamic Models and Correlations for Bare and Wire-wrapped Hexagonal Rod Bundles – Bundle Friction Factors, Subchannel Friction Factors and Mixing Parameters," Nuclear Engineering and Design, v 92, n 2, Apr, 1986, p 227-251

Davis, C., "Implementation of Molten Salt Properties into RELAP5-3D/ATHENA" (INEEL/EXT-05-02658), INL, 2005.

Dostal V., Driscoll M. J. and Hejzlar P., "A Supercritical Carbon Dioxide Cycle for Next Generation Nuclear Reactors", MIT-ANP-TR-100, March 2004.

Duderstadt J., Hamilton L.: Nuclear Reactor Analysis, John Wiley and Sons. Inc. New York, 1976.

EPRI "Advanced Light Water Reactor Utility Requirements Document." EPRI NP-6780-L, 1992

Forsberg C. W., Private communication, April, 2007

Forsberg C.W., "Reactors with Molten Salts: Options and Missions," Proc. of the Frédéric Joliot & Otto Hahn Summer School, August 25 – September 3, 2004, Cadarache, France.

Fridman E., Shwageraus E., Galperin A., "Implementation of multi-group cross-section methodology in BGCore MC-depletion code," Proc. of Physor-2008, Interlaken, Switzerland, September 2008.

Gnielinski, V., "New Equations for Heat and Mass Transfer in Turbulent Pipe and Channel Flow", International Chemical Engineering, v 16, n 2, Apr, 1976, p 359-368.

Haubenreich, P.N., Engel, J.R., "Experience with the Molten-Salt Reactor Experiment," Nuclear Applications and Technology 8: 113-136, 1970

IAEA Fast Reactor Database, 2006

Janz G. J., Molten Salts Handbook, Academic Press, NY, 1967

Kambe, M. and Uotani, M. "Design and development of fast breeder reactor passive reactivity control systems: LEM and LIM," Nucl. Technol., 122, 179, May 1998

Konings R., Private communication February – May 2007

MacDonald P. et. al., "Design of an Actinide Burning, Lead or Lead-Bismuth Cooled Reactor That produces Low Cost Electricity," INEEL/EXT-02-01249, MIT-ANP-PR-092, Idaho National Engineering and Environmental Laboratory, FY-02 Annual Report, (Oct. 2002).

Oda, R. T., Editor, "ALMR Summary Plant Design Description," GE Nuclear Energy, GEFR-00909, March 1993.

Pavel Hejzlar, Jacopo Buongiorno, Phillip MacDonald, and Neil Todreas, „Design Strategy and Constraints for Medium Power Lead-alloy Cooled Actinide Burners“, Nuclear Technology, Vol. 147, pp. 321-343, September 2004.

Polyakov P. V. and Gildebrandt E. M., "Investigation of Thermal-Conductivity of Melts of System KCl-MgCl₂," High Temperature 12(4), 780–781 (1974)

Raseman C. J., Susskind H., Farber G., McNulty W. E., and Salzano F. J., "Engineering Experience at Brookhaven National Laboratory in Handling Fused Chloride Salts," BNL-627, T-192, Brookhaven National Laboratory, Brookhaven, NY, 1960

Robertson, R.C., "MSRE Design and Operations Report, Part I, Description of Reactor Design" ORNL-TM-0728, 1965

Shwageraus, E., Hejzlar, P., Driscoll, M.J., "Nuclear Design Feasibility of a Lead-cooled Fast Reactor with Flexible Conversion Ratio," ANS/ENS international Meeting, Washington D.C., 2007.

Susskind et al., "Corrosion Studies for a Fused Salt-Liquid Metal Extraction Process for the Liquid Metal Fuel Reactor", BNL-585, 1960.

Todreas N.E, and Kazimi M.S, Nuclear Systems I: Thermal Hydraulic Fundamentals, Hemisphere Publishing Corp. 1993.

Todreas N.E., Hejzlar P., Shwageraus E., and Whitman J., "Flexible Conversion Ratio Fast Reactor Systems Evaluations", 1st Quarterly report, Center for Advanced Nuclear Energy Systems, MIT, MIT-NFC-PR-087, July 2006a.

Todreas N.E., Hejzlar P., Shwageraus E., Petroski R., Nikiforova A., and Whitman J., "Flexible Conversion Ratio Fast Reactor Systems Evaluations", 2nd Quarterly report, Center for Advanced Nuclear Energy Systems, MIT, MIT-NFC-PR-087, October 2006b.

Todreas N.E., Hejzlar P., Shwageraus E., Petroski R., Nikiforova A., and Whitman J., "Flexible Conversion Ratio Fast Reactor Systems Evaluations", 3rd Quarterly report, Center for Advanced Nuclear Energy Systems, MIT, MIT-NFC-PR-090, January 2007a.

Todreas N.E., Hejzlar P., Shwageraus E., Petroski R., Nikiforova A., and Whitman J., "Flexible Conversion Ratio Fast Reactor Systems Evaluations", 1st Yearly report, Center for Advanced Nuclear Energy Systems, MIT, MIT-NFC-PR-092, June 2007b.

Todreas N.E., Hejzlar P., Shwageraus E., Petroski R., Nikiforova A., and Whitman J., A. Boogaerts, J.I. Lee, and C.J. Fong “Flexible Conversion Ratio Fast Reactor Systems Evaluations”, 5th Quarterly report, Center for Advanced Nuclear Energy Systems, MIT, MIT-NFC-PR-093, July 2007c.

Todreas N.E., Hejzlar P., Shwageraus E., Petroski R., Nikiforova A., and Whitman J., A. Boogaerts, J.I. Lee, and C.J. Fong “Flexible Conversion Ratio Fast Reactor Systems Evaluations”, 6th Quarterly report, Center for Advanced Nuclear Energy Systems, MIT, MIT-NFC-PR-097, October 2007d.

Todreas N.E., Hejzlar P., Shwageraus E., Petroski R., Nikiforova A., and Whitman J., A. Boogaerts, J.I. Lee, and C.J. Fong “Flexible Conversion Ratio Fast Reactor Systems Evaluations”, 7th Quarterly report, Center for Advanced Nuclear Energy Systems, MIT, MIT-NFC-PR-097, January 2008a.

Todreas, N., Hejzlar, P., Shwageraus, E., Petroski, R., Nikiforova, A., Whitman, J., Fong, C., “Flexible Conversion Ratio Fast Reactor Systems Evaluations,” Final report, Center for Advanced Nuclear Energy Systems, MIT-NFC-PR-101, MIT, Cambridge, Massachusetts, July 2008b.

Wade, D.C., Chang, Y.I., “The Integral Fast Reactor Concept: Physics of Operation and Safety”, Nuclear Science and Engineering, 100, 507-524, 1988.

Williams D.F. and Toth L.M., “Assessment of Candidate Molten Salt Coolants for the NGNP/NHI Heat Transfer Loop,” ORNL/TM-2006/69, June 2006b.

Williams D.F., Toth L.M. and Clarno K.T., “Assessment of Candidate Molten Salt Coolants for the Advanced High-Temperature Reactor (AHTR),” ORNL/TM-2006/12, March 2006a.